Deployment of Pulsed Eddy Current Technology for Non-Destructive Testing Using Unmanned Aerial Vehicles

Taiyi Zhao

Centre for Ultrasonic Engineering

Department of Electronic and Electrical Engineering

University of Strathclyde, Glasgow

A thesis submitted for the degree of

Doctor of Philosophy

2024

Copyright

This thesis is the result of the author’s original research. It has been composed by the author and has not been previously submitted for examination which has led to the award of a degree.

Signed:

Date: *1st August 2024*

Acknowledgement

Time flies, and now I find myself at the end of my PhD academic journey, filled with mixed emotions.

I would like to express my gratitude to my supervisor, Prof. Charles MacLeod. He welcomed an undergraduate student with no academic achievements into his lab for the internship during my third year. Whenever I faced academic challenges, he provided just the right amount of guidance, often illuminating my understanding and inspiring my thoughts. Even during times of personal crisis, he helped me maintain a proper perspective on life. It has been a great honour to work with him.

I also want to extend my deepest thanks to Dr. Dayi Zhang for the meticulous help and support throughout my PhD academic career.

I would also like to thank Dr. Robert Watson for his selfless academic guidance and Dr. William Jackson for his lab assistance - the drone team shall never be forgotten. I am grateful to Prof. Gordon Dobie for providing me with an internship and an electronic engineer opportunity at PPS UK. I appreciate Dr. Ehsan Mohseni for his help with my knowledge of eddy currents, Walter Galbraith for his assistance in building electronic circuit systems, and Ross McMillan and Adam Gilmour for their companionship in the lab. I am also appreciative of the support and resources provided by Cailean Forrester from Inspectahire Ltd (UK) and Dr. Paul Crouzen from Maxwell NDT Ltd (The Netherlands).

Thank you to Kanye West's "DONDA" listening parties for keeping me company during the lonely nights in the lab over the last six months of 2023.

Finally, I am immensely grateful to my parents for their upbringing and support, ensuring that I have never had to worry about my basic needs.

The PhD journey has been a time of acquiring knowledge and exploring UAV NDT and PEC field boundaries. While the completion of this journey brings me joy, some of the time has also been a period of profound sorrow. In 2022, I received the heartbreaking news that my grandfather had passed away, but I could not attend the funeral due to COVID restrictions. The man with immense responsibility raised me from a young age. Although he did not teach me any academic knowledge, he taught me how to conduct myself and how to navigate life. Everything I have achieved today is inseparable from his painstaking care.

I am deeply grateful to my grandfather and hope that he can see my accomplishments from heaven.

Taiyi Zhao

June 2024

Abstract

The necessity to inspect essential infrastructure such as oil and gas pipelines for wear, and deterioration highlights the critical role of enhancing Non-Destructive Testing (NDT) methods. Routine inspections, including assessments of wall thinning, are essential for ensuring the structural integrity of these assets and preventing serious accidents. Although Unmanned Aerial Vehicles (UAVs) equipped with high-resolution cameras offer a safer and more efficient alternative for remote visual inspections, they are limited to surface-level assessments and cannot detect subsurface defects or measure wall thickness beneath coatings. This limitation reduces their effectiveness for industrial pipe inspections. Pulsed Eddy Current (PEC) technology, on the other hand, provides a promising solution, capable of assessing the thickness beneath coatings and addressing the shortcomings of camera-based inspections. However, traditional PEC systems are effective but bulky and difficult to incorporate within mobile platforms, limiting their versatility and ease of deplorability.

This thesis describes the challenges facing the energy and petrochemical sectors when considering remote asset inspection and proposes new innovations and techniques to improve such inspections. The thesis presents on the benefits related to remotely deployable inspections, particular those from UAVs and investigates quantifiable PEC inspection from such platforms. Firstly, the performance of a conventional commercial PEC sensor is evaluated for its suitability in autonomous airborne inspections. The PEC sensor is affixed to a robot manipulator and precisely controlled to simulate airborne inspections across various alignment angles. Through systematic analysis, the

impact of sensor alignment on inspection accuracy is comprehensively assessed, demonstrating critical factors influencing the reliability of UAV-based PEC NDT.

Building on these findings, the thesis introduces a novel, compact PEC sensor system to address the global challenges, enhancing PEC inspections for mobile platforms. The system can be effectively mounted on a crawler-hybrid UAV, facilitating detailed 360-degree inspections of pipe surfaces. Findings detail the autonomous deployment of this PEC system via an UAV for the non-intrusive assessment of wall thickness. Finite element analysis was used for the design and performance evaluation of the PEC system. When finally, integrated with a multirotor-crawler UAV engineered for navigating through complex and dangerous pipeline environments, this mobile PEC system can conduct thorough evaluations of steel pipeline wall thinning. The system delivers a sensing method that achieves accurate thickness measurements, with errors under 4.8%, facilitating reliable and comprehensive asset inspections.

Table of Contents

List of Figures

List of Tables

List of Acronyms

2D	Two Dimensional
3D	Three Dimensional
ADC	Analog-to-Digital Converter
ALSFL	Adaptive Least Square Fitting Line
ASME	American Society of Mechanical Engineers
CAD	Computer-Aided Design
CUE	Centre for Ultrasonic Engineering
CoM	Centre of Mass
CUI	Corrosion Under Insulation
DAQ	Data Acquisition
DTM	Digital Terrain Model
DFT	Discrete Fourier Transform
DOFPOS	Degrees of Freedom Positioning System
EC	Eddy Current
ECT	Eddy Current Testing
EMI	Electromagnetic Interference
ESC	Electronic Speed Controller

FEA	Finite Element Analysis
FFT	Fast Fourier Transform
FPSO	Floating Production Storage and Offloading
FT	Fourier Transform
ILI	Inline Inspection
INCOTEST	INsulated COmponent TESTing
ITRA	Interfacing Toolbox for Robotic Arms
MDT	Multidirectional Thrust
MFL	Magnetic Flux Leakage
MOSFET	Metal-Oxide-Semiconductor Field-Effect Transistor
NDE	Non-Destructive Evaluation
NDT	Non-Destructive Testing
PAUT	Phased Array Ultrasonic Testing
PEC	Pulsed Eddy Current
PPMS	Physical Property Measurement System
PV	Photovoltaic
RFT	Remote Field Testing
RTD	Röntgen Technische Dienst
RMSE	Root Mean Square Error

SNR	Signal to Noise Ratio
SLAM	Simultaneous Localisation and Mapping
SLA	Stereolithography
SQUID	Superconducting Quantum Interference Devices
UAV	Unmanned Aerial Vehicles
UT	Ultrasonic Testing

Chapter 1 Introduction

1.1 Context of Research

1.1.1 Oil & Gas Sector

While the UK is transitioning to a renewable low-carbon energy model, the oil and gas sector remains a significant contributor to the national economy and energy supply. In 2021, this sector provided approximately 26,900 jobs and contributed £31.1 billion in gross value added [1]. The oil and gas industry remains essential for meeting current energy demands and supporting economic stability. However, the sector faces substantial challenges related to the maintenance and inspection of aging infrastructure, which is prone to corrosion and other forms of degradation. These issues necessitate regular and thorough inspections to ensure structural integrity and safe operation, with failure to do so potentially resulting in costly unplanned outages [2].

For instance, an unplanned shutdown of a refinery or an offshore platform can lead to lost production valued at hundreds of thousands to millions of dollars per day [2]. Moreover, the costs associated with the extensive preparation required for traditional inspection methods, including scaffolding, crane lifts, and insulation removal, further add to the financial burden. Investing in more efficient and effective inspection technologies can therefore yield substantial economic benefits [1]. By reducing the frequency and duration of shutdowns, minimizing the need for extensive preparatory work, and enhancing the accuracy and reliability of inspections, the industry can achieve significant cost savings and improve overall operational efficiency [2].

The oil and gas industry is particularly vulnerable to various forms of corrosion and degradation due to the harsh environments in which it operates. Pipelines, pressure vessels, and storage tanks are critical components that require constant monitoring to prevent failures [3-10]. These structures frequently experience both interior and exterior corrosion, including specific issues like stress corrosion cracking, high-temperature hydrogen attack, and Corrosion Under Insulation (CUI), where moisture trapped at the pipe wall-insulation boundary causes accelerated corrosion [3-10], shown in Figure 1-1. This degradation can lead to significant safety hazards and economic losses if not properly managed [5-10].

Figure 1-1: Examples of degraded pipework within the oil and gas sector (a) Insulated pipe with cladding removed to show corrosion under insulation (b) Leaked pipework due to corrosion [11].

Non-Destructive Testing (NDT) is an inspection method used to quantify structural health ultimately before failure occurs. It examines structures and components in a safe manner without causing damage. The process of such evaluations does not permanently destroy the serviceability of the target object; thus, components are still usable after inspection. The advantages are both operational and financial. Such evaluations provide an indication of the structural health to experienced inspectors, which then leads to a decision on repairing or retiring the corresponding component. Such inspections can be undertaken in-situ, while the system is operating. Numerous

NDT approaches have been developed, researched, and observed in many industrial applications over the last few decades. Examples of NDT techniques include liquid penetrant, magnetic particle, eddy current, and radiographic testing, as well as visual and ultrasonic methods used by many commercial and industrial inspection services [12].

Among these, Pulsed Eddy Current (PEC) technology, as one electromagnetic technique, has seen a surge in interest due to its ability to inspect through coatings and its non-contact nature, making it ideal for assessing the integrity of structures where direct access is a challenge [13]. The technique is particularly relevant for ferromagnetic pipe materials, aligning with recent studies focused on PEC sensing of ferromagnetic material thicknesses [14-17]. Ulapane et al [14] show the advantages of PEC for critical pipe inspection, especially for measuring the remaining thickness of existing pipes.

However, elevated pipework presents additional challenges for manual inspections. The inspection process in the oil and gas industry is complex and resource-intensive. Traditional inspection methods often involve manual inspections, which can be hazardous, time-consuming, and expensive. For example, inspecting elevated pipelines or storage tanks typically requires extensive scaffolding, crane lifts, or rope access techniques, as shown in Figure 1-2, all of which pose significant safety risks to personnel. Additionally, the need to inspect confined spaces, such as the interiors of storage tanks or pressure vessels, presents further challenges. These environments are not only difficult to access but also pose significant health and safety risks due to the presence of hazardous materials and confined space entry requirements.

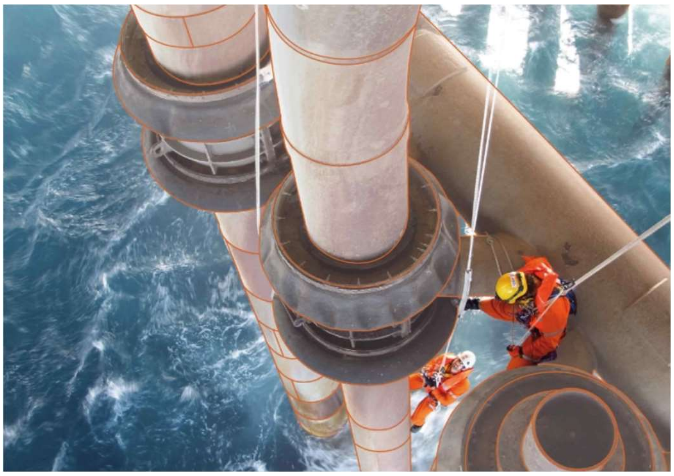

Figure 1-2: Example of work at height conducted from an offshore platform [18].

1.1.2 Aerial Remote Inspection

In light of the hazards associated with manual inspections and the subjective nature of human assessment, automated NDT procedures are becoming increasingly valuable. The advent of Industry 4.0 has catalysed the integration of mobile robotics and automation into inspection processes, offering significant advantages in speed, accuracy, and safety [19], [20]. UAVs, in particular, have proven to be practical tools for non-contact visual screening across various energy generation applications, including wind turbines, nuclear sites, and oil and gas facilities [21-26].

The deployment of UAVs for comprehensive visual inspections offers numerous advantages over traditional methods. UAVs can access difficult-to-reach areas without the need for scaffolding or crane lifts, significantly reducing the safety risks associated with manual inspections [21], [22]. Additionally, UAVs can conduct inspections more quickly and efficiently, minimizing downtime and disruption to operations [25]. UAVs provide more consistent and objective data, reducing the subjectivity inherent in human assessments and leading to more accurate and reliable inspection results [22].

For example, UAVs can inspect elevated pipework, storage tanks, and pressure vessels without the need for scaffolding or cranes [25]. This approach allows for rapid, comprehensive assessments of large and complex structures, identifying areas of concern and enabling targeted follow-up inspections. Additionally, UAVs can quickly detect issues such as coating or insulation flaws, leaks, and structural distortions, which are critical for maintaining the integrity of these assets [23].

Several case studies highlight the practical advantages and applications of UAV technology in the oil and gas sector. For instance, UAVs have been used to inspect the underdeck of jack-up platforms, a task traditionally requiring a six-person team of rope access technicians working at height above the splash zone for almost 100 days. UAV inspection can deliver a full visual screening in just three days, significantly reducing hazard exposure and inspection costs [27].

In another instance, UAVs were deployed to inspect the primary tank within a Floating Production Storage and Offloading (FPSO) vessel. A conventional inspection would involve a four-person team spending 14 days within a confined space. By contrast, UAV operations allowed two inspectors to complete the process in under four days without entering the tank, enhancing safety and efficiency [27]. These case studies demonstrate the potential of UAVs to revolutionize inspection processes in the oil and gas industry.

The integration of advanced NDT technologies with UAV platforms, particularly focusing on PEC technology, is a focal point of this research. Including photogrammetry testing, techniques such as ultrasonic testing (UT) [28], [29] and thermographic testing [30] can be adapted for deployment via UAVs, providing a comprehensive assessment of structural integrity. These methods allow for the detection of subsurface defects, material thickness measurements, and other critical parameters that visual inspections alone cannot reveal. Ultrasonic testing, for example, involves sending high-frequency sound waves into materials to detect internal flaws [29]. When integrated with UAVs, this technology can be used to inspect areas that are difficult to access manually, such as high-rise structures or submerged components. Similarly, thermographic testing uses infrared imaging to detect temperature variations on the surface of materials, which can indicate subsurface defects and areas of structural weakness [30]. By combining these advanced NDT techniques with UAV technology, the research aims to provide a more thorough and accurate assessment of infrastructure health, ultimately enhancing safety and reliability.

1.2 Problem Statement

The inspection and maintenance of critical infrastructure, such as oil and gas pipelines, pressure vessels, above-ground storage tanks, and offshore platforms, are essential to ensuring their structural integrity and safe operation. However, these inspections are often challenged by several factors:

- **Corrosion Threats**: In the oil & gas sector, stringent inspections are required to manage aging infrastructure and ensure safety. Corrosion, particularly flow accelerated corrosion, poses a severe threat to the integrity of these structures, leading to significant economic impacts. In 2016, the global cost of managing corrosion was estimated at USD $1.4 trillion [31].

- **Limitations of Traditional Inspection Methods**: Traditional inspection methods are labour-intensive, time-consuming, and often involve hazardous environments. They require extensive manual intervention, including scaffolding, crane lifts, or rope access, leading to high costs, significant downtime, and potential safety risks.
- **Inadequacy of UAV-Based Inspections**: While UAVs equipped with high-resolution cameras provide a safer and more efficient alternative for remote visual inspections, they are limited by their inability to detect subsurface defects or assess thickness under coatings. This limitation restricts their effectiveness in industrial pipe inspection. Sensors such as UT and Eddy Current (EC), which are typically used for these purposes, face significant challenges when deployed with UAVs. UT is a contact-only method that requires a coupling medium to transmit sound waves, making it impractical for airborne use. Additionally, EC instruments tend to be bulky and are highly susceptible to electromagnetic noise, which is difficult to eliminate in UAV environments. These limitations make it challenging to integrate UT and EC into UAV platforms, restricting their effectiveness for thorough industrial pipe inspections where subsurface analysis is critical.

- **Bulkiness of Traditional PEC Systems**: PEC technology offers a potential solution due to its non-contact nature and ability to inspect through coatings. However, traditional PEC systems are typically bulky, requiring substantial power supplies and large-scale signal generators, which restricts their deployment in agile and mobile inspection scenarios.

These challenges highlight the need for innovative inspection solutions that can provide comprehensive, efficient, and safe assessments of critical infrastructure, such as oil and gas industry pipelines, particularly in complex and hazardous environments.

1.3 Research Aims and Objectives

This section outlines the primary research goals of this thesis, which focus on enhancing the PEC NDT method for inspecting critical infrastructure, such as oil and gas pipelines, using innovative UAV technologies.

1. Evaluate the Performance of Conventional PEC Sensors for UAV Inspections: Assessing the suitability of conventional commercial PEC sensors for autonomous airborne inspections and identify critical factors that influence the reliability of UAV-based PEC NDT.

2. Design and Development of a Compact PEC Sensor System for Mobile Platforms: Design of a novel, compact PEC sensor system that addresses the challenges of traditional PEC systems, such as bulkiness and difficulty in deployment and integration on mobile platforms crawler-hybrid UAVs.

3. Enhanced UAV deployed PEC Inspections for 360-Degree Pipe Surface Coverage: Integration of the PEC sensor system with a multirotor-crawler UAV designed to navigate complex and hazardous pipeline environments, to facilitate autonomous UAV Deployed 360-degree inspections of pipe surfaces for accurate thickness measurements.

1.4 Contributions to Knowledge

This thesis makes three distinct contributions to the field of NDT, particularly in the application of PEC technology and its integration with robotic systems and UAVs.

1.4.1 Performance and System Characterization of the MAXWELL PEC P1 Probe

To addressing challenges in sensor sensitivity, accuracy, and enhancing PEC applications in UAV-based NDT, the MAXWELL PEC P1 probe's performance was studied. In particular, this work presents the following contributions:

- Provides a comprehensive study on the performance of the MAXWELL PEC P1 probe in measuring the thickness of carbon steels.
- Highlights the probe’s sensitivity to orientation angles and thickness variations.
- Offers valuable insights for optimizing PEC probe deployment in various industrial contexts.

1.4.2 Characterisation of Pulsed Eddy Current Sensor for Thickness Measurement

In response to the research aims and goals posed above, a novel dual-coil customised PEC sensor system was proposed. This system presents the following contributions:

- Advances the design of a dual-coil PEC sensor system for mobile NDT of ferromagnetic materials.
- Utilises finite element analysis (FEA) simulations to demonstrate improvements in detecting material thickness variations.
- Study probe parameter effect on the PEC sensor thickness measurement performance.
- Provides insights on the effects of lift-off distances and coil configurations, enhancing PEC system sensitivity and accuracy.
- Minimises the weight of the entire PEC system, making it adaptable to UAV integration.

1.4.3 Integration of PEC Technology with UAV Systems:

To meet the research aims and goals stated above, the customised PEC sensor system was integrated with the hybrid UAV-crawler. The novel aerial robotic approach presents the following contributions:

- Modifies and improve the design of a hybrid UAV-crawler to integrate the PEC system.
- Demonstrates the stability, disturbance rejection, and comprehensive inspection capabilities of the hybrid UAV-crawler with PEC system.

- Enhances the whole system's reliability and accuracy of thickness measurements through signal processing techniques such as Butterworth low-pass filtering, Fourier Transform, and Savitzky-Golay smoothing.

1.5 Thesis Structure

This thesis is structured into six chapters, each dedicated to exploring different aspects of NDT technologies, their advancements, and their applications in industrial settings, particularly focusing on PEC methods and their integration with UAVs.

Chapter 2 presents a detailed review of related work in the field of NDT. It begins with an introduction to PEC inspection techniques, covering their principles and system configurations. The chapter explores PEC-based ferromagnetic material thickness quantification and discusses various NDT applications of PEC. It then transitions to robotic NDT, focusing on non-destructive techniques for aerial inspection, including thermographic, photogrammetry, and ultrasonic inspection methods.

Chapter 3 delves into the experimental studies conducted on the MAXWELL PEC P1 probe. It examines the probe's performance in measuring the thickness of carbon steels under various orientation angles, simulating conditions akin to those encountered with a hybrid-crawler UAV. The findings highlight the probe's accuracy and sensitivity, informing strategies for optimizing its deployment in NDT.

Chapter 4 first reviews the analytical model of feature extraction methods used to calculate material thickness. Then it details the design, fabrication, and analysis of a PEC sensor system aimed at mobile NDT of ferromagnetic materials. The chapter discusses the advantages of a dual-coil configuration, finite element analysis simulations, and the impact of various design parameters on the system's performance.

Chapter 5 explores innovative approaches for exterior pipe inspection using robotic systems, focusing on the development of a novel hybrid UAV-crawler equipped with an embedded PEC system. It demonstrates the system's capability to perform comprehensive, non-intrusive inspections, addressing the limitations of traditional PEC systems and enhancing the safety and efficiency of pipeline inspections.

The final chapter, Chapter 6, summarizes the key findings of the research, emphasizing the contributions made to the field of NDT. It discusses the implications of integrating PEC with UAV technology and proposes directions for future research. The chapter also outlines potential improvements in system sensitivity, applicability to various geometries and materials, and operational endurance.

1.6 Dissemination of Findings

1.6.1 Journal Articles Publications Arising from This Thesis

- **T. Zhao**, D. Zhang, R. Watson, W. Jackson, C. MacLeod, E. Mohseni, and G. Dobie, ‘Evaluation of Pulse Eddy Current for Autonomous Airborne Inspections’, *IEEE Sensors Letters*, vol. 8, no. 8, pp. 1–4, Aug. 2024, doi: 10.1109/LSENS.2024.3424910.

- **T. Zhao**, R. Watson, D. Zhang, R. McMillan, W. Galbraith, C. N. MacLeod, E. Mohseni, and G. Dobie, "A pulsed eddy current sensor for UAV deployed pipe thickness measurement," *IEEE Sensors Journal*, early access, 2024, doi: https://doi.org/10.1109/JSEN.2024.3450193
- R. McMillan, M. Tabatabaeipour, R. Hampson, C. Loukas, **T. Zhao**, R. S. Edwards, C. N. MacLeod, and G. Dobie, 'Characterization of EMAT guided wave reflectivity on welded structures for use in ranging,' *IEEE Sensors Journal*, vol. 23, no. 5, pp. 4383-4391, Jun. 2022.
- R. Watson, **T. Zhao**, D. Zhang, G. Dobie, C. MacLeod, S. G. Pierce, G. Bolton, and A. Joly, 'A Hybrid Unmanned Aerial Vehicle – Crawler for Full-Contact Airborne Pipe Inspection', *IEEE Transactions on Mechatronics (T-Mech).*, [Reviewed & Under Revision]

1.6.2 Conference Proceedings Arising from This Thesis

- **T. Zhao**, R. Watson, D. Zhang, J. Cao, E. Mohseni, R. McMillan, C. MacLeod, G. Dobie, P. Crouzen, and C. Forrester, 'Towards unmanned aerial vehicle-deployed pulsed eddy current for NDT', BINDT Webinar Week, Online, Sep. 08, 2021. [Online]. Available: https://www.bindt.org/events-and-awards/ndt-2021-webinar-week/abstract-6a4/
- **T. Zhao**, R. Watson, D. Zhang, E. Mohseni, C. MacLeod, G. Dobie, P. Crouzen, and C. Forrester, 'Automated Unmanned Aerial Vehicle Deployed Pulsed Eddy Current for Non-Destructive Testing', UoS Nuclear Showcase, Shaping the through-life vision for ANRC 2.0, Feb. 2023. Available:

https://www.strath.ac.uk/research/advancednuclearresearchcentre/news/showcase2023/

- R. Watson, **T. Zhao**, D. Zhang, M. Kamel, C. MacLeod, G. Dobie, G. Bolton, A. Joly, S. G. Pierce, and J. Nieto., ‘Techniques for Contact-Based Structural Health Monitoring with Multirotor Unmanned Aerial Vehicles’, in *Proceedings of the 13th International Workshop on Structural Health Monitoring*, Stanford University, Stanford, CA, USA, Mar. 2022, pp. 21–28.
- D. Zhang, R. Watson, J. Cao, **T. Zhao**, G. Dobie, C. MacLeod, and S. G. Pierce, ‘Dry-Coupled Airborne Ultrasonic Inspection Using Coded Excitation’, in *2020 IEEE International Ultrasonics Symposium (IUS)*, Las Vegas, USA, Sep. 2020, pp. 1–4. doi: 10.1109/IUS46767.2020.9251483.

1.6.2 Conference Presentations Arising from This Thesis

- R. Watson, **T. Zhao**, D. Zhang, J. Cao, C. MacLeod, G. Dobie, and S. G. Pierce, ‘Advances in Contact-Based Non-Destructive Evaluation using Unmanned Aerial Vehicles’, BINDT Condition Monitoring Conference, Online, Jun. 16, 2021. [Online]. Available: https://www.bindt.org/admin/Downloads/5A5%20-%20Watson.Robert.pdf
- R. Watson, **T. Zhao**, D. Zhang, G. Dobie, C. MacLeod, and S. G. Pierce, ‘Full-contact and immediate-proximity airborne inspection with a hybrid crawler-multirotor vehicle’, BINDT Condition Monitoring Conference, London, UK, Jun. 07, 2022. [Online]. Available: https://www.bindt.org/events/cm-2022/abstract-216/

- G. Dobie, R. Watson, **T. Zhao**, D. Zhang, C. MacLeod, and S. G. Pierce, ‘Full-Contact and Immediate-Proximity Airborne SHM with a Hybrid Crawler-Multirotor’, European Workshop for Structural Health Monitoring, Palermo, Italy, Jul. 04, 2022. [Online]. Available: https://www.ewshm2022.com/wp-content/uploads/2022/07/TechnicalProgram_04072022.pdf

Chapter 2 A Review of Related Work

2.1 Introduction

Non-Destructive Testing (NDT) is an essential technique in various industries for assessing the properties and integrity of materials and structures without causing any damage. NDT methods, such as liquid penetrant, magnetic particle, eddy current, and radiographic testing, as well as visual and ultrasonic methods, are crucial for ensuring the safety, reliability, and longevity of components in sectors like aerospace, automotive, and energy sector [12], [28].

Pulsed Eddy Current (PEC) technology is a highly effective NDT method for detecting corrosion and other subsurface defects in conductive materials. PEC operates by inducing transient eddy currents in the material under inspection and measuring the resulting magnetic fields [32], [33]. This method is particularly sensitive to changes in material properties, such as thickness variations caused by corrosion, making it invaluable for inspecting metallic structures like pipelines, storage tanks, and structural steel. This contactless method is particularly advantageous as it allows for the inspection of materials through coatings and insulation, which is a significant limitation for many other NDT techniques. The ability to measure through these layers makes PEC invaluable for inspecting metallic structures like pipelines, storage tanks, and structural steel, as it can detect thickness variations and corrosion without the need for direct contact [13], [15], [16], [17], [34].

Robotic NDT leverages advancements in robotics to enhance traditional NDT methods. By integrating robots into NDT processes, inspections can be conducted more efficiently and safely, particularly in hazardous or hard-to-reach environments. Robotic NDT systems can perform complex, automated movements and can deploy various NDT methods, including ultrasound, thermography, and X-ray inspection [35], [36], [37], [38]. This integration improves inspection accuracy, reduces human error, and increases the speed and repeatability of inspections.

Unmanned Aerial Vehicles (UAVs) have further revolutionized NDT by providing a flexible and mobile platform for conducting inspections. UAV-based NDT systems can access areas that are difficult or dangerous for human inspectors, such as high-rise structures, wind turbines, and large industrial plants. Equipped with various sensors and cameras, UAVs can perform visual [39], thermal [40], and ultrasonic inspections [29], [41], [42] from the air. Their ability to hover and manoeuvre precisely makes them ideal for detailed inspections and continuous monitoring, thus enhancing safety and efficiency by reducing the need for scaffolding or rope access.

This chapter will explore the state-of-the-art in NDT, PEC, robotic NDT, UAV-based NDT. It will review current academic and industrial developments, highlighting trends and challenges in this field. The focus will be on the advancements in PEC and UAV NDT technologies, demonstrating the potential of combining PEC with UAVs and how this innovative approach could potentially enhance the capability to measure the wall thinning for critical pipes.

2.2 Pulsed Eddy Current Inspection Techniques

2.2.1 Introduction

PEC technique is a non-intrusive, non-contact and emerging method of eddy current testing. It can detect corrosion and flaws within materials typically hidden under layers of coating, fireproofing, or insulation. Because of the rich spectral components leading to greater amounts of information about the component under testing, such as defect location in multi-layered components and increased stand-off distance allowing the detection of corrosion under insulation it has been applied widely to a diverse engineering field. These include examples such as aircraft [43] refineries and oil production facilities [44], high-speed rails and large nuclear steam pipes [43].

Conventional Eddy Current Testing (ECT) only applies a single frequency for excitation, which makes it unable to detect both surface and sub-surface defects reliably. An improved technique is multi-frequency ECT, which applies different excitation frequencies, one after another. Compared to multi-frequency ECT, PEC can potentially be applied in a shorter time for inspection of different depths as PEC applies broadband of frequencies in a single pulse. This allows reducing the measurement time to the minimum one depending on the sample characteristics.

In Pulsed Eddy Current (PEC) testing, the rising and falling edges of the pulsed excitation are theoretically represented by a Heaviside step function. The Fourier transform of this function is defined by:

$$\delta(f) = \frac{1}{i2\pi f} \tag{2.1}$$

Where $i = \sqrt{-1}$, f is the frequency, and $\delta(f)$ is the unit impulse function of f. This indicates that low frequencies can exhibit very high power. Achieving such high-power levels with a single low frequency is often limited by the capabilities of excitation circuitry. However, using a pulse allows for high power in the low-frequency range while also covering a wide frequency spectrum within the magnetic field. This enables PEC to achieve excellent penetration capability and generate a strong resultant magnetic field, as high power is concentrated at low frequencies, while high frequencies are present with lower power. Thus, PEC offers greater versatility compared to other Eddy Current (EC) techniques and is extensively used for assessing the condition of various materials, including ferromagnetic ones [45].

Given its capabilities, PEC is deemed the most suitable EC technique for this thesis's objective, which is the thickness estimation of critical pipe materials that are electrically conductive and ferromagnetic.

In the following subsections, the concept of PEC is discussed, which is then followed by the review in system configurations, PEC-based thickness quantification and applications.

2.2.2 Principles

The principles of PEC are similar to that of ECT. In terms of ECT, as shown in Figure 2-1, when alternating current is applied to a conductor, such as a wound copper wire, a magnetic field develops in and around the conductor. Then if an electrically conductive material is placed in the coil's dynamic magnetic field, electromagnetic induction will occur, and eddy currents will be induced in the material. In turn, eddy currents flowing in the material will generate their own secondary magnetic field, which will oppose the coil's primary magnetic field [17], [34]. Therefore, if a flaw or change occurs in the electrical conductivity, magnetic permeability or thickness of the tested material is found, the field will vary. A sensing device like a magnetic sensor or a coil, can be utilised to pick up the change [13].

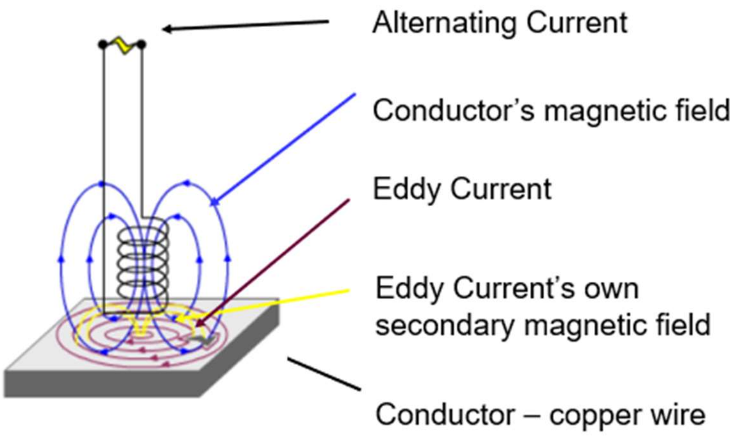

Figure 2-1: Process of how eddy current works [63].

The penetration depth and the density of the eddy current in the sample is an important issue in any ECT. The penetration depth is limited due to the skin effect, which causes the density of eddy currents to decrease exponentially with depth. The depth at which the density is reduced to $1/e$ of the density at the surface is termed the skin depth δ and is defined by:

$$\delta = \sqrt{\frac{2}{\omega\mu\sigma}} \tag{2.2}$$

Where δ is skin depth (m), μ is magnetic permeability (H/m), σ is electrical conductivity (S/m), and ω is the angular frequency (rad/s). The equation shows that the depth of penetration depends on the excitation frequency. The lower the frequency, the deeper the penetration and vice versa.

In contrast to conventional electromagnetic eddy current NDT technique, PEC utilises rectangular magnetic field excitation. A diagram of how the PEC principle works is presented in Figure 2-2.

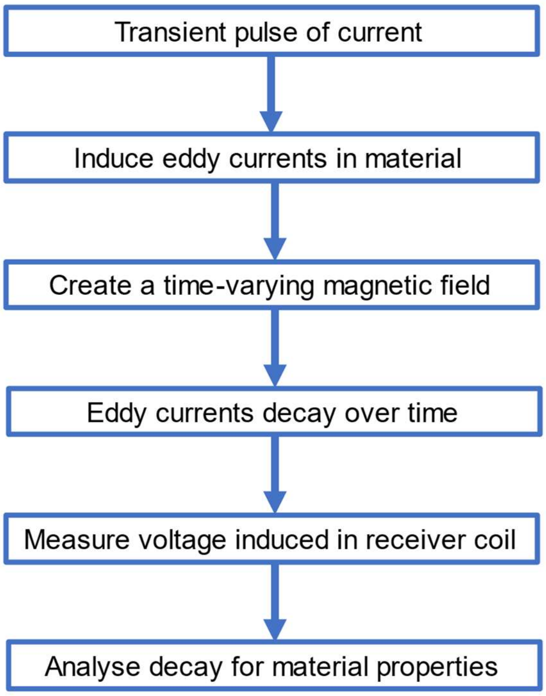

Figure 2-2: PEC principles.

The Fourier Transform of the pulse waveform components can be illustrated as

$$f(t) = \begin{cases} A, & -\frac{T}{2} \leq t \leq \frac{T}{2} \\ 0, & |t| > \frac{T}{2} \end{cases} \tag{2.3}$$

Where T stands for the pulse width and A is the amplitude of the pulse. Then the excitation amplitude spectrum can be defined as

$$F(\omega) = \frac{2sin\omega T/2}{\omega} \quad (2.4)$$

Pulses with different width examples are shown in the Figure 2-3. It shows that the excitation signal has a broad spectrum of frequencies. In this way, the PEC NDT technique can potentially be able to provide a wealth of information about defects with robustness against interference. Furthermore, the ability to inspect at different depths discriminatively and simultaneously in the material is possible when compared to the conventional ECT NDT technique [46].

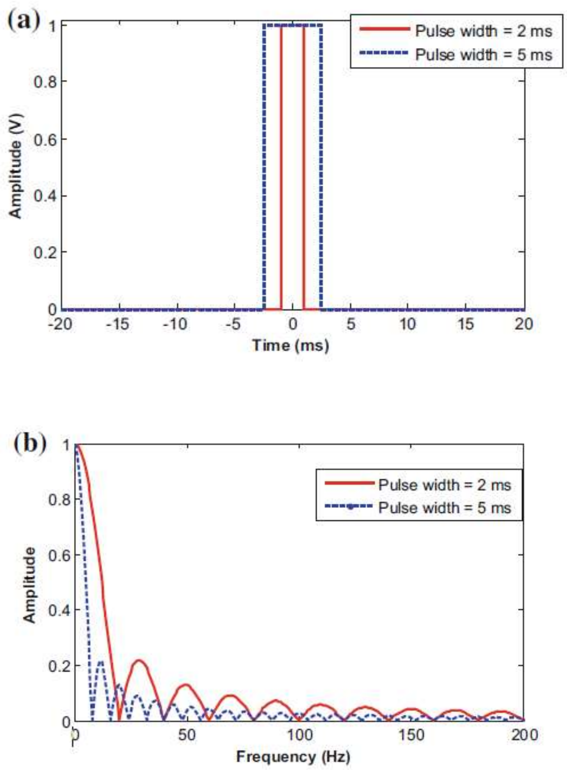

Figure 2-3: Pulses with different width examples [46].

2.2.3 Pulsed Eddy Current System Configuration

2.2.3.1 Excitation Signals

Different types and shapes of excitation signal have been proposed by PEC researchers over the years [13], [44]. The study on the influence of the excitation voltage on the received response signal for PEC NDT showed that excitation waveforms do not have a significant impact on the resolution of defect's depth. Therefore, the square excitation signal is preferable [47]. Additionally, a variable pulse width excitation has also been proposed, which was used in the inspection of subsurface corrosion in conductive structures [48], shown in Figure 2-4. This can provide different frequency spectra and is suggested of being able to eliminate the need for reference sample signal [48]. In the study of measurement of the liftoff of variable magnetic flux of PEC, the decaying part of the step signal can be used after the power of the excitation signal is disconnected [49].

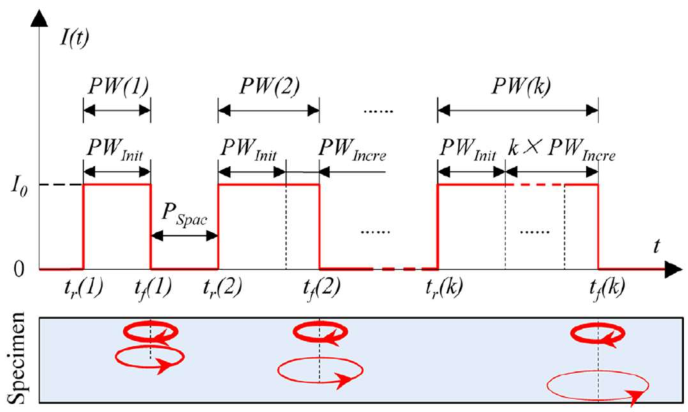

Figure 2-4: Variable pulse width excitation and the induced eddy currents [49].

2.2.3.2 Probe Configurations

Typically, a PEC probe would contain one excitation coil and one or more sensing devices. Probe designs are usually optimised in terms of the probe structure, sensing elements type and the cores deployed in different applications. The excitation coil and the probe can be categorised into three types: surface coil, encircling coil and internal coil, illustrated in Figure 2-5. The surface coil is usually used for both flat and curved samples [13]. Encircling coil can form an enclosing circle around the test object coaxially. Therefore, it can be used to inspect cylindrical insulated or coated structures [50]. However, this needs the outer diameter and the inner diameter of the coil to be large enough. The internal coils are mostly used to inspect hollow cylindrical structure from inside [17].

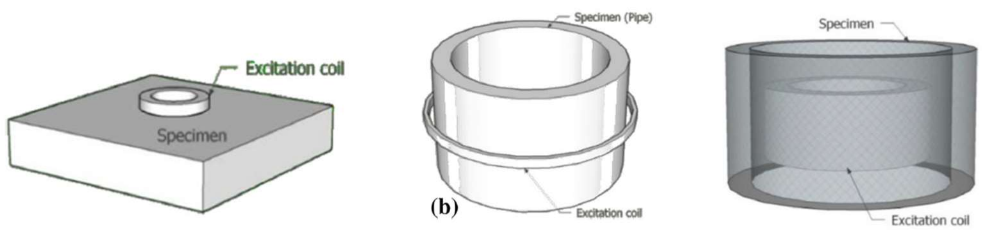

Figure 2-5: Coil types used in ECT: (a) surface coil, (b) encircling coil, and (c) internal coil [13].

In contrast to probes aforementioned, differential probes have the advantage of the self-nulling features, which means this type of probe doesn't need reference signals. This configuration has been mostly used in the crack detection instead of pipe thickness measurement [51]. Therefore, these variations are not of direct relevance to the work of this thesis and are not discussed in detail.

2.2.3.3 Sensing Devices

All PEC sensor architectures can be classified based on the type of detector used. Commonly used detectors include solenoid coils, superconducting quantum interference devices (SQUIDs), Hall-effect sensors, and magneto resistive sensors.

For the specific application of inspecting conductive ferromagnetic materials, PEC sensor architectures can be categorized into two types: (a) Detector coil-based architecture and (b) non-detector coil-based architecture. The former refers to sensors that use solenoid coils as detectors to sense the magnetic field, while the latter includes sensors that utilize other types of detectors such as SQUIDs, Hall-effect sensors, and magneto resistive sensors. Both sensor types of output can be given by

$$V_{coil} = -N \cdot A \cdot \frac{dB}{dt} \tag{2.5}$$

$$V_{mag} = K \cdot B \tag{2.6}$$

Where N is the number of turns of the coil, A is the area which the magnetic flux passes through, B is the magnetic field density, and K is the coefficient of the magnetic sensor [13].

Both the output signal of an induction coil and that of magnetic sensors are dependent on the value of magnetic flux density change. In this way, the response from the induction coil shares similar characteristics with that of the magnetic sensors when used in a PEC system.

In terms of induction coils, they have a wide frequency bandwidth and large dynamic range and are simple to operate. The size of the coil could be changed easily as well.

Induction coils are also the only option under extremely high-temperature conditions. Besides, it can detect an averaged representation of the material thickness or volume remaining under the footprint of the sensor [61].A typical cross-sectional view of the configuration of this architecture is shown in Figure 2-6. However, induction coils are only sensitive to AC magnetic fields, even if this disadvantage has been compensated by introducing movement to the coil [61]. Additionally, this architecture has limited sensitivity to fine and isolated defects [61].

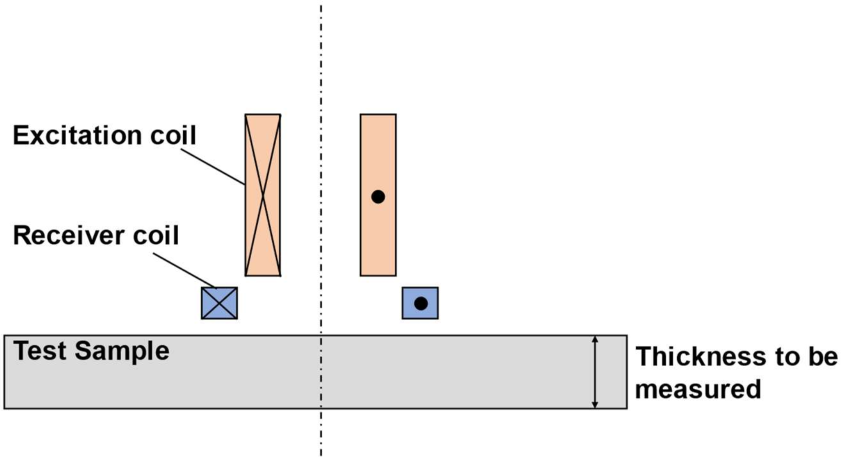

Figure 2-6: Cross-sectional view of the typical detector coil-based PEC sensor architecture used for ferromagnetic material thickness estimation.

This architecture has coils whose axis are perpendicular to the surface of the test piece. These probes can be either air-core coils or ferrite-core coils. Ferrites have high permeability and the initial coil impedance is higher than that of the air-core coils. Air-cored coils are the ones typically used for ferromagnetic material assessment [16], [53]-[61]. This architecture is generally suitable for evaluating flat surfaces [45], but this is also used on large diameter pipes [54], [62] as shown in Figure 2-7, since curvature of large pipes is low relative to the sensor size.

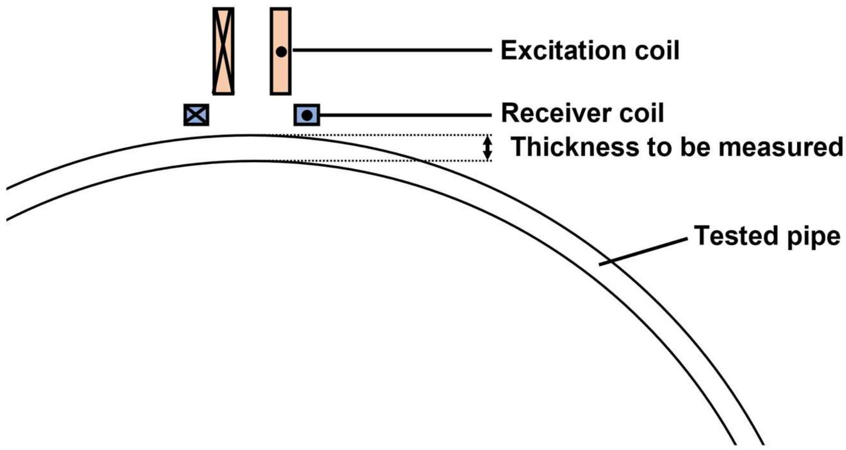

Figure 2-7: Cross-sectional view of the typical detector coil-based PEC sensor architecture used for pipe thickness assessment.

This architecture is known to be highly sensitive to lift-off (the vertical distance between an EC/PEC sensor and the surface of the test piece) and tilt [45].

As indicated in [51], when the pipe radius satisfies the condition $w/R < 0.25$, the sensor experiences less than 1% variation in τ. In the work of this thesis, the highest observed w/R ratio was 0.246, supporting the validity of treating large-diameter pipe surfaces as flat plates for practical purposes in the context of the analysis presented here.

Consequently, it is best suited for assessing the thickness of flat surfaces, with the sensor placed as parallel as possible to the surface. However, ideal conditions cannot be expected when assessing critical pipes with UAVs carrying PEC sensors, as the UAV's movement around the pipe can cause shaking and tilting. This instability makes using this architecture for UAV deployed critical pipe evaluation with existing signal processing and feature extraction techniques challenging. Therefore, this thesis employs the 'detector coil voltage decay rate' as a signal feature relevant to this architecture, as it shows reasonable insensitivity to lift-off [14], [56], [63-65], as detailed in Section 2.2.4.2.

In terms of magnetic sensors, they have been widely used to sense low-frequency magnetic fields [66]. A magneto resistive sensor was used in [67] to assess carbon steel pipe wall thicknesses up to 10 mm. [68] presented a method using a Hall-effect sensor supported by a ferrite core to evaluate stainless steel thicknesses up to 5 mm. The use of magnetization to improve the sensitivity of a sensor was proposed in [69] to detect and quantify subsurface defects in ferromagnetic steels. When applying this architecture to assess ferromagnetic materials, it has primarily been used for low-thickness steels such as 5 mm [70]. However, the objective of this thesis is to assess steels with thicknesses up to 20 mm. There is limited work suggesting the usability of this architecture on ferromagnetic materials, such as low carbon steel with high thicknesses. Consequently, this architecture is not preferred for this thesis.

2.2.4 PEC Based Ferromagnetic Material Thickness Quantification

2.2.4.1 Application Specific Noise Suppression Techniques

PEC signals are time varying induced voltages or currents in the detector due to the net magnetic field resulting from excitation and electromagnetic interaction with the test piece. Signals resulting from excitations used in practice are usually small in magnitude and do not exceed the millivolt scale irrespective of the type of detector. Given the small magnitude of signals, they are highly susceptible to noise [32]. Therefore, appropriate signal conditioning, noise suppression and amplification are essential to acquire signals in the quality suitable for extracting discriminative features to perform condition assessment.

Signal conditioning done in hardware is no different from any standard signal acquisition device as long as minimal distortion is introduced. Amplification and filtering are usually done before sampling and storing the signals. Operational amplifier-based amplification [71] and active filtering [72] techniques are used as in any common low voltage electronic system. [73] has presented the complete design and implementation steps of a PEC system. In [73], a second order Sallen and Key [72] low pass filter is used, and amplification is done using an instrumentation amplifier [74] before digital sampling. The hardware signal conditioning methods are not fixed by any means and there is freedom to use any filtering [75] and amplification [71] mechanism depending on the desired signal quality expected at the input of the sampling stage, however, minimal distortion is desired. Digital sampling networks are known to introduce noises which are unique to the sampling circuitry, and therefore software-based signal noise suppression is required to further cleanse the signals [73]. When it comes to software-based noise suppression, there are a few unique techniques which are used on PEC signals [73]. Some tailor-made methods for signals captured using detector coils have been researched and published as well [52], [53].

As in hardware filtering, the desired feature in software-based filtering techniques used on PEC signals is introducing minimal distortion since preserving the original shape of signals is essential to derive relationships between test piece geometry and signal features. Therefore, software implemented counterparts of commonly used filtering techniques such as Chebyshev, Butterworth and Bessel [76], are not generally used due to their tendency to introduce distortion. Instead, techniques such as acquiring multiple signals and averaging, Mean filtering and Gaussian filtering are used [73].

Averaging multiple signals which are synchronized is a useful distortion free noise suppression technique and is used in the digital signal processing stage of the commercial PEC signal acquisition unit and customised PEC sensor used in this thesis. Additionally, the techniques proposed in [52] and [53] are applied explicitly on detector coil-based signals and are more relevant to this thesis.

The work in [57] introduces a noise suppression method which improves the signal to noise ratio (SNR) up to about 40 dB. Improvement of signal discriminative capability resulted by filtering can clearly be seen in Fig. 2.5. The signals have been acquired for different thicknesses of steel using a step wedge Q235 steel plate at a constant lift-off of 20 mm. Steps included in the noise suppression method are:

1. Recording multiple PEC signals and calculating the averaged PEC signal,
2. Performing double logarithmic transform of the averaged PEC signal (refers to plotting both signal voltage and time in logarithmic scale),
3. Processing the signal from step (2) by median filtering,

Similar to [57], recording multiple signals and averaging was performed in the digital signal processing stage of the PEC signal used in this thesis. However, averaging alone is insufficient to achieve the desired signal quality. As such, a median filter, as applied in [57], was utilized to further suppress noise. The results in Figure 2-8 demonstrate that median filtering is effective in reducing noise in detector coil-based PEC signals. The jagged curves observed are a consequence of poor signal representation due to the low resolution in the digital-to-analog ratio, which can result in inaccuracies in signal interpretation. Therefore, particular attention has been given in this thesis to addressing this, with an emphasis on improving signal clarity through enhanced digital signal processing, as discussed in Chapter 5.

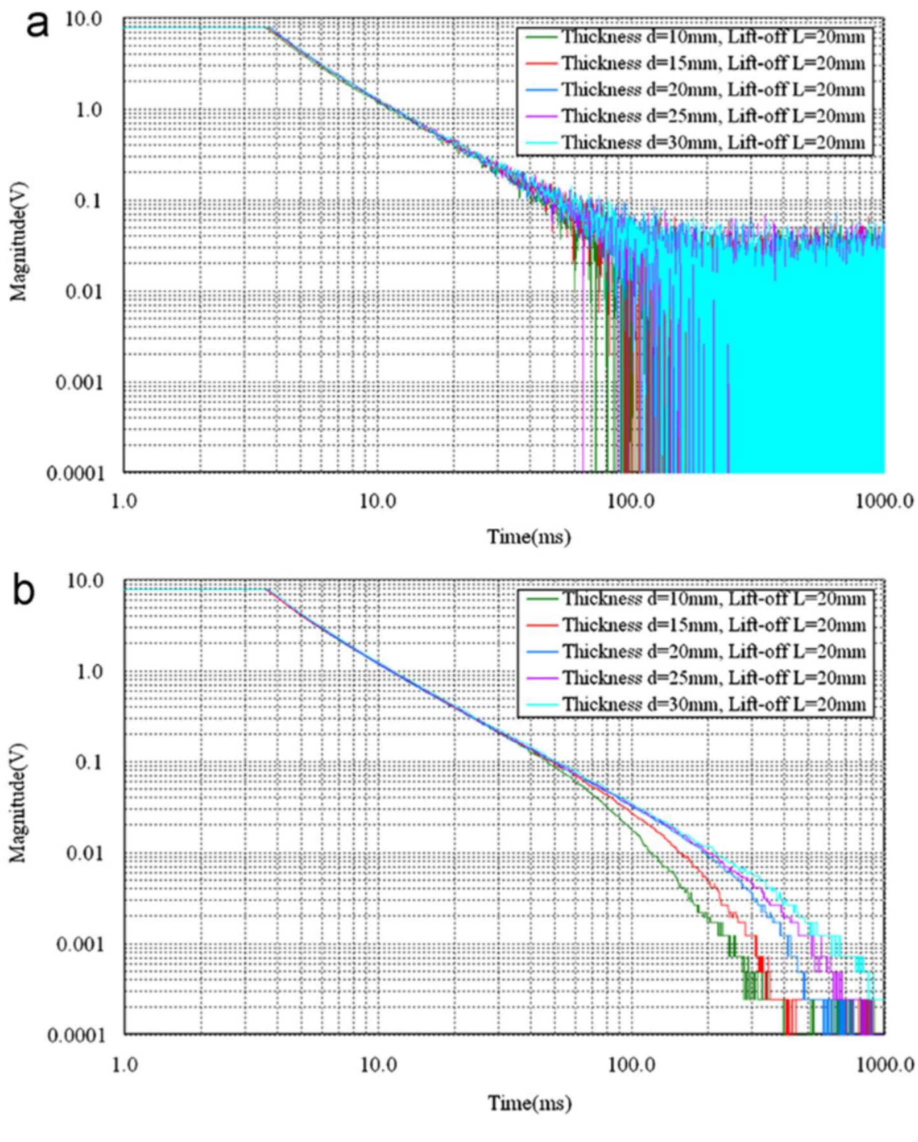

Figure 2-8: Comparison of signals before/after denoising [57]. (a) Signals before filtering and (b) signals after filtering.

The work presented in [53] introduces a distortion free noise suppression technique based on numerical cumulative integration. Figure 2-9 shows signals processed in [53] and the signals have been acquired on different thicknesses of Q235 steel.

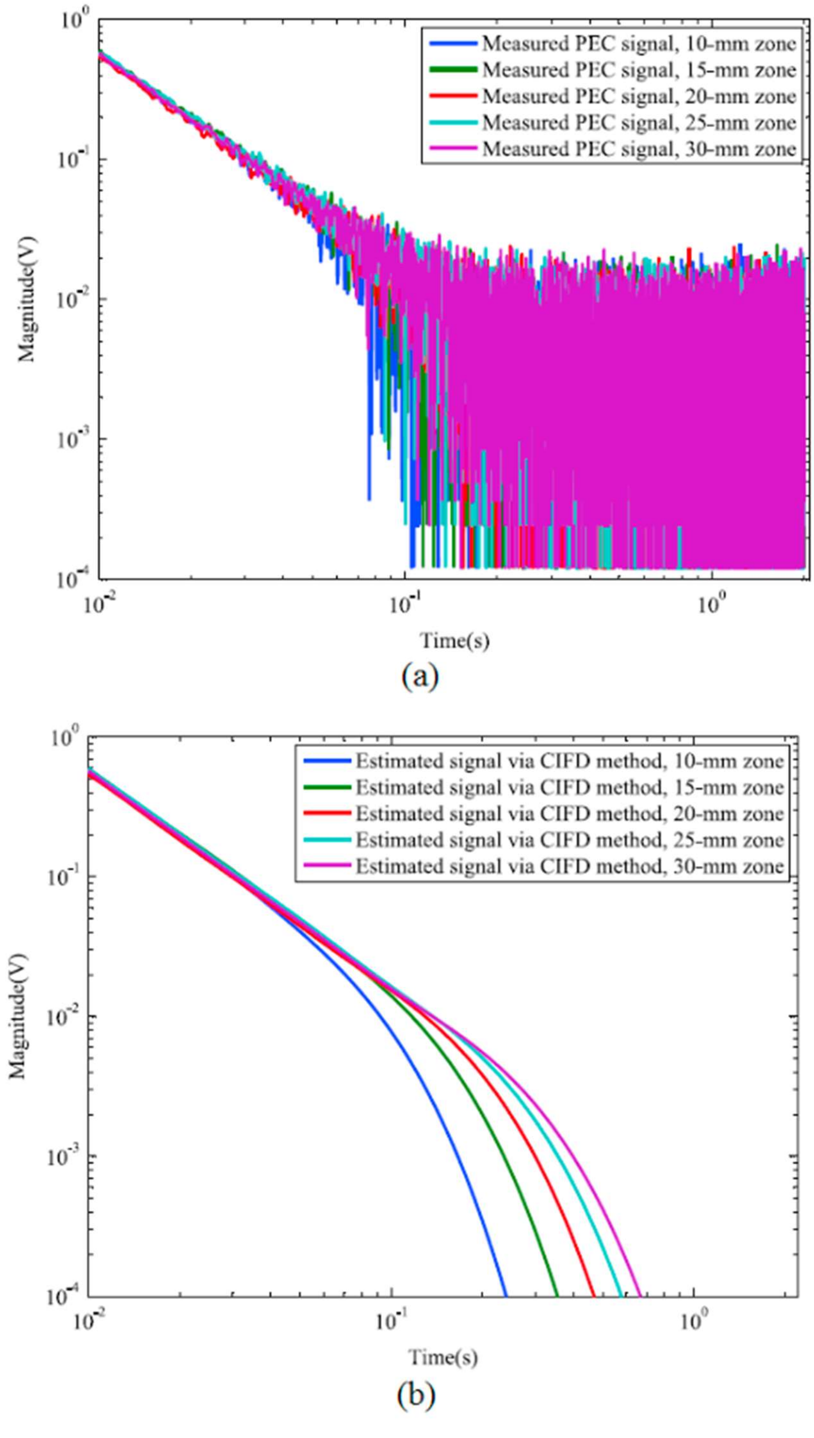

Figure 2-9: Detector coil-based PEC signals acquired on Q235 steel: (a) Signals before filtering; (b) Signals after filtering [53].

The time domain PEC signal (voltage induced in the detector coil) is integrated over time and an analytical model is fitted by approximating the cumulative integration of noise (average over time) to zero. Certain estimated analytical model parameters exhibit functional behaviour usable to quantify thickness of ferromagnetic plates. This noise suppression technique is highly desirable for PEC signal processing since it does not introduce distortion and therefore was considered incorporable for the work of this thesis. The approach of reducing noise is exploited in this thesis to fit a straight line to the late stage of the induced detector coil voltage to extract the "detector coil voltage decay rate" signal feature. Hence, the procedure followed in this thesis to extract the proposed feature uses the fundamental of approximating average noise to zero as done in [63], also following the method in work of [53].

2.2.4.2 Thickness Discriminative Feature Extraction Techniques

Traditional PEC signal features used for quantifying properties and defects in metal test pieces can be categorized into time domain signal features [55], [77], frequency spectrum features [68], [78], [79], principal components [80], [81], and integral features [82]. Among these, [55] focuses on ferromagnetic materials, while [68] and [78] evaluate stainless steel thicknesses up to 5 mm. The rest of the studies have been conducted on non-ferromagnetic materials with non-detector coil-based sensors, making them less relevant to this thesis.

The work in [68] and [78] utilise Hall-effect sensors to assess the thickness of stainless steel using power spectral density features. However, the thickness sensitivity has only been evaluated up to 5 mm. Since these signals are acquired using Hall-effect sensors rather than detector coils, the feature extraction methods are not directly applicable to this thesis. Additionally, these features have not been evaluated for higher thicknesses or other ferromagnetic materials carbon steels, which are the materials of interest here. Therefore, the feature extraction methods from these studies are not incorporated in this thesis.

The detector coil-based architecture described in [55] aims to find an efficient and straightforward signal feature for assessing ferromagnetic pipe wall thinning. Analytical modelling for a detector coil-based PEC probe placed over an insulated piping system is performed and verified experimentally. Two commonly used time-related features, peak value and time-to-peak are identified in the differential signal obtained by subtracting the test signal from a reference signal. Among these, the time-to-peak is found to be superior due to its linear variation with wall thickness. The influence of various practical testing conditions on the PEC signal is also investigated in [55], demonstrating that the time-to-peak is independent of insulation thickness and probe lift-off. The robustness of the time-to-peak feature to probe configuration is validated using three probes of different dimensions and structures. To determine the linear range of time-to-peak with respect to wall thinning, differential signals based on different reference thicknesses are examined. However, results indicate that the time-to-peak remains linear only for relative wall thinning of less than 60%, which is a limitation. Consequently, this feature extraction technique is not used in this thesis. Nevertheless, the technique could still be useful for calibration in periodic in-service inspection of insulated pipelines.

The work shown in [17] and [69] focus on defect identification in ferromagnetic materials. In [17], a remote field testing (RFT) sensor energized by PEC excitation detects axisymmetric surface slot defects on ferromagnetic tubes by examining variations in the induced detector coil voltage features. However, as this work focuses on defect detection using the RFT sensing technique, it is not applicable to this thesis. [69] proposes improving the sensitivity of time-domain reference-subtracted PEC difference signal features using magnetization to detect and quantify subsurface defects in ferromagnetic steels. Although effective for defect detection, their applicability to ferromagnetic material thickness quantification has not been examined, thus these feature extraction techniques are not included in this thesis.

Several analytical methods directly related to ferromagnetic material thickness quantification have been proposed [16], [83]. These methods are most closely related to the focus of this thesis. [83] and [54] have modelled Hall-effect sensor readings and PEC difference signals, respectively, on non-ferromagnetic materials. However, their sensitivity to thickness in ferromagnetic materials has not been evaluated, so they are not used in this thesis.

The work of [53] and [16] propose methods of fitting analytical models for detector coil-based PEC sensor signals, demonstrating significant thickness sensitivity of the induced detector coil voltage to ferromagnetic material thickness, achieving thickness detection up to 25 to 30 mm for steel. This level of sensitivity is highly desirable for critical pipe evaluation. Building on the theoretical models in [53] and [16], Ulapane et al. [84] proposed a novel PEC signal feature with low dependence on lift-off, sensor shape, and size, using the detector coil voltage decay rate to develop a thickness-feature function and estimate the wall thickness of in-situ critical water pipes up to 23 mm.

Because the PEC sensor is ultimately planned to be mounted on a UAV, the sensor will potentially encounter significant movement and vibration when the UAV is in operation. Therefore, immunity to lift-off distance is important. Consequently, this thesis chose the feature of detector coil voltage decay rate, which is suitable for in-situ critical pipe assessment.

2.2.5 NDE Application of PEC

Thanks to the aforementioned advantages of PEC, it has been used in a number of NDT applications, both in material characterisation and structural integrity inspection. For material characterisation, PEC has been used in the measurement of electrical conductivity and magnetic permeability [50]. In structural integrity inspection, PEC has been applied to the defect detection and characterisation of corrosion evaluation, measurement of insulation thickness, plate thickness and wall thickness of pipework. In these areas, both insulated and non-insulated, coated and non-coated materials are covered. In terms of UAV inspection and concerning this particular project, measurement of thickness and evaluation of corrosion will be mainly discussed.

Commercially, Ro¨ntgen Technische Dienst (RTD) – now known as Applus RTD – created a PEC system called RTD INCOTEST (INsulated COmponent TESTing) that can measure the wall thickness – ranging from 6 mm up to 65 mm – of both pipes and plates made of low alloy carbon steel, the system is capable of measuring through the insulation of up to 200 mm in thickness [85].

Another two companies, Eddyfi and Maxwell, also have similar PEC commercial NDT systems. In previous work conducted at Strathclyde University, Maxim et al.

[86] presented results of wall thickness evaluation of carbon steel pipes with internal and external corrosion using commercial PEC instrumentation, i.e. Eddyfi Lyft and Maxwell NDT. Results showed that wall thickness could be measured through insulation of 50 mm and through aluminium weather jacket up to 20 mm. The state-of-the-art PEC technology from Eddyfi Lyft has been reported to measure wall thickness up to 102 mm and insulation up to 305 mm with their PEC-152G2 probe [87]. However, it is important to note that these values are based on specific testing conditions and do not represent absolute upper limits of the technology.

2.3 Robotic NDT

2.3.1 Introduction

In this section, the current state of art in robotic NDT inspection systems from both academic and industrial aspects will be reviewed. Robotic NDT is that of the deployment of the NDT methods, including ultrasound, eddy current, thermography, visual inspection and X-ray inspection, etc., using robotics systems. These systems are capable of complicated automated motions as required for inspections. Because of the speciality and value the system can bring, a growing interest can be found in the development of robotic NDT system in manufacturing and in-service inspections at the current stage [88].

2.3.2 Fix Based Robotic NDT System

Typical fixed based robotic NDT systems are composed of cartesian systems and manipulators [89]. These systems are often used for the inspection of shaped components, with each machine used to inspect similarly shaped or sized components. These types of systems can be applied to most types of NDT, and the most commonly used ones are UT, EC and visual inspection.

Robotic manipulators have widely been developed for manufacturing applications and subsequently been applied to robotic NDT, with examples including robotic deployment of ultrasonic transducers within the Centre for Ultrasonic Engineering (CUE) at University of Strathclyde. Interfacing Toolbox for Robotic Arms (ITRA) has been created to allow the controlling robot arms update rates to reach up to 250 Hz, with the reaction time being as short as 30 ms [90]. Other ongoing research includes a hybrid force position control system developed by Mineo et al [91]. The system integrates high-accuracy KUKA KR90 R3100 with photogrammetry and phased array ultrasonic testing (PAUT) to enable automated, high-speed inspections, ensuring precise positioning and data quality through real-time path correction and advanced communication software, as shown in Figure 2-10.

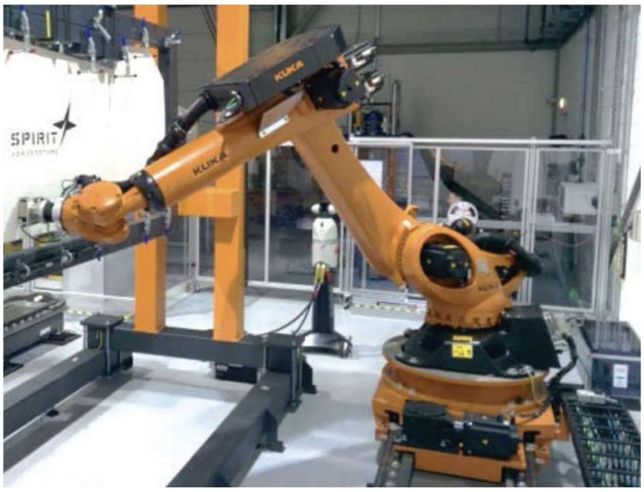

Figure 2-10: KUKA KR90 R3100 robotic manipulators [91].

2.3.3 Mobile Based Robotic NDT System

Another category of robotic NDT systems considered is mobile-based systems. These are robotic systems which are free to move around in their environment, moving to and around the inspection target. This section will focus on the applications and specifics of climbing robots for internal and external inspections, submersibles and a brief aerial platform.

The application of external climbing robots can be seen in many industries for inspections of different ferrous and non-ferrous surfaces. Most systems mentioned in this section are used for in-service, integrity asset inspection, overcoming safety concerns and speeding up the whole inspection process.

In the previous Strathclyde's work, a novel, autonomous reconfigurable robotic inspection system for quantitative NDE mapping was presented. The system consists of a fleet of wireless (802.11g) miniature robotic vehicles, each approximately 175 x 125 x 85 mm with magnetic wheels and carry one of a number of payloads including a two channel Magnetic flux leakage (MFL) sensor, a 5 MHz dry coupled UT thickness wheel probe (shown in Figure 2-11(a)) and a machine vision camera that images the surface, which is shown in Figure 2-11(b) [37].

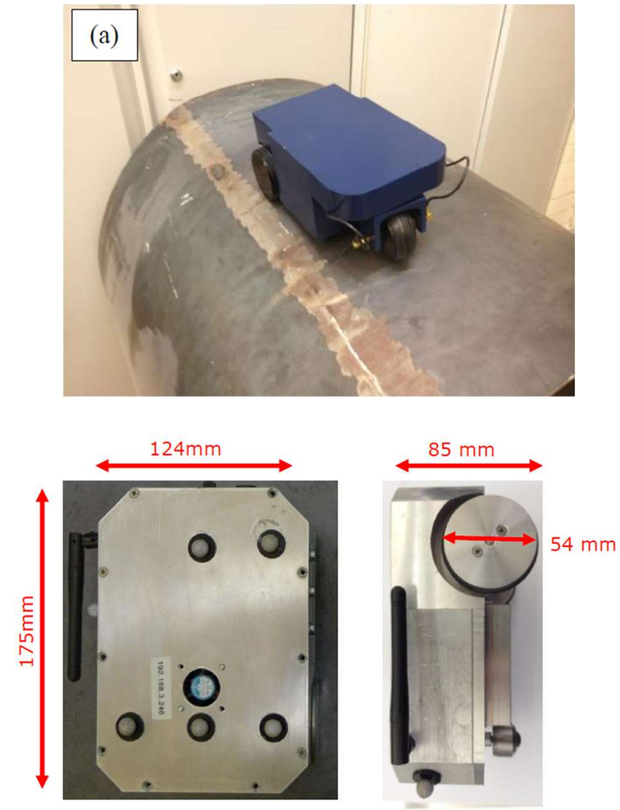

Figure 2-11: Wheel probe inspection robot, (b) Miniature robotic vehicle platform [37].

Structural Integrity Associates Inc in California [92] proposed a novel robotic crawler (shown in Figure 2-12) using dynamic pulsed eddy current technology to assess internal corrosion in piping configurations. This system utilises a robotic inline inspection (ILI) tool developed by Diakont, a manufacturer of advanced robotics and inspection equipment. The developed robotics inspection system can inspect piping with diameters ranging from 600 mm to 1400 mm, with the probe liftoff being approximately 15.9 mm for the 1067 mm diameter test spool and 15.2 mm for the 914 mm test spool. All measurement of defect depth can be within ±15% of the original wall thickness.

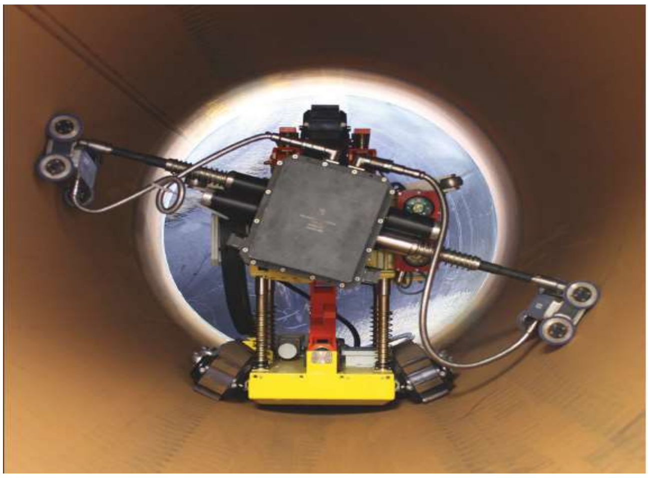

Figure 2-12: A novel robotic crawler with Pulse Eddy Current sensors [10].

Further industrial applications use visual methods for inspection, including the Helical robotics system which utilises a meconium wheeled scanning platform with permanent magnetic adhesion for enhanced manoeuvrability on large diameter pipes and vessels [92]. One bespoke system designed by Lufthansa (Figure 2-13) is utilised for thermographic inspection of aircraft [93]. The novel pneumatic suction cup design enables the inspection of non-ferrous structures. Similarly, pneumatic cup walking robot ROBAIR, shown in Figure 2-14(a) and Figure 2-14(b), was designed by Jianzhong et al. The robot has sufficient flexibility and stability in its structure. It can cope with a varying surface with a payload of a maximum 18 kg [38]. And for EC inspection of aircraft, the climbing robot (Figure 2-15) created by Sattar et al. uses X-ray tomography to inspect wind turbines. It was created as a prototype, leading to cost-effective development and laying the foundation of future crawler robot system design [94].

Figure 2-13: Testing of the Helical robot [93].

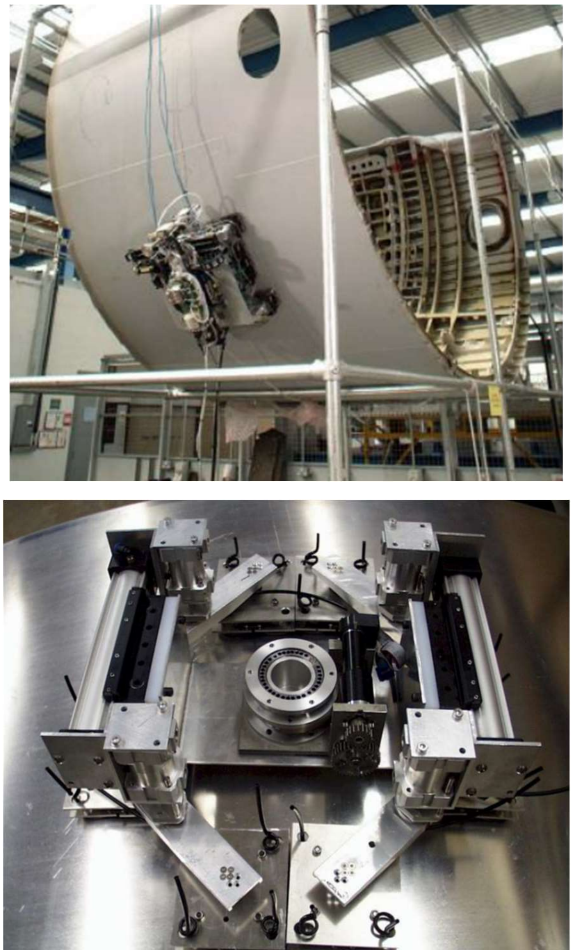

Figure 2-14: (a) Robot climbing on a D10 aircraft fuselage section (b) Overall Structure of the system [38].

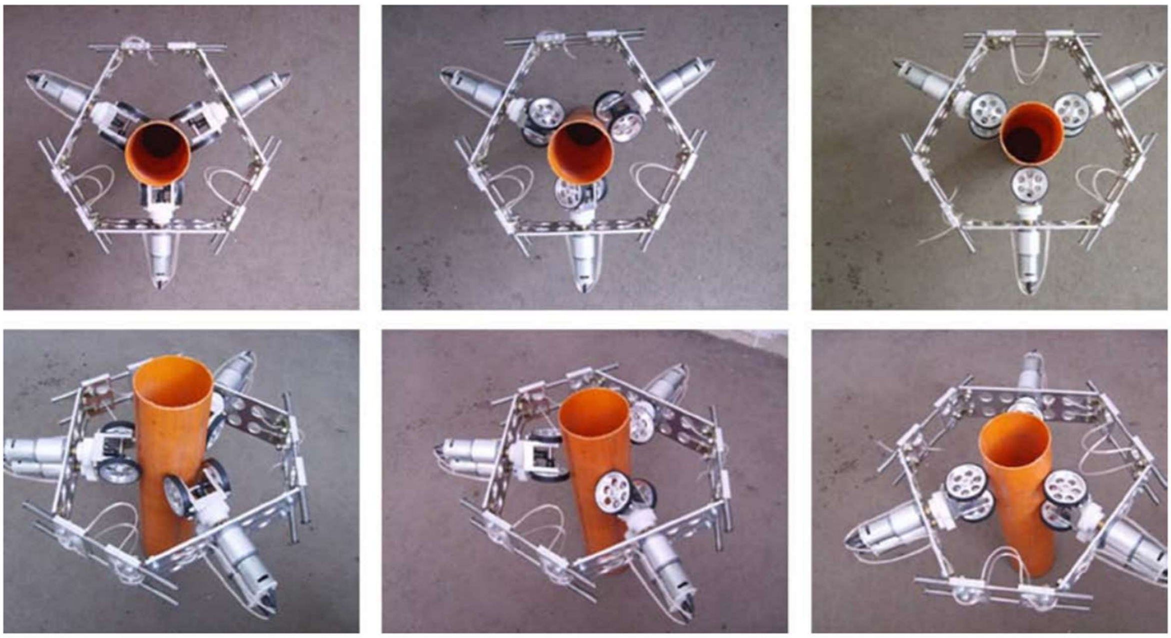

Figure 2-15: Prototype design in a small scale of wind turbine climbing robot [94].

The aerial robotic systems, which are also known as UAV system, have also seen growing development for overcoming access issues for inspections. These systems are primarily quad, hex or oct-copter based for academic or industrial use. A wide range of different types of aircraft, positioning methods and inspection techniques has been applied to both academic and industrial application, with more detailed literature review addressed in Section 2.4.

2.4 Non-Destructive Techniques for Aerial Inspection

2.4.1 Aerial NDE Introduction

In order to provide other practical solutions for the specific inspection requirements of the general industry, further requirements are needed in terms of mobility, flexibility and capabilities. The automated aerial NDE work platforms allow many inspection tasks to be conducted without restricting ferromagnetic material surface inspection or effect of gravity. The aerial NDE platform should be able to inspect not only ferromagnetic metal structures but also common composite materials as well [95].

Apart from the application aforementioned in Section 2.2, in terms of the UAV-based NDE, the application consists of visual or photogrammetric inspections [39], thermographic inspections [40], and ultrasonic inspections [41], [29], [42].

2.4.2 Thermographic Inspection

Thermographic inspection measures the characteristics of radiative heat in order to set areas or points with higher or lower heat emissivity, areas that could indicate the presence of a fault. Therefore, it can identify oil or gas leakage from damaged or worn structures, for example, underground pipelines [30]. Figure 2-16 is an example of Nimbus PLP6 during the thermographic monitoring operation.

Figure 2-16: Nimbus PLP6 during photovoltaic (PV) monitoring operation [30].

The key benefit of thermographic inspection is the absence of contact between the instrument and the measured object, so avoiding the thermal contact resistance effect [40].

The progress that instrumentation involved in aerial thermography has experienced during recent years has led aerial thermographic inspection to be the most suitable technique to identify underperforming PV cells at a PV site. Numerous researchers have started to prove its feasibility and suitability in this specific application during recent years, and significant advances in the field have already been made [40].

Paolo et al. [30] applied UAV with some thermal imaging cameras and a visual camera to monitor and scan PV modules, as shown in Figure 2-17. Nimbus EosXi UAV and Nimbus PLP6 are used as the aerial platform. Additionally, MicroCAM 640 and Nikon1-v1 are used as a thermal camera and an HD photo camera, respectively [40].

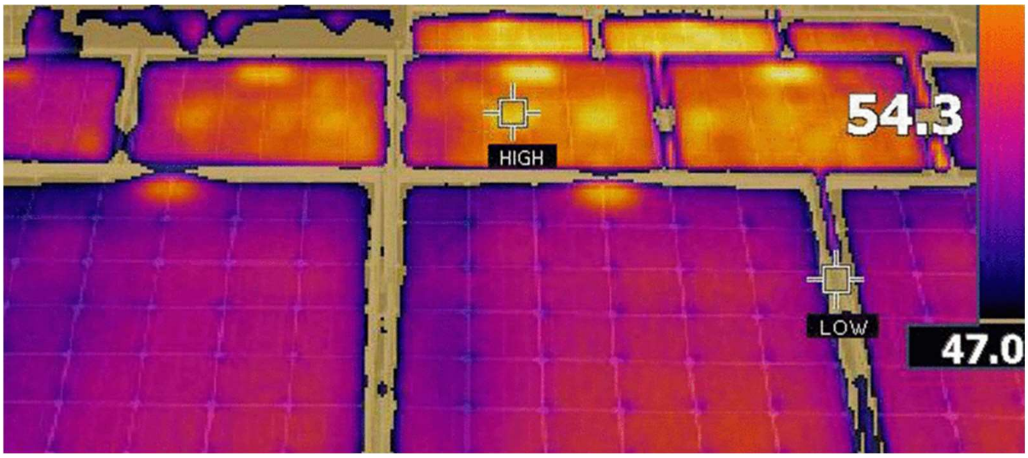

Figure 2-17: Thermal image of different PV modules [40].

2.4.3 Photogrammetry Inspection

A small high-resolution digital camera replaces the large metric camera, the combination of both is used as a platform for acquiring aerial images, so as called UAV photogrammetry [39]. It is regularly utilised as a method of NDT to find defects in large component structures, an example [39], [96].

In the existing literature, researchers mostly focus on higher accuracy and faster mapping with UAV photogrammetry inspection. For example, Han et al. proposed a vision-based approach for blade tip detecting and positioning using UAV. Well-tuned detector MASK R-CNN and shape constraints are used to detect the wind turbine structure, as depicted in Figure 2-18 [97].

Rojgar et al. discussed the use and the capabilities of UAV photogrammetry for producing topographic maps, and to assess the accuracy of these maps. Fixed-wing UAV eBee – Sensefly is used as the aerial platform and Pix4Dmapper software is utilised to process the digital images. For accuracy assessment, 2.1 cm in Northing and 7.5 cm in Elevation were obtained for Ortho mosaic and Digital Terrain Model

(DTM) respectively. Zhang et al. [96] at Strathclyde implemented the remote visual 3D reconstruction of the wind turbine blade with AscTec Firefly autonomous flight, to test the defects. The realignment deviation of 1.36 mm, with a light condition in the indoor environment was achieved. Figure 2-19 is an illustration of the 3D reconstruction deviation map.

Figure 2-18: 3D model outputs average F1-score obtained from UAV photogrammetry [97].

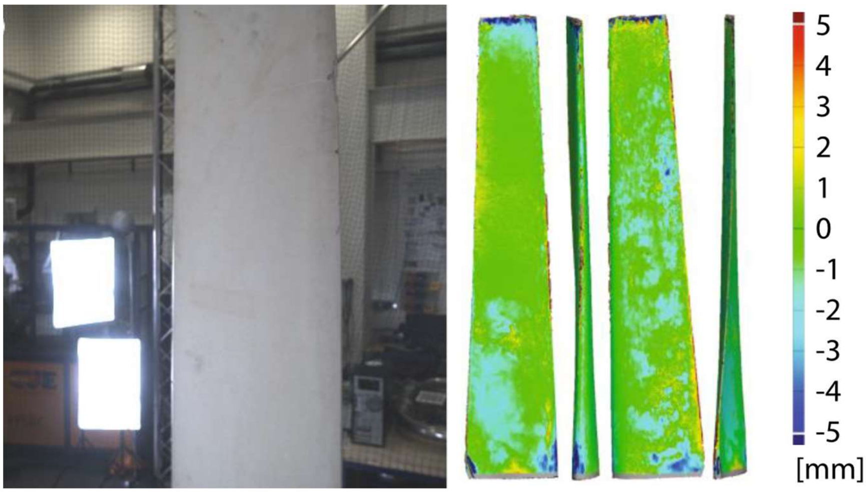

Figure 2-19: Deviation maps captured in 30ms shutter with light [96].

Nieuwenhuisen et al. [98] employed a similar approach for photogrammetric inspection inside a decommissioned industrial chimney, as illustrated in Figure 2-20. They began with a conical helix path based on the chimney's coarse dimensions, followed by ad hoc standoff corrections informed by feedback from a combined lidar and visual inertial stereo Simultaneous Localisation and Mapping (SLAM) system. To enhance the practicality of the assessment, they conducted a preliminary coarse reconstruction of the chimney's interior and unrolled the surface texture for on-site expert review. This method allowed for the immediate targeting of defects or visual anomalies for follow-up imaging before the final full-scale reconstruction, thereby improving inspection quality and avoiding costly return visits to the site.

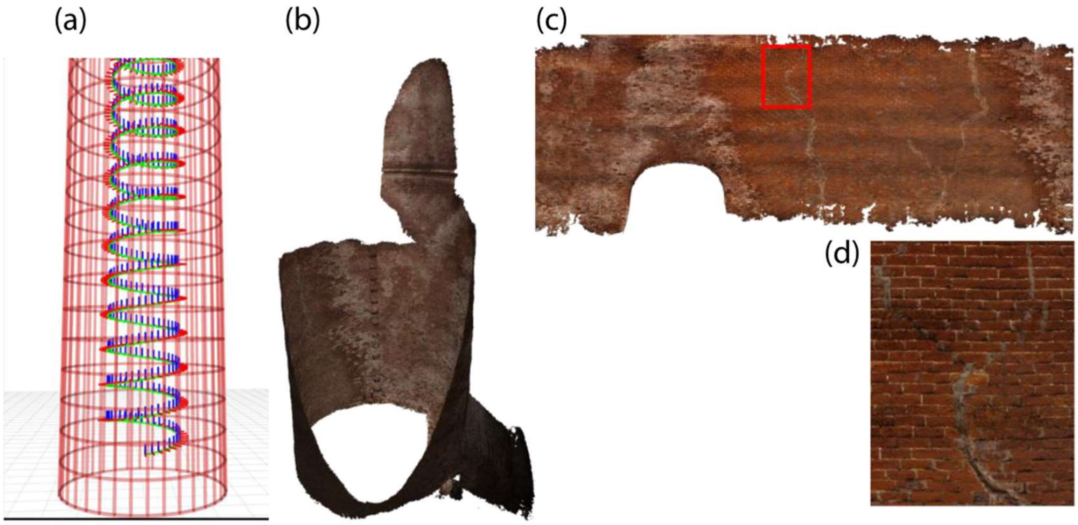

Figure 2-20: Automated photogrammetric inspection of an industrial chimney. (a) Flightpath planned with coarse geometry knowledge. (b) Textured mesh reconstruction of the chimney interior. (c) Unrolled surface texture. (d) Inset of region in red box showing crack formation.

Watson [99-100] et al developed and demonstrated an UAV platform, represents an innovative, dedicated platform with visual camera. This UAV model is equipped with six arranged reversible propellers, enabling the UAV to invert its thrust output completely. The arrangement includes four propellers inclined at 25° from the vertical and two tilted 15° above the horizontal plane, allowing for a combined thrust capability of up to ±30.8 N vertically and ±28.8 N horizontally relative to the drone's frame [99]. The UAV is equipped with two continuous rotation servos for movement, making it a hybrid between a drone and a robotic crawler. These servos, along with rigid legs that stabilize the UAV and can adjust to wrap around objects larger than 160 mm in diameter, ensure precise contact and navigation around the target. Figure 2-21 depicts the successful inspection image of the weld cap and pipe surface.

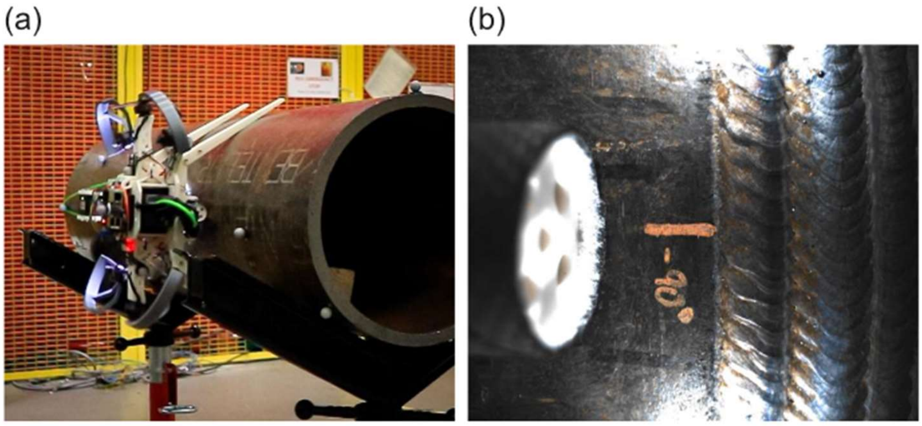

Figure 2-21: Synchronised photographs of the UAV inspection. These show: (a) the vehicle and (b) an unprocessed image captured while in motion passing the -90° clockface angle [100].

However, the photogrammetric inspection method cannot tell minute discontinuities or deformations beneath a surface coating [41]. Additionally, during the UAV asset inspection process, the UAV needs to approach the inspection object closely. Due to the influence of wind, it is predicted that the UAV will collide with the inspection object. When the airframe comes into contact with the inspection object, problems arise with the camera image provided by the camera mounted on the airframe [101].

2.4.4 Ultrasonic Inspection

Ultrasonic inspection is a NDT method commonly used in corrosion mapping. One of the drawbacks of thermographic and photogrammetric inspection techniques is that they can only identify visible discontinuities and other prominent surface-exposed defects. However, ultrasonic inspection can detect sub-surface corrosion beneath the exterior façade. Therefore, ultrasonic inspection is introduced for aerial NDT applications.

Dayi et al [29] have developed an autonomous UAV system with an integrated ultrasonic contact-based measurement payload, whereby the AscTec Firefly UAV is used in this application and equipped with ultrasonic payload, shown in Figure 2-22. A 5 MHz, dual-crystal ultrasonic transducer is held in a spring-loaded mounting structure to ensure an appropriate contact force while ultrasonic acoustic energy is transmitted through the coupling gel. Using this system, measurements were conducted in a region of the aluminium sample with a nominal thickness of 12.92 mm, reporting the thickness with a 0.03 mm error. However, aerodynamic factors cause alignment errors during the autonomous inspection process, leading to measurements with a low Signal-to-Noise Ratio (SNR) [29].

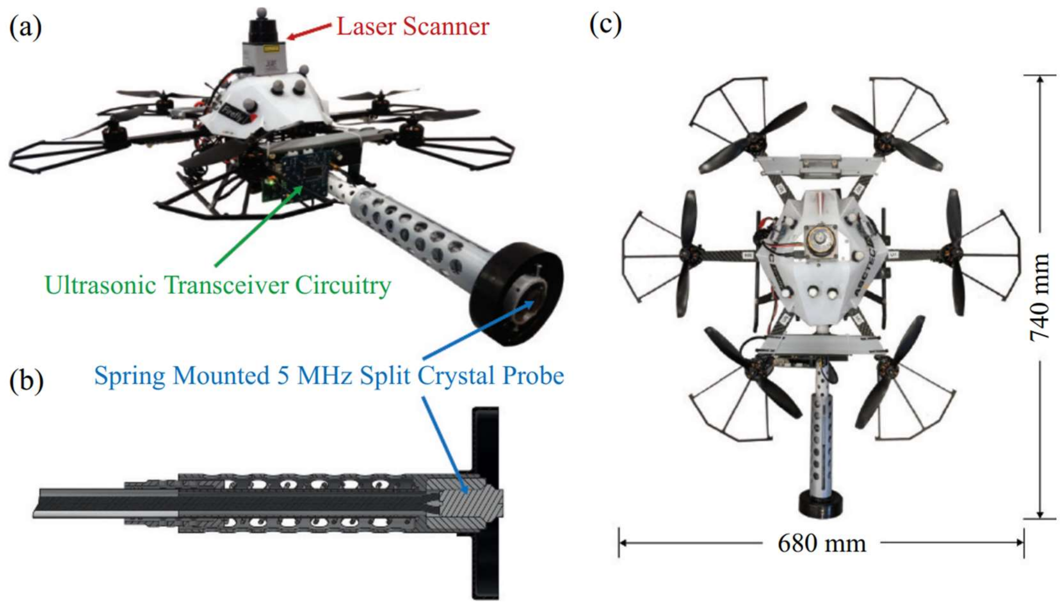

Figure 2-22: (a) AscTec Firefly UAV equipped with ultrasonic payload (b) Cross-section of the spring-loaded arm mechanism (c) The UAV system top-down view and bounding dimensions [29].

Watson et al [42] also presented an over-actuated multirotor (shown in Figure 2-23(a)), to deploy a dry-coupled ultrasonic wheel probe as a novel means of mapping wall thickness loss due to corrosion [82]. In point thickness measurements of an aluminium sample mounted in the vertical plane with geometry representative of corrosive wall loss, a mean absolute error of under 0.1 mm in thickness can be obtained. When accessing the underside of a near 45° overhang (Fig. 2-23(b)), stable interaction similarly enabled thickness measurements with comparable error margins. It is important to note that these error margins are primarily due to sensor limitations, while the UAV's over-actuated design effectively mitigated vibration-induced errors. Lastly, in the surface scanning modality, the wheel probe was rolled along the sample length (Fig. 2-23(c)), providing sufficient data to accurately resolve stepped thickness changes. These changes, representative of corrosion features, were detected at a spatial resolution of 20 mm, meaning the system was able to distinguish thickness variations with a feature size as small as 20 mm along the scanned surface [42].

(a)

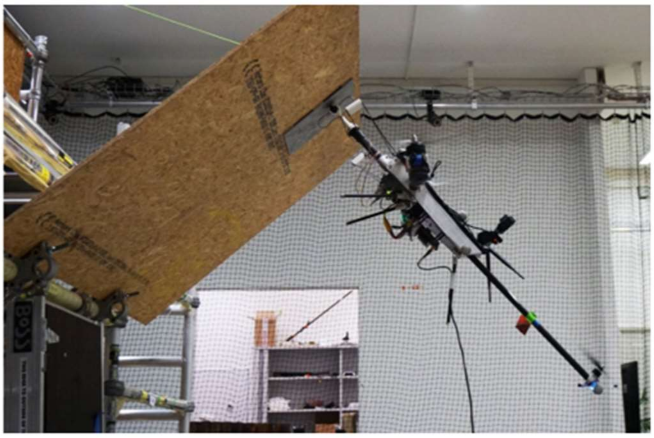

(b)

(c)

Figure 2-23: UAV Voliro Platform [42]: (a) A simple interaction with the vertically mounted aluminium plate (b) The Voliro manipulator platform is able to enter and maintain stable contact with the underside of an overhanging surface, with the inclination of the overhang is approximately 45° (c) The Voliro UAV scans across the stepped-thickness aluminium bar.

2.5 Conclusion

This chapter has provided an extensive review of PEC technology, robotic NDT systems, and advancements in aerial NDT inspection. PEC remains a valuable tool for inspecting conductive materials, especially when examining subsurface defects and corrosion. The ability to detect material thickness variations through coatings and insulation enhances its applicability across industries such as oil and gas. Additionally, integrating NDT technology into robotic platforms, such as UAVs, offers novel potential solutions for remote and hazardous inspection scenarios, improving safety and accessibility. Several techniques, such as thermography, ultrasonic inspection, and photogrammetry, were reviewed for aerial NDT, further highlighting their contributions to efficient infrastructure monitoring.

Despite the advancements in PEC technology, the research gap remains in integrating traditional PEC systems with UAV platforms for aerial NDT applications. One major issue is the bulkiness of conventional PEC sensors, which makes them difficult to mount on UAVs, limiting their flexibility in real-world applications. Additionally, most existing systems face challenges related to sensor accuracy, vibration management, and inspection limitations over large or insulated surfaces. This project seeks to overcome these challenges by developing a compact, lightweight PEC system specifically designed for UAV-based inspections. The system will be mounted on a customized UAV-crawler vehicle to perform detailed pipe inspections, addressing both aerial and surface-level constraints effectively.

Chapter 3 Characterisation of Pulsed Eddy Current Sensor for Autonomous Airborne Inspections

3.1 Introduction

With an increasing and focused emphasis on human safety and environmental protection [20], there is a growing need for detailed information regarding the current status and condition of global infrastructure. Rising operational requirements, such as higher working loads and extended service lifetimes, along with reduced capital investment in new infrastructure, have placed significant stress on various components [103]. This has critically impacted their condition and safe operational lifespan [104]. To equip infrastructure owners, operators, and planners with the necessary information about the state and condition of their assets, significant progress has been made in the field of NDT [105], [106].

One of the NDT methods, PEC technique, can detect corrosion and flaws within materials typically hidden under layers of coating, fireproofing, or insulation. Because of the rich spectral components leading to greater amounts of information about the component under testing, such as defect location in multi-layered components and increased stand-off distance allowing the detection of corrosion under insulation, it has been applied widely to a diverse engineering field. These include examples such as aircraft [43], refineries and oil production facilities [107], high-speed rails and large nuclear steam pipes [43].

Notably, PEC sensing plays a pivotal role in the non-invasive identification and measurement of the physical and geometric attributes of metal specimens. This technique operates by measuring the magnetic field resulting from a specimen positioned next to a sensor that emits a pulsed magnetic wave. Of the various geometric attributes gauged, the thickness of wall-like specimens is crucial for monitoring the integrity of metal structures [55], [108]. Given that some of these wall-like formations are ferromagnetic, eddy current sensing emerges as a preferred choice among the spectrum of other sensors when it comes to determining the thickness of such ferromagnetic substances [17], [58]. Building on this foundation, this chapter zeroes in on utilizing PEC sensing to gauge the thickness of ferromagnetic wall-like entities. Compared to other NDT techniques, PEC does not require direct contact with the material, making it advantageous for rough or inaccessible surfaces [43]. In addition, it is beneficial for autonomous inspections where ensuring good contact is challenging during robot manipulations. Despite its promising applications, the impact of these challenges on the accuracy and reliability of PEC measurements, particularly in autonomous UAV operations, remains underexplored.

The fusion of NDT techniques with robotic inspection platforms offers enhanced performance and broader coverage. Previously, the PEC sensor was introduced on the crawler for manoeuvrability and accessibility [92]. It used a contact wheel probe to measurement the inner surface of the pipe. However, it does not address the challenge of accessing the inner surface of a pipe. Because of the enhanced manoeuvrability, capability, and accessibility of UAVs, this robotic platform can not only access the outer surface but also be equipped with NDT inspection payloads, which have been commercialized in many applications using photogrammetry [39] and thermographic inspection techniques [40]. Additionally, a novel UAV-Crawler hybrid platform, which has been developed at University of Strathclyde [100], is different to existing commercial UAVs in that it is able to crawl about the asset surface, performing a fly-crawl-fly inspection strategy.

The PEC sensor utilized in these trials was manufactured by MAXWELL NDT Ltd [109], chosen due to its availability to the research team. The system consists of a data acquisition unit for data collection and analysis. The system includes four probes, each designed for a specific lift-off range to maximize detection capabilities. The smallest probe is ideal for applications requiring less weight without sacrificing inspection quality. While originally designed for manual inspections, these sensors are equipped with specifications enabling accurate assessments across diverse conditions. However, integrating the sensor into an aerial inspection platform could surpass its designated capabilities. Hence, it is essential to comprehend the sensor's specifications in the context of airborne inspections.

This chapter focuses on evaluating the sensor performance which influencing measurement accuracy in autonomous airborne PEC inspections. It investigates sensor tilt angles to understand how deviations affect measurement accuracy, crucial for reliable readings in real-world scenarios with positionally uncertain robotic deployment or complex or uneven surfaces. In the following subsections, the detailed characterisation of the Maxwell Pulsed Eddy Current Technology (PECT) Tool is performed.

3.2 MAXWELL NDT PECT

The PECT instrument, shown in Figure 3-1, uses the PEC principle illustrated in Section 2.2.2. It is a very compact and innovative PEC kit, which has been developed by MAXWELL NDT Ltd. in The Netherlands. The inner life of the kit combines a compact detector coil-based PEC probe and a windows-based tablet computer with a LabVIEW-based data acquisition (DAQ) unit. It captures two measurements per second. The probe is connected to the DAQ unit through an armoured cable.

Figure 3-1: The Maxwell PECT Probe kit [109].

The whole instrument relies on a high-energy magnetic pulse and weights 7.2kg, including the batteries in the tablet computer. The battery types come with external chargers and are hot-swappable. It also features four standard probes, each optimized for different lift-off ranges i.e., types S (Small), M (Medium), L (Large), XL (Extralarge), ensuring defect sensitivity. The whole kit can be applied to ferromagnetic steel with wall thickness between 2.5mm to 65mm, with the lift-off from 0mm to 250mm.

The system diagram of the system is illustrated Figure 3-2. It begins with a rectangular waveform generator producing an electrical signal, which is amplified by a driver circuit to power an excitation coil. This coil induces eddy currents in the sample, and a detector coil measures the response. The signal from the detector coil is conditioned and collected by a data acquisition system. The data undergoes feature extraction and characterization to determine the PEC thickness results of the sample.

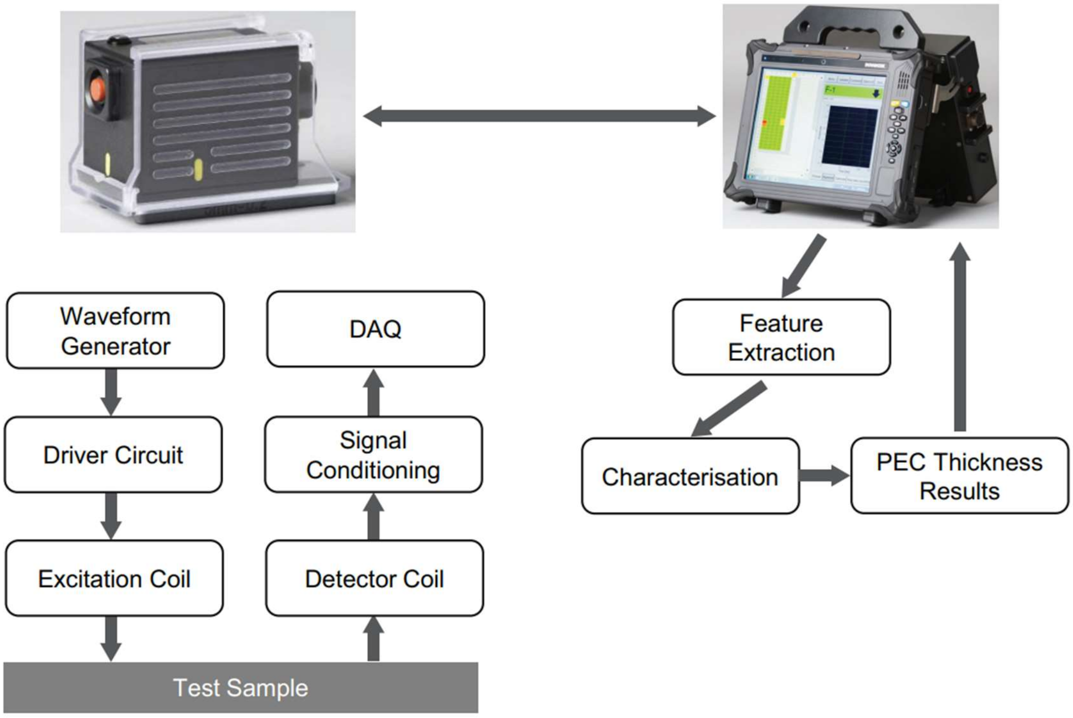

Figure 3-2: Maxwell PECT system diagram.

However, unlike the probe used in [39], the type S (Small) probe is chosen for this project to minimize the payload of the aerial platform. This smallest probe is ideal for applications requiring less weight without sacrificing inspection quality, with a nominal lift-off range from 0 to 20 mm. The C-scan results could be saved as data files and be exported using the PECT Analysis software (Figure 3-3). At the same time, users are allowed to export the amplitude received from the probe and the corresponding time. In this way, the certain amplitude signal obtained on the steel sample for the full range could be plotted (Figure 3-4).

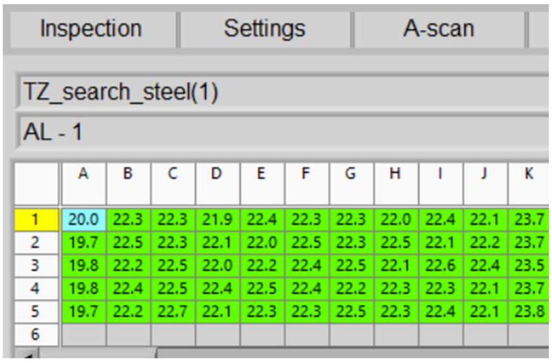

Figure 3-3: Maxwell ground station software user interface.

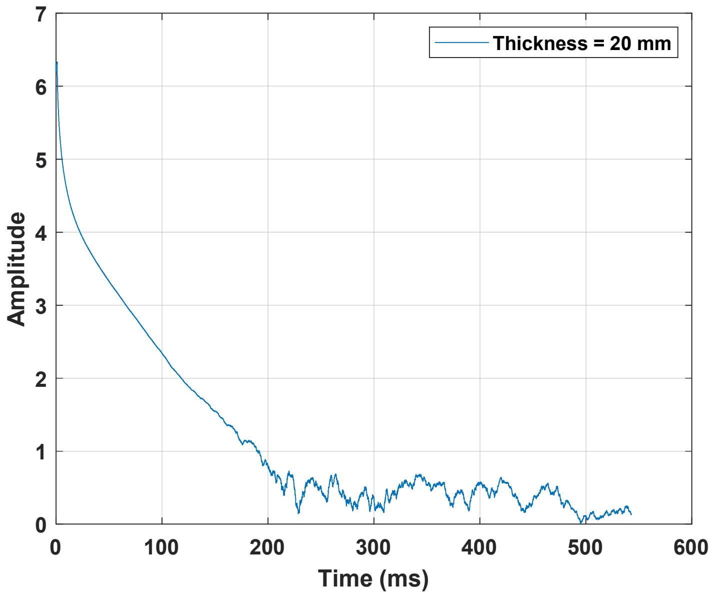

Figure 3-4: Obtained amplitude for the 20 mm thickness sample.

3.3 Experimental Assessment Methodology

3.3.1 Robotic Measurement Facility

In [100], an Multidirectional Thrust (MDT) configuration UAV-crawler was introduced, with six 5-inch, fixed-pitch, reversible propellers hexagonally distributed about the airframe. A photogrammetric sensor was positioned onto the platform, to identify visible discontinuities of the pipe sample. However, this visual measurement is only capable of identify prominent surface-exposed defects. To inspect internal support material corrosion and fatigue crack formation beneath an outer surface coating, the Maxwell PECT sensor has the potential to be employed onto the platform.

It may be readily realised from practical experience that probe alignment error causes signal attenuation when the probe face is not parallel to the target surface [13]. This experiment is thus designed to measure the alignment constraints of the sensor and quantify their impact on inspection accuracy in the larger context of the UAV deployment. Hence, the PEC probe was mounted on the end of a KUKA KR6 R900 sixx: an industrial, six-degree of freedom, robotic manipulator arm [110].

Compared with the probe vibration when mounted on the UAV, the KUKA robot can deploy the sensor to much more precise positions granting the experiment repeatability and providing more accurate quantification results. Utilising the internal pose feedback, the robot pitch, roll and yaw angles and (x, y, z) translations, measured with 0.01° angular and 0.01 mm translational resolution respectively, were manually adjusted to move the PEC probe. Additionally, the measurements under this setup are not influenced by interference from the UAV motors. In conducting the assessment, the probe is triggered by the commercial software at the control panel end and its output signal digitised by the customised PEC software described in Section 3.2.

In the probe's body reference frame, as shown in Figure 3-5, the alignment of the probe was controlled to be normal to the y-axis of the positioner across all tested ranges. Similarly, the lift-off distance was precisely maintained at 5 mm as measured by the robot's z-axis feedback. The arm of the robot is manually manipulated to adjust the probe within a ±4◦ range in roll, pitch, and yaw, incrementally changing by 2◦ steps. ±4◦ was selected as the upper limit for reasonable and meaningful thickness measurements. For each orientation, five measurements were conducted to reduce uncertainties during the measurements.

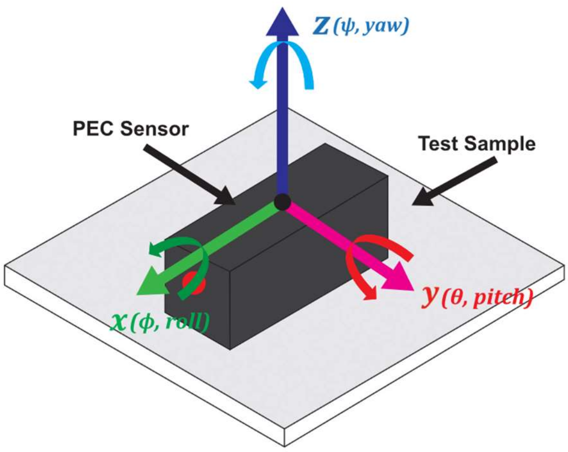

Figure 3-5: PEC probe's body reference frame.

Measurements were conducted for five different lift-off distance scenarios with nominal values of 0.0 mm, 5.0 mm, 10.0 mm, 15.0 mm, and 20.0 mm. As shown in Figures 3-6 and 3-7, each steel sample of varying thickness was horizontally attached to the robotic inspection platform, serving as the inspection target for this experiment. The robotic manipulator approached the sample vertically, ensuring that the probe was aligned with the centre of mass of the sample. To achieve this, the tool calibration was conducted using a manual approach, where the KUKA tool was calibrated by aligning the Tool Centre Point (TCP) with the marked area on the sample. This was done manually by eye. The manual calibration process provided sufficient accuracy for the inspection scenario, ensuring that the probe remained parallel and centred with respect to the sample's surface.

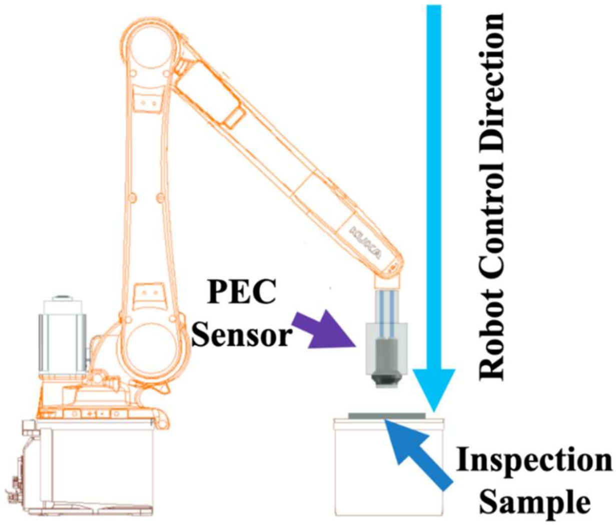

Figure 3-6: Robotic manipulator setup for the quantification of alignment constraints.

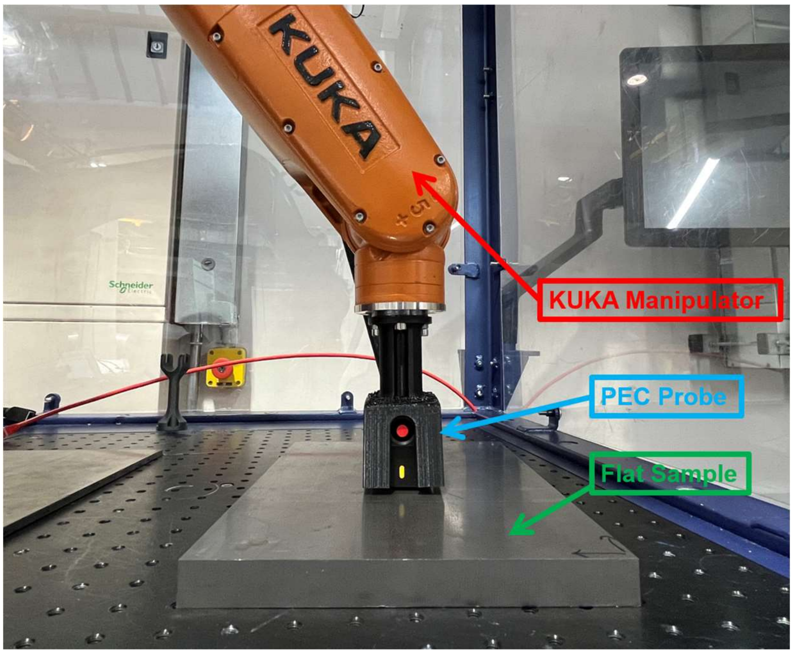

Figure 3-7: Practical robotic manipulator set-up.

3.3.2 Inspection Samples

The sample are low carbon steel flat bars of 300 mm long, 200 mm width. Three different thicknesses were investigated, of nominal thickness values 6.0 mm, 10.0 mm, 20.0 mm separately, shown in Figure 3-8. These thicknesses were chosen to accurately represent the variety of pipes typically used in industries. The use of uniform and flat plates was adopted to establish a controlled baseline for assessing sensor performance. Uniform structures are essential for performance validation because they offer consistent properties that enable precise evaluations of sensor accuracy and repeatability. This ensures that any deviations observed are due to the sensor itself rather than inconsistencies in the structure. Flat plates were selected to simplify the test environment, minimizing the impact of external factors such as curvature, surface roughness, and thus providing a clear benchmark for the sensor's capabilities. In addition, no coatings or variations in thickness were applied to guarantee that the sensor's measurements were solely influenced by the alignments, avoiding any masking of the sensor's true performance and sensitivity by different material properties or layering effects.

Figure 3-8: Experimental samples of 20 mm, 10 mm and 6 mm thickness separately.

3.3.3 Thickness Error Quantification

For every individual value in the measurement process, the error in thickness was determined as the shortest vertical distance from the top surface point to the bottom one of the samples. However, it must be noted that when the probe is tilted with the angle α_z, β_z then γ_z, the measured thickness values change correspondingly, as shown in Figure 3-9.

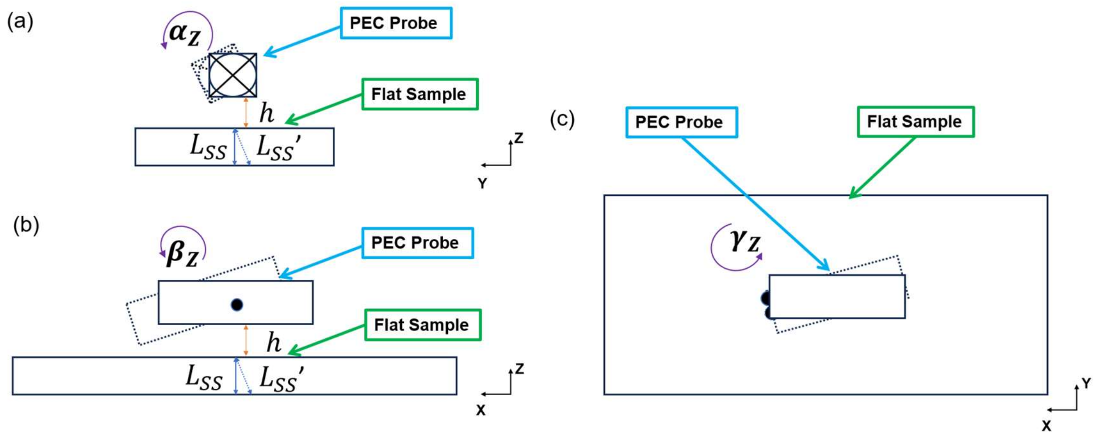

Figure 3-9: PEC sensor surface scanning convention: (a) Front view (b) Side view (c) Top view

The following parameters are utilised to define the thickness experiment measurement figures:

- α_Z Roll angle of the sensor (°)
- β_Z Pitch angle of the sensor (°)
- γ_Z Yaw angle of the sensor (°)
- h Lift off distance of the sensor (mm)
- L_{SS} Sensor to Surface Distance (SSD) (mm)
- L_{SS}' Actual measured Sensor to Surface distance (mm)

In the case of the 6.0 mm-thickness carbon steel sample, the actual thickness value could be then obtained to be 6.004, 6.015, 6.007, 6.018, 6.029 mm in terms of the angles change of 0° and 2°, 0° and 4°, 2° and 2°, 2° and 4°, 4° and 4° separately on two separate axes. The other actual measured thickness values are shown in Table 3-1

Table 3-1: The nominal and actual measured thickness after two angle changes

Nominal (mm)	Angle Change 0 and ±2 (°)	Angle Change 0 and ±4 (°)	Angle Change ±2 and ±2 (°)	Angle Change ±2 and ±4 (°)	Angle Change ±4 and ±4 (°)
6	6.004	6.015	6.007	6.018	6.029
10	10.006	10.024	10.012	10.031	10.049
20	20.012	20.049	20.024	20.061	20.098

In this case, the relative error η could be obtained by using the formula:

$$\eta = \left|\frac{y_a - y_E}{y_E}\right| \times 100\% \tag{3.1}$$

Where y_a is the actual observed thickness value, while y_E is the expected thickness value.

Consequently, for each position, five measurements were gathered corresponding to the count of individual points identified during the acquisition. To produce one error value for each thickness measurement and each tilt angle, the mean value can be calculated using:

$$\bar{y} = \frac{1}{N}\sum_{i=1}^{N} y_i \tag{3.2}$$

Where N is the number of collected data points of each thickness measurement for each angle, and $y(i)$ is the i-th measurement thickness.

At the same time, the Root Mean Square Error (RMSE) was calculated compared to the actual material surface, given by:

$$RMSE = \sqrt{\frac{\sum_{i=1}^{N} \left\| y_i - \hat{y}_i \right\|^2}{N}} \tag{3.3}$$

and the RMSE standard deviation with

$$\sigma_{RMSE} = \sqrt{\frac{1}{N} \sum_{i=1}^{N} (RMSE_i - \overline{RMSE_i})^2} \tag{3.4}$$

Where $\hat{y}_i$ is the corresponding prediction measurement thickness of y_i, and $RMSE_i$ is the i-th RMSE value.

Then the relative RMSE value could be calculated as

$$RMSE_r = \text{RMSE} - RMSE_{(0,0)} \tag{3.5}$$

Where $RMSE_{(0,0)}$ represents the RMSE when both angle of the axis is zero degree.

These relative RMSE values were then employed to create surface plots, which is able to facilitate the identification of patterns within the data. Figure 3-10 depicts the 125 unique orientation angles as the sensor pivots around the yaw (A), pitch (B), and roll (C) axes of the end effector of the 6 DOFPOS (Degrees of Freedom Positioning System). This representation emphasizes consistent raster scanning within the angular space.

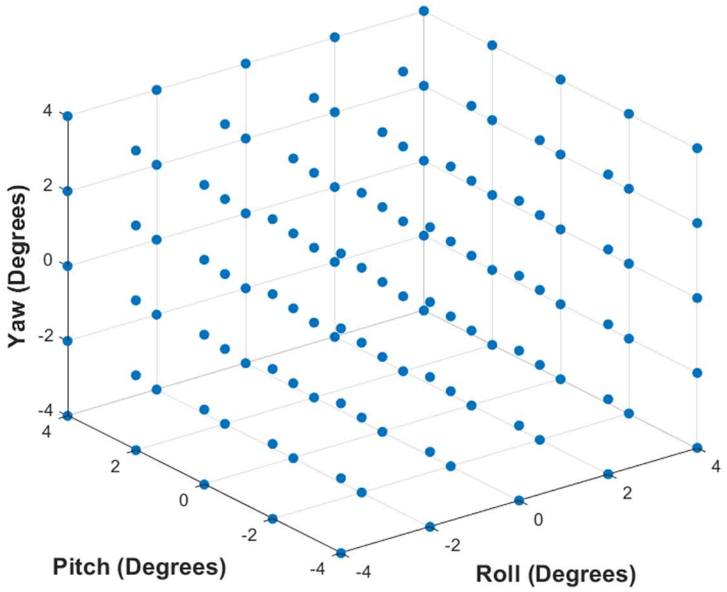

Figure 3-10: Complete scanning pose locations illustration.

Considering the three separate orientation factors, the error data can be analysed from three angles: AB, AC, and BC. Due to the structure of the orientation sweep, for a constant AB/AC/BC pair, there are several thickness data points. In each position, there are five unique RMSE measurements related to the five distinct values of the final third orientation angle.

To understand the trend in the error data, the average value could be computed from the column of five RMSE for each pair of angles on the independent axes, as shown in Table 3-2, Table 3-3. Table 3-4, Table 3-5 and Table 3-6. The calculation of this mean enables a surface of relative RMSE error to be plotted along both axes. Such a plot is shown below (Figure 3-11) for AB orientation for a nominal thickness of 6.0 mm.

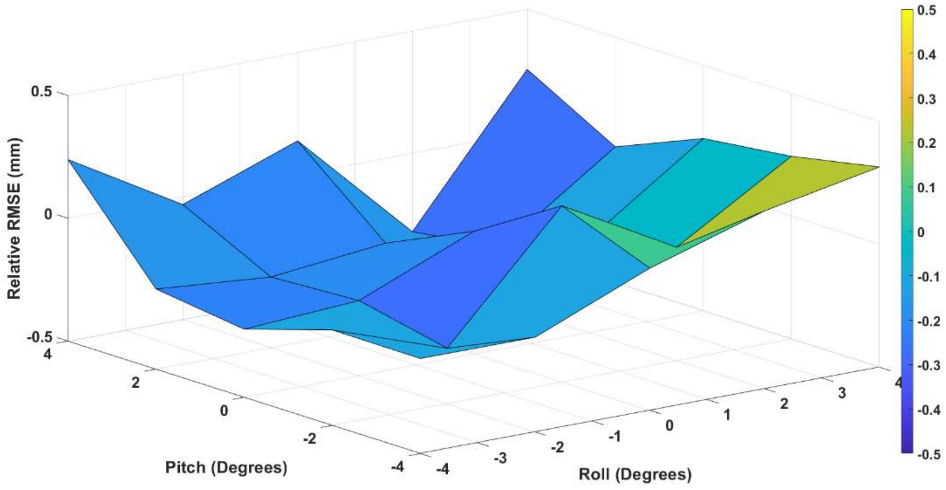

Figure 3-11: Two angle orientation error surface plot.

The standard deviation could then be obtained, taking into account both direction axes, throughout the surface plot, as well as the mean error.

3.4 Experimental Results and Performance Validation

The study comprised 125 individual distance scans for each material tested, with each scan containing between 10,700 and 10,860 distinct data points, including amplitude and time values. Although the dataset size itself is manageable, the manual collection process was time-consuming. Due to limited access to the instrumentation, automating the process was not feasible within the available timeframe. The complexity and density of the data further necessitated the use of visualization techniques to enable effective analysis and interpretation.

3.4.1 Angular Factor Validation

Using the Eq. 3.3, the mean value and relative measurement error across the whole measurement window can be calculated.

Table 3-2: Mean and relative error of measurement data after 0° and 2° change, with two different axes respectively

Nominal Thickness (mm)	Angle-Corrected Ground Truth (mm)	Mean (mm)	Relative Error η
6	6.004	7.395	23.168%
10	10.006	10.430	4.237%
20	20.012	20.065	0.265%

Table 3-3: Mean and relative error of measurement data after 0° and 4° change, with two different axes respectively

Nominal Thickness (mm)	Angle-Corrected Ground Truth (mm)	Mean (mm)	Relative Error η
6	6.015	7.415	23.027%
10	10.024	10.461	4.360%
20	20.049	20.105	0.279%

Table 3-4: Mean and relative error of measurement data after 2° and 2° change, with two different axes respectively

Nominal Thickness (mm)	Angle-Corrected Ground Truth (mm)	Mean (mm)	Relative Error η
6	6.007	7.390	23.023%
10	10.012	10.435	4.225%
20	20.024	20.100	0.380%

Table 3-5: Mean and relative error of measurement data after 2° and 4° change, with two different axes respectively

Nominal Thickness (mm)	Angle-Corrected Ground Truth (mm)	Mean (mm)	Relative Error η
6	6.018	7.437	23.579%
10	10.031	10.455	4.23%
20	20.061	20.1625	0.51%

Table 3-6: Mean and relative error of measurement data after 4° and 4° change, with two different axes respectively

Nominal Thickness (mm)	Angle-Corrected Ground Truth (mm)	Mean (mm)	Relative Error η
6	6.029	7.521	24.747%
10	10.049	10.498	4.468%
20	20.098	20.242	0.716%

The performance of the probe when scanning the steel samples, as depicted in Figure A-1 to Figure A-3, reveals that the lowest mean error for RMSE was detected at the thickest sample, specifically 20 mm, which is shown in APPENDIX A. In this case, the minimal change in error could be found when any of the orientation angles through the chosen range are varied. Furthermore, an obvious nonlinear trend emerged in all three orientations. However, this trend was weakened at increased nominal thickness measurement. It could be noted that such a nonlinear effect is not obvious for yaw (C) orientation.

Moreover, at the selected lift-off distance, the nominal thickness recorded by the probe was persistently higher than the real sample thickness, resulting in a positive distance error in all cases, as emphasized in Figure A-1 to Figure A-3.

When the nominal sample thickness was decreased to 10.0 mm, there was a corresponding slightly increase in the relative RMSE in the roll (A) and pitch (B) orientations. For the other two orientations, the change of error almost remains constant.

In terms of the 6.0 mm nominal steel sample, a sharp increase of relative RMSE occurred. Nevertheless, there was a minimal variation in error when any of the orientation angles were altered within the selected range, at this proximity.

3.4.2 Angular Factor Discussion

The experimental results displayed in Appendix A.1, Appendix A.2 and Appendix A.3 demonstrate that the performance of the PEC probe on steel samples varies with sample thickness and orientation. Appendix A.4 shows the representative raw signals, captured with different thickness, and orientation. The PEC sensor was able to measure thickness even when the probe was not perfectly aligned.

For the 6.0 mm thickness samples, the probe demonstrates high accuracy and stability across all fixed orientations. As shown in Table A-1, the highest recorded error stood at 0.451 mm. The RMSE remains low and consistent whether the roll, yaw, or pitch angle is fixed. This consistency suggests that the probe’s measurements are reliable and less sensitive to changes in orientation for thinner samples. The minimal error variation across different angles indicates that the probe's design and calibration are well-suited for thinner steel samples, ensuring precise measurements.

When the sample thickness increases to 10.0 mm, there is a noticeable, albeit slight, increase in RMSE values and variability. With the roll angle fixed, the probe still maintains relatively low errors, although there is a slight increase compared to the 6.0 mm samples. This trend continues with fixed yaw and pitch orientations, where the RMSE remains generally low but exhibits more variability. The increased thickness introduces more complexity in the measurement process, yet the probe's performance remains within an acceptable range. This suggests that the probe is capable of handling medium-thickness samples effectively, but users should be aware of the slight increase in measurement error.

For the 20.0 mm thickness samples, the RMSE values increase significantly, indicating greater measurement challenges. When the roll angle is fixed, the RMSE shows larger variability across different yaw and pitch angles, suggesting that the probe's accuracy is more affected by thicker samples. As illustrated Table A-2, an error peak of 1.408 mm occurred when the probe was misaligned by 4◦ along both the x-axis and y-axis. Similar trends are observed for fixed yaw and pitch orientations, where the RMSE values are higher, and the error variability increases. This indicates that the probe's performance is less stable with thicker samples. Misalignments can increase the signal attenuation, leading to more pronounced discrepancies in measurements of thicker materials, as opposed to thinner ones where the signal does not have to travel as deeply, maintaining more of its integrity. In addition, in thicker materials, minor angular misalignments at the surface can translate into substantial spatial errors at greater depth due to geometric effects, impacting the accuracy of the readings.

Across all thicknesses, the fixed roll and yaw orientations generally result in lower RMSE values compared to the fixed pitch orientation. This trend is particularly evident for the thicker samples, where fixing the pitch angle leads to higher errors and greater variability. This indicates that the probe's design may be more optimized for stability in roll and yaw orientations, whereas pitch changes introduce more complexity into the measurement process. In the terms of autonomous inspections, robots should take this orientation sensitivity into account when planning measurements, especially for thicker samples. Additional calibration or compensation techniques might be necessary to ensure accurate measurements.

Overall, the probe performs best with thinner steel samples, demonstrating high accuracy and stability across different orientations. As the thickness increases, the measurement accuracy decreases, with significant challenges observed for 20.0 mm samples. However, the errors increased by less than 1.5 mm, and therefore, the sensor was still working well, even with the imperfect alignments. The orientation of the probe plays a crucial role in the measurement accuracy, with fixed roll and yaw orientations generally providing better stability compared to fixed pitch. These findings highlight the importance of considering both sample thickness and probe orientation to achieve reliable and accurate measurements in practical inspections.

3.5 Conclusions

An extensive study was conducted on the performance and system characterization of the MAXWELL PEC P1 probe when used to scan various thicknesses of low carbon steels. The research particularly focused on how changes in orientation angles affect thickness measurements, simulating conditions like those encountered when the probe is mounted on a hybrid-crawler UAV.

Experimental results highlight the PEC probe's varied performance on steel samples, influenced by thickness and alignment. The 20.0 mm thick samples exhibited slightly greater susceptibility to orientation effects, yet errors remained below 1.5 mm. Conversely, alignment had a limited impact on thinner samples (6.0 mm), with the maximum error reaching only 0.451 mm. The thicker samples are more sensitive to alignment due to deeper probe penetration, causing signal attenuation and spatial errors. Consistently, the probe overestimates thickness. These insights inform strategies to optimize probe deployment and improve accuracy in NDT.

Importantly, these findings are critical for addressing challenges associated with sensor sensitivity and measurement accuracy, particularly in the context of UAVs. Ultimately, this research serves as a foundation for future advancements in NDT techniques, offering a roadmap for using PEC probes in UAV deployments. As industries increasingly rely on automation and robotics for inspection and monitoring tasks, the insights gathered from this study pave the way for enhanced efficiency, precision, and reliability in industrial operations.

Despite promising results, several limitations exist. The controlled laboratory setting with an industrial robotic manipulator does not fully replicate real-world UAV environments. The test samples were uniform, flat carbon steel plates, not reflecting real-world variability in material properties, surface roughness, and geometry.

Future research will focus on automating the inspection process to increase efficiency and allow for the capture of more data points, which would make the data analysis more robust and effective. Additionally, collaborations with industrial partners will be pursued to align the developed system with real-world applications by mounting a commercial PEC inspection kit onto an aerial platform. To improve the calibration process, the more precise XYZ 4-point calibration method will be adopted, which will ensure greater accuracy in tool alignment. Moreover, future experiments will use finer angular steps to gather more detailed performance data, particularly for more complex geometries and non-planar structures common in industrial settings. Finally, field tests using UAVs equipped with PEC sensors in real-world environments will be conducted, exploring non-uniform components such as drawn pipes, which vary in material composition and thickness. This will be crucial for enhancing the system's capability in handling real-world conditions for modern industrial applications.

Chapter 4 Design, Optimisation and Validation of PEC Sensor System for Autonomous Non-destructive Testing

4.1 Introduction

As stated in Chapter 1 Section 1.2, one of the key challenges in automated aerial deployed PEC inspection lies in optimizing the PEC system to function reliably in positionally varying and often harsh operational environments. The primary motivation behind this chapter and body of work is to address the limitations of traditional PEC systems, which are too bulky and cumbersome to deploy from aerial platforms. This chapter focuses on optimizing and verifying the design and performance of PEC, ensuring it is compact and efficient for deployment on mobile platforms, particularly UAVs.

The chapter begins with exploring the analytical analysis of the relationship between specimen under inspection thickness and PEC decay rate characteristics, which is the primary method for thickness measurement used in Section 4.3 and later in Chapter 5. It then provides a detailed discussion on the design of a PEC probe, for aerial deployment, using Finite Element Analysis (FEA), including an examination of how dimensional parameters and lift-off height affect the received signal. The subsequent sections cover the overall design and manufacture of a PEC system, including the probe, excitation and receiver circuits, and the DAQ system, explaining how each component was engineered to enhance the system's accuracy and efficiency. Finally, a comparison of the FEA analysis against the experimental results of the system is included, and the elements affecting the results are discussed.

4.2 Methodology

The design process focuses on limitations such as bulkiness, high power consumption, and challenges associated with integration into mobile platforms. A dual-coil configuration was chosen for the sensor to enhance its sensitivity while reducing physical size and weight, ensuring compatibility with UAV-based inspection systems.

Finite Element Analysis (FEA) was conducted using COMSOL Multiphysics to model the electromagnetic response of the PEC sensor in various scenarios, including different carbon steel thicknesses, lift-off distances and coil spacings. The simulations allowed for the investigation of the ability to detect different thicknesses, i.e. decay rate of the induced voltage. These computational results guided the refinement of sensor geometry parameters, ensuring a robust design capable of accurate thickness measurements under real-world conditions.

Following the design phase, a prototype of the PEC sensor was fabricated. The bobbin was created using Stereolithography (SLA), a high-precision 3D printing technique. The sensor coils were constructed using high-conductivity copper wire, and the excitation and detection circuitry were implemented on a printed circuit board (PCB).. The entire system was designed to meet stringent weight and size constraints, facilitating seamless integration with UAVs and ensuring the sensor's durability in field operations.

The sensor system underwent extensive experimental validation to assess its performance. The experimental results were compared with the FEA simulations to validate the sensor's design and confirm its suitability for real-world application.

By following this systematic methodology, the PEC sensor system was successfully designed, optimised and validated for deployment in UAV-based NDT applications. The combination of computational modelling, fabrication and experimental verification ensures that the system can provide reliable and accurate assessments of carbon steel conditions, particularly for critical infrastructure such as pipelines.

4.3 Analytical Derivation of the Relationship between Thickness and Decay Rate Characteristics

A detector coil-based PEC sensor placed above a conducting test piece, when not affected by external sources of noise, can be modelled in circuit theory as a setup composed of infinitely many mutually coupled coils [16]. Figure 4-1(a) shows how [16] models a circular PEC sensor placed above a conducting ferromagnetic plate as a set of mutually coupled coils.

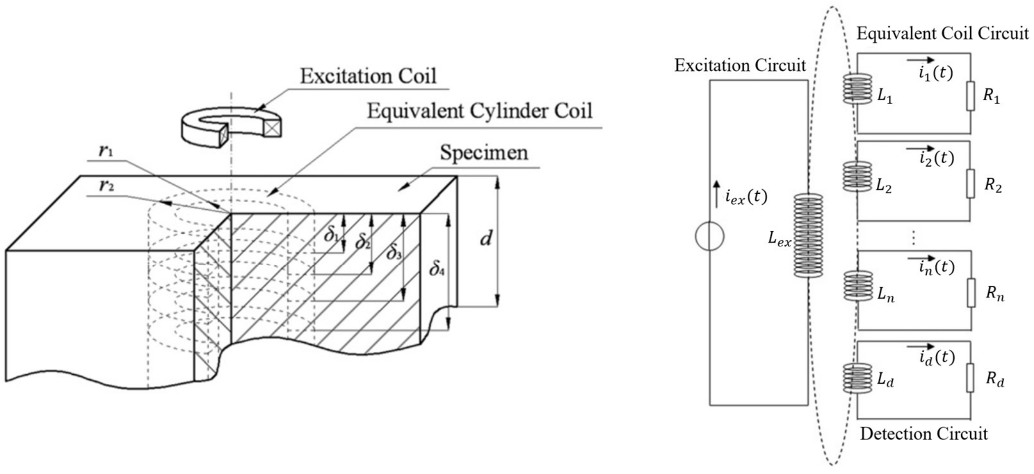

(a) (b)

Figure 4-1: Mutually coupled coil architecture for PEC sensor modelling: (a) Mutually coupled coil model; (b) equivalent circuit model for pulsed eddy current testing system. (adapted from [16]).

As shown in [16], by applying Kirchhoff's laws to every current carrying coil in the model considering coil resistances (denoted by R terms), self inductances (denoted by L terms) and mutual inductances (denoted by M terms), the set of simultaneously solvable differential equations shown in Figure 4-1(b) can be derived for a pulsed current excitation $Au(t)$, where A denotes amplitude and $u(t)$ denotes the Heaviside step function.

$$
\begin{cases}
M_{1ex}\frac{di_{ex}(t)}{dt} - L_1\frac{di_1(t)}{dt} + M_{12}\frac{di_2(t)}{dt} + M_{13}\frac{di_3(t)}{dt} + \cdots + M_{1n}\frac{di_n(t)}{dt} + M_{1d}\frac{di_d(t)}{dt} - R_1 i_1(t) = 0 \\
M_{2ex}\frac{di_{ex}(t)}{dt} - M_{21}\frac{di_1(t)}{dt} - L_2\frac{di_2(t)}{dt} + M_{23}\frac{di_3(t)}{dt} + \cdots + M_{2n}\frac{di_n(t)}{dt} + M_{2d}\frac{di_d(t)}{dt} - R_2 i_2(t) = 0 \\
M_{3ex}\frac{di_{ex}(t)}{dt} - M_{31}\frac{di_1(t)}{dt} - M_{32}\frac{di_2(t)}{dt} - L_3\frac{di_3(t)}{dt} + \cdots + M_{3n}\frac{di_n(t)}{dt} + M_{3d}\frac{di_d(t)}{dt} - R_3 i_3(t) = 0 \\
\vdots \\
M_{(n-1)ex}\frac{di_{ex}(t)}{dt} - M_{(n-1)1}\frac{di_1(t)}{dt} - M_{(n-1)2}\frac{di_2(t)}{dt} - \cdots - L_{n-1}\frac{di_{n-1}(t)}{dt} + M_{(n-1)n}\frac{di_n(t)}{dt} + M_{(n-1)d}\frac{di_d(t)}{dt} - R_{n-1} i_{n-1}(t) = 0 \\
M_{nex}\frac{di_{ex}(t)}{dt} - M_{n1}\frac{di_1(t)}{dt} - M_{n2}\frac{di_2(t)}{dt} - \cdots - M_{n(n-1)}\frac{di_{n-1}(t)}{dt} - L_n\frac{di_n(t)}{dt} + M_{nd}\frac{di_d(t)}{dt} - R_n i_n(t) = 0 \\
M_{dex}\frac{di_{ex}(t)}{dt} - M_{d1}\frac{di_1(t)}{dt} - M_{d2}\frac{di_2(t)}{dt} - \cdots - M_{d(n-1)}\frac{di_{n-1}(t)}{dt} - M_{dn}\frac{di_n(t)}{dt} - L_d\frac{di_d(t)}{dt} - R_d i_d(t) = 0
\end{cases}
\tag{4.1}
$$

Solving the set of equations yields an expression consisting of an infinite summation of exponents and an infinite summation of sinusoidal oscillations for the induced detector coil voltage. Considering the practical circumstance where the signal is conditioned by amplifiers and filters, the oscillations can be ignored and the analytical model in Eq. 4.1 which represents the decaying part of a PEC induced detector coil voltage can be derived [16].

$$\mathrm{V(t)} = \sum_{\mathrm{i}=1}^{\infty} \mathrm{k_i} \exp(-\mathrm{b_i t}) \tag{4.2}$$

Terms k_i and b_i in Eq. 4.2 are constants that encapsulate the properties of the sensor setup and the test piece. The condition $b_i > 0$ holds for all i [16]. Using linear and homogeneous representations of magnetic permeability μ and electrical conductivity σ, the diffusion time constant of eddy currents induced in a ferromagnetic plate of thickness d is defined as $\mu\sigma d^2/\pi^2$ [77]. This represents the largest time constant appearing in an exponential term within the infinite summation of Eq. 4.2, making the corresponding exponential term dominant in the late stage of the signal (just before the eddy currents decay to zero) [30]. In this thesis, the dominant term is isolated and $V(t)$ is rewritten as

$$V(t) = k_1 \exp\left(-\frac{\pi^2 t}{\mu\sigma d^2}\right) + \sum_{i=2}^{\infty} k_i \exp(-b_i t) \tag{4.3}$$

The goal is to derive the time derivative of $V(t)$ to express the decay rate. Before differentiation, $V(t)$ is expressed in its natural logarithmic form in this thesis:

$$\ln[V(t)] = \ln\left[k_1 \exp\left(-\frac{\pi^2 t}{\mu\sigma d^2}\right) + \sum_{i=2}^{\infty} k_i \exp(-b_i t)\right] \tag{4.4}$$

This logarithmic transformation is necessary to establish a direct proportionality between thickness in the form of $\frac{1}{d^2}$ and the decay rate, in addition to the already existing exponential relationship. The later stage of a noise-free PEC signal in the form of $V(t)$ becomes a positive-valued decreasing convex function of time, characterized by a summation of exponential decays as suggested by Eq. 4.4.

Considering the logarithm of this region, $\ln[V(t)]$, it also becomes a decreasing function, typically convex. Although the decrease in $\ln[V(t)]$ is apparent, confirming convexity or concavity is not straightforward. Therefore, the second derivative of $\ln[V(t)]$ should be considered theoretically. Let $V'(t)$ and $V''(t)$ denote the first- and second-time derivatives of $V(t)$, respectively.

$$\frac{d^2 \ln[V(t)]}{dt^2} = \frac{V(t)V''(t) - [V'(t)]^2}{[V(t)]^2} \tag{4.5}$$

According to the principles of convex functions [111], a positive second derivative confirms convexity, while a negative one ensures concavity. Therefore, $V(t)V''(t) > [V'(t)]^2$ is the necessary condition for $\ln[V(t)]$ to be convex over a specified period. The parameters of Eq. 4.5 can be estimated as done in [16] for a given PEC signal, which can then be used to check the condition in Eq. 4.5 to verify convexity. Alternatively, this can be easily identified by studying signals plotted against. This behaviour is common to many ferromagnetic and non-ferromagnetic materials, with convexity in the late stages of $\ln[V(t)]$ being typical. However, concavity, though rare, is not impossible. Differentiating Eq. 4.4 yields Eq. 4.5, which is a negative-valued function since $\ln[V(t)]$ is decreasing over time in its decaying part.

$$\frac{d \ln[V(t)]}{dt} = \frac{k_1 \pi^2}{\mu\sigma d^2} \exp\left(-\frac{\pi^2 t}{\mu\sigma d^2}\right) + \sum_{i=2}^{\infty} k_i b_i \exp(-b_i t) \tag{4.6}$$

By grouping exponential terms, the absolute value of the decay rate can be expressed as

$$\left|\frac{d \ln[V(t)]}{dt}\right| = \frac{\pi^2}{\mu\sigma d^2} \left\{ \frac{1 + \sum_{i=2}^{\infty} \frac{k_i}{k_1} \frac{b_i}{\pi^2/(\mu\sigma d^2)} \exp\left[\left(\frac{\pi^2}{\mu\sigma d^2} - b_i\right) t\right]}{1 + \sum_{i=2}^{\infty} \frac{k_i}{k_1} \exp\left[\left(\frac{\pi^2}{\mu\sigma\ ^2} - b_i\right) t\right]} \right\} \tag{4.7}$$

Since $\mu\sigma d^2/\pi^2$ is the largest time constant and $b_i > \pi^2/(\mu\sigma d^2)$ holds for all i, we express the main relationship used for our work, the reciprocal of the absolute value of the decay rate, as

$$\tau(t) = \frac{dt}{d\ln[V(t)]} = \frac{\mu\sigma\ {}^{2}}{\pi^2}\left\{\frac{1+\sum_{i=2}^{\infty}\frac{k_i}{k_1}\frac{b_i}{\pi^2/(\mu\sigma d^2)}\exp\left[\left(\frac{\pi^2}{\mu\sigma\ {}^{2}}-b_i\right)t\right]}{1+\sum_{i=2}^{\infty}\frac{k_i}{k_1}\exp\left[\left(\frac{\pi^2}{\mu\sigma\ {}^{2}}-b_i\right)t\right]}\right\} \tag{4.8}$$

The absolute value of the decay rate thus characterizes the entire decaying part of a PEC-induced detector coil voltage in the absence of noise. Since the relationship in Eq. 4.8 comprises exponential terms, it is differentiable with respect to time. Given the typical convex decrease of the noise-free logarithmic PEC signal, its derivative will be a negative-valued increasing function of time. Therefore, the absolute decay rate will be a positive-valued decreasing function. This causes $\tau(t)$, the reciprocal of the absolute decay rate, to be a positive-valued monotonically increasing function of time. Thus, for a given thickness d of a material with properties μ and σ, the relationship for $\tau(t)$ is a monotonically increasing function of time, reaching a maximum of $\mu\sigma d^2/\pi^2$ as t approaches infinity for materials producing convex $\ln[V(t)]$ signals. If $\ln[V(t)]$ becomes concave by chance for a rare material, $\tau(t)$ will be a monotonically decreasing function, reaching a minimum of $\mu\sigma d^2/\pi^2$. This is a useful attribute of the decay rate for thickness quantification, as demonstrated later in the chapter.

For the purposes of this thesis, the monotonic increase suggests that $\tau(\infty) = \frac{\mu\sigma d^2}{\pi^2}$

(by applying $t \to \infty$ in Eq. 4.8) will be an ideal signal feature for thickness discrimination since it is directly proportional to the square of thickness. Under practical circumstances, $t \to \infty$ cannot be achieved since the signal will enter the noise bounds of the sensor sampling circuitry. Obtaining decay rates at the late stage (just before the signals enter the noise bound) is possible in practical applications. Therefore, the decay rate at late stages can be approximated by $\tau(t) \approx \frac{\mu\sigma\ ^2}{\pi^2}$.

$\tau_{\max}$ is used as the maximum achievable value of $\tau(t)$ of convex $\ln[V(t)]$ before the signals enter the noise margin, as the discriminative signal feature for thickness quantification. If a concave $\ln[V(t)]$ is encountered, the feature will be the same, but should be defined as the minimum achievable value of $\tau(t)$ i.e., $\tau_{\min} \approx \frac{\mu\sigma\ ^2}{\pi^2}$

Since the derived relationship is in the form:

$$\tau_{\max} \approx \frac{\mu\sigma d^2}{\pi^2} \tag{4.9}$$

To achieve a linear relationship, we start by considering the relationship between $\ln \tau_{\max}$ and $\ln d$. By modelling the relationship as:

$$\ln \tau_{\max} \approx 2 \ln d + c \tag{4.10}$$

Where $c \approx \ln\left(\frac{\mu\sigma}{\pi^2}\right)$, we can isolate d by rearranging the equation. Solving for d, we get:

$$\ln d \approx \frac{1}{2}(\ln \tau_{\max} - c) \tag{4.11}$$

To apply the thickness-feature function for condition assessment and estimate thickness, the constant c can be determined from material specimens either by using Superconducting Quantum Interference Device (SQUID) or Physical Property Measurement System (PPMS) devices, or from known thicknesses with calibration signals [64], [84]. However, due to the limited access to SQUID or PPMS devices, this thesis adopts the latter approach.

4.4 Numerically Modelling the PEC Sensor

4.4.1 Fundamental Equations of the Computational Model

Maxwell's equations, which elucidate the interplay between electric and magnetic fields, are foundational to the study of electromagnetic phenomena [112]. These equations encompass Ampere's, Faraday's, and Gauss's laws, and are presented in both differential and integral formats [112], [113].

In its differential form, Ampere's law is expressed as:

$$\nabla \times \vec{H} = \vec{J} + \frac{\partial \vec{D}}{\partial t} \tag{4.12}$$

This equation indicates that a circulating magnetic field $\vec{H}$ is generated by an electric current density $\vec{J}$ and a time-dependent displacement current $\frac{\partial \vec{D}}{\partial t}$. Here, $(\nabla \times)$ signifies the curl operator.

The integral form of Ampere's law is:

$$\oint_c \vec{H} \cdot d\vec{l} = \int_s \left(\vec{J} + \frac{\partial \vec{D}}{\partial t}\right) \cdot d\vec{s} \tag{4.13}$$

For quasi-static conditions where $\sigma \gg \omega\epsilon_0$, with $\omega = 2\pi f$ representing the frequency f, and $\epsilon_0 = 8.854 \times 10^{-12}$ F/m being the permittivity of free space, the displacement current $(\frac{\partial \vec{D}}{\partial t})$ can be neglected. This simplifies Ampere's law to:

$$\nabla \times \vec{H} = \vec{J} \tag{4.14}$$

And

$$\oint_c \vec{H} \cdot d\vec{l} = \int_s \vec{J} \cdot d\vec{s} \tag{4.15}$$

Faraday's law in differential form states:

$$\nabla \times \vec{E} = -\frac{\partial \vec{B}}{\partial t} \tag{4.16}$$

This indicates that a time-varying magnetic flux density $\vec{B}$ induces a circulating electric field intensity $\vec{E}$. The integral form of Faraday's law is:

$$\oint_c \vec{E} \cdot d\vec{l} = -\frac{\partial}{\partial t}\int_s \vec{B} \cdot d\vec{s} \tag{4.17}$$

This shows that a changing magnetic flux through a surface induces an electromotive force (EMF) along the boundary of that surface, opposing the flux change as per Lenz's law [114].

Gauss's law for magnetic fields, in its differential form, is given by:

$$\nabla \cdot \vec{B} = 0 \tag{4.18}$$

This states that the divergence of the magnetic flux density $\vec{B}$ at any point is zero. The integral form of Gauss's law is:

$$\int_s \vec{B} \cdot d\vec{s} = 0 \tag{4.19}$$

This means that the net magnetic flux exiting a surface is zero.

For modelling purposes, additional constitutive relationships are used. The terms μ_0, μ_r, and σ denote the permeability of free space $\mu_0 = 4\pi \times 10^{-7}$ H/m, relative permeability, and electrical conductivity, respectively.

$$\vec{B} = \mu_0\mu_r\vec{H} = \mu\vec{H} \tag{4.20}$$

And

$$\vec{J} = \sigma\vec{E} \tag{4.21}$$

Given these relationships, accurate measurement of electrical and magnetic properties is crucial for numerical modelling. While μ_r is constant for linear materials, it is nonlinear for most ferromagnetic materials, such as critical pipes, where permeability depends on the magnetic field as shown in Eq. 4.22. The B-H curve, relating $|\vec{B}|$ and $|\vec{H}|$, is given by:

$$\mu(|\vec{H}|) = \frac{\partial|\vec{B}|}{\partial|\vec{H}|} \tag{4.22}$$

The magnetic flux density $\vec{B}$ can also be expressed using the magnetic vector potential $\vec{A}$:

$$\vec{B} = \nabla \times \vec{A} \tag{4.23}$$

Substituting Eq. 4.23 into Eq. 4.16, we get:

$$\nabla \times \vec{E} = -\frac{\partial}{\partial t}(\nabla \times \vec{A}) = -\nabla \times \frac{\partial \vec{A}}{\partial t} \tag{4.24}$$

Thus, $\vec{E}$ is expressed as:

$$\vec{E} = -\frac{\partial \vec{A}}{\partial t} - \nabla\Phi \tag{4.25}$$

where Φ is the applied magnetics scalar potential [115], [116]. Multiplying both sides of Eq. 4.25 by σ:

$$\sigma\vec{E} = -\sigma\frac{\partial \vec{A}}{\partial t} - \sigma\nabla\Phi \tag{4.26}$$

Here, $\vec{J_s} = -\sigma\nabla$ is considered as an externally applied source current. Therefore, Eq. 4.26 can be rewritten as:

$$\sigma\vec{E} = -\sigma\frac{\partial \vec{A}}{\partial t} + \vec{J_s} \tag{4.27}$$

The total current density $\vec{J}$ is thus the sum of the induced current density $\overrightarrow{J_{\text{ind}}} = -\sigma\frac{\partial\vec{A}}{\partial t}$ and the source current density $\overrightarrow{J_s}$. Combining Eq. 4.27 and Eq. 4.12 for the quasi-static case results in:

$$\nabla \times \vec{H} = -\sigma\frac{\partial\vec{A}}{\partial t} + \overrightarrow{J_s} \tag{4.28}$$

Substituting $\vec{H}$ from Eq. 4.28 and expressing $\vec{B}$ using $\vec{A}$ from Eq. 4.23, Eq. 4.28 becomes:

$$\nabla \times \vec{B} = \nabla \times \left(\nabla \times \vec{A}\right) = -\mu_0\mu\frac{\partial\vec{A}}{\partial t} + \mu\overrightarrow{J_s} \tag{4.29}$$

Expanding the curl of the curl using $\nabla \times \left(\nabla \times \vec{A}\right) = \nabla\left(\nabla \cdot \vec{A}\right) - \nabla^2\vec{A}$, we get:

$$\nabla\left(\nabla \cdot \vec{A}\right) - \nabla^2\vec{A} = -\mu_0\mu\frac{\partial\vec{A}}{\partial t} + \mu\overrightarrow{J_s} \tag{4.30}$$

By using the Coulomb gauge, $\nabla \cdot \vec{A} = 0$, Eq. 4.30 simplifies to:

$$\nabla^2\vec{A} - \mu_0\sigma\frac{\partial\vec{A}}{\partial t} = -\mu\overrightarrow{J_s} \tag{4.31}$$

Eq. 4.31 represents the magnetic vector potential within the modelled domain and serves as the numerically solvable governing equation for the PEC setup described in this thesis. Subsection 4.3.2 provides further details on the model's development.

4.4.2 Numerical Model Development

Finite Element Analysis (FEA) [117]-[120] is widely utilized to address various multi physics problems, including those involving electromagnetic phenomena such as the eddy current problem [118], [119], [121]. This section focuses on developing the model using the commercially available FEA simulation package, COMSOL Multiphysics® [122]-[124]. Additionally, software packages like ANSYS [125] and

CIVA [126] have been employed in the literature to solve eddy current-related issues. Since this thesis proposes a new configuration and employs the feature extraction method illustrated in Section 4.2 to infer pipe wall thickness using measured signals, the developed numerical model is designed to meet the requirements for solving the forward problem. This involves optimizing probe dimensions, lift-off distances, and accounting for the physical properties of critical pipe materials. Given that the formulated problem does not yield closed-form solutions and is governed by the nonlinear form of Eq. 4.31, numerical solutions are necessary, which is why the versatile technique of FEA is employed in this work.

In traditional coil-based configurations, a single-coil setup comprising one transmitter coil and one receiver coil is commonly used [34], [54], [64], [77], [84], [127], as illustrated in Figure 4-2(a). However, this study proposes a dual-coil configuration, offering potential advantages over the conventional single-coil system.

In this dual-coil configuration, a pair of concentric cylindrical transmitting receiving multi-turn coils were placed side-by-side in the dual-coil configuration. In the dual-coil set-up, as shown in Figure 4-2(b), two transmitter coils were positioned in opposing orientations and were interconnected, with the bottom end of one coil linked to the top end of the other. The arrangement and configuration of the two receive coils mirrored those of the transmit coils. Prior to construction, the interactions between both the single-coil and dual-coil configurations with a steel plate with low carbon content were simulated. This was achieved within a 2D-Axisymmetric framework, as illustrated in Figure 4-3(a) and Figure 4-3(b) for each configuration.

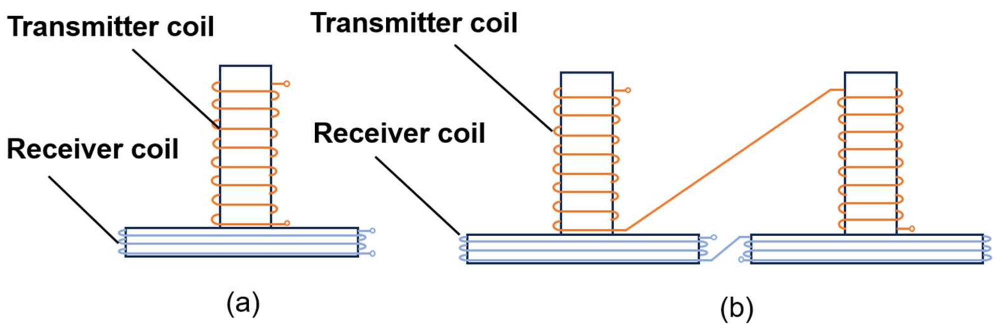

Figure 4-2: The wiring diagram of (a) single-coil configuration, and (b) dual-coil configuration.

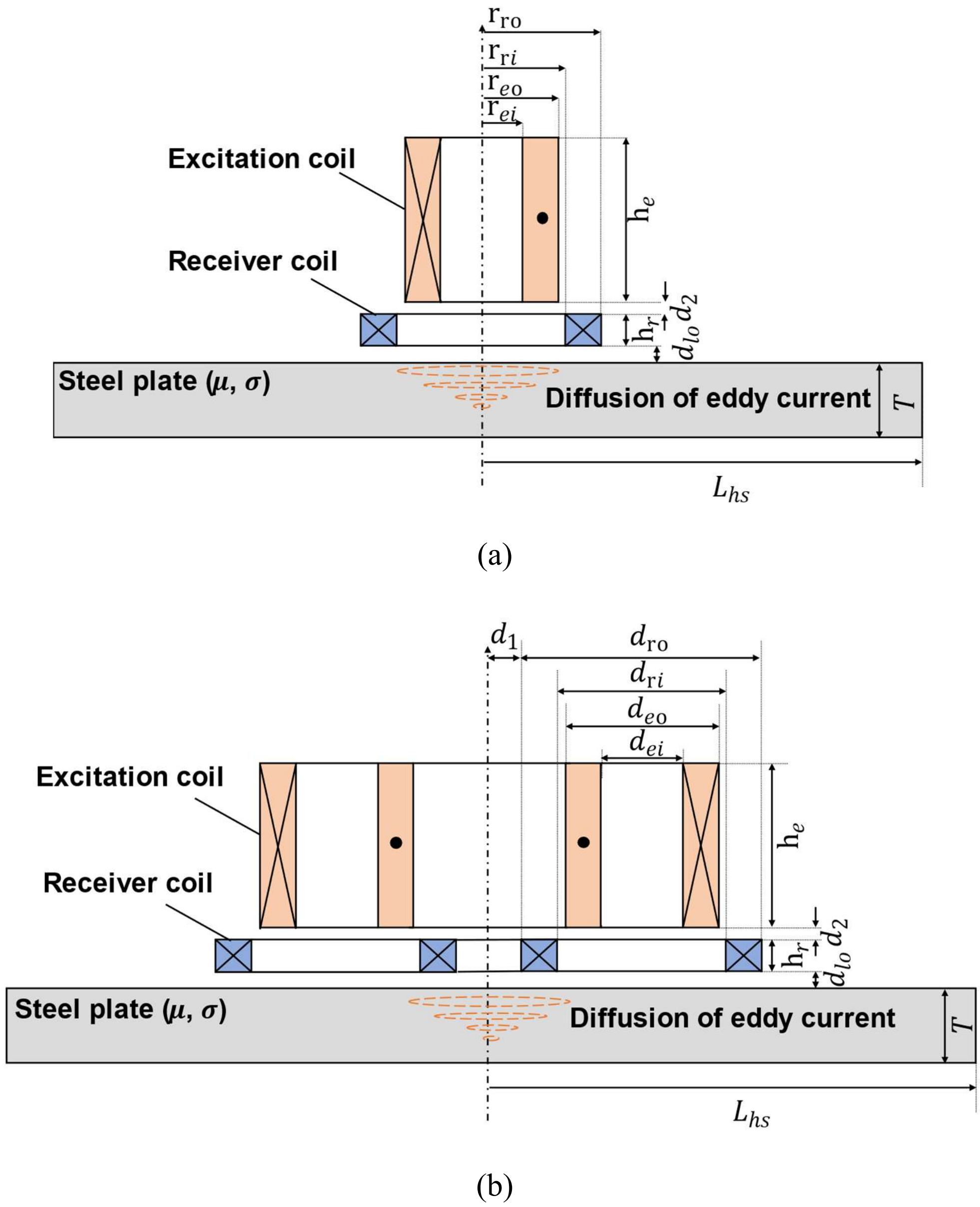

Figure 4-3: A 2D-Axisymmetric PEC simulation model in (a) single-coil configuration, and (b) dual-coil configuration.

In this study, both transmitter and receiver coils were constructed using copper wires with 1 mm diameter / 18 Gauge, and common permeability and electrical conductivity values for copper (μ_e, μ_d, σ_e and σ_d) were employed in simulations. To mitigate potential heat generation from high currents in the excitation pulse, while ensuring sufficient eddy current penetration depth over the sample, the excitation current pulse was set to 5 A.

Given the requirement to mount the final probe configuration on an aerial platform, the excitation coil voltage will be restricted. Since the regulator used in the Section 4.4 has the function to transfer high voltage to constant 12V DC, the sensor excitation voltage essentially takes the shape of a Heaviside step function with 12V amplitude (V_p). Due to the decay rate signal feature used for thickness quantification appearing in the later stages of the signal, capturing the excitation signal's influence on the early stages of the detector signal is not of critical importance for this work. An ideal step function with pulse frequency (f_p) of 1 Hz and duty cycle (D%) of 5% is therefore used to excite the simulated sensor since the rise time of the excitation signal has no significant impact of the predominantly thickness dependent decay rate feature $\beta_{\max} \approx \frac{\mu\sigma d^2}{\pi^2}$. This results in a rest time of 950 ms between pulses, which helps to prevent excessive heat buildup in the excitation coils.

This was also specified for the excitation circuit to energize the coil, necessitating a resistance of 2.4 Ω for the exciter part, resulting in each excitation coil having a resistance of 1.2 Ω. For consistency, the transmitter and receiver coils remained unchanged across both configurations.

For refining and narrowing down the suitable sensor dimensions, the transmitter coil property of r_{eo}, r_{ei}, d_{eo}, d_{ei}, h_e, N_e, d_2 are fixed. In addition, one of the important sets of input variables is the set of test piece properties. The test piece in this case is the flat plate and therefore the required input variables in terms of geometry are sample length $2L_{hs}$ and plate thickness T. In terms of intrinsic material properties, measured electrical conductivity σ and magnetic permeability μ are required. But since carbon steel pipes are ferromagnetic and feature nonlinear magnetic properties, obtaining a constant μ is not possible. As a result, the magnetization curve of low-carbon steel (B-H curve) in COMSOL in the form of $\left|\left|\vec{B}\right|\right| = f\left(\left|\left|\vec{H}\right|\right|\right)$ is applied.

Given the requirement to mount the final probe configuration on an aerial platform, it was crucial to minimize the system's size and weight. Consequently, the diameter of the receiver coil was designed to be as small as feasible. Through a series of iterative experiments and considering various parameters, the suitable dimensions of the receiver (r_{ro}, r_{ri}, d_{ro}, d_{ri}, h_r, N_r) are determined, as listed in . These dimensions were chosen to ensure the system's compactness without compromising its ability to sensitively detect carbon steel sample thicknesses of 2.0 mm, 6.0 mm, 10.0 mm, 15.0 mm and 20.0 mm, with a resolution of 2.0 mm.

The numerical model can thus be expressed as a function f_M which maps the parameters required to the output logarithmic PEC signal V_M as shown in

$$V_M = f_M(r_{ro}, r_{ri}, r_{eo}, r_{ei}, d_{ro}, d_{ri}, d_{eo}, d_{ei}, d_2, d_1, d_{lo}, h_e, h_r, N_e, N_r, R_e, \mu_r,$$
$$\mu_e, \sigma_r, \sigma_e, V_p, f_p, D\%). \tag{4.32}$$

After the numerical model takes B-H curve of the sample, geometry of the test piece, geometric and physical properties of the PEC sensor and excitation signal characteristics as inputs and produces the time varying sensor signal for a given test piece as the output.

4.4.3 Numerical Model Results and Analysis

4.3.3.1 Configurations comparison

Furthermore, to assess the performance between the two configurations, a comparative performance analysis is depicted in Figure 4-4(a) and Figure 4-4(b), illustrating the distribution of the induced eddy currents within the 20.0 mm sample for both setups at the steady state of the transient signal at 2.53 ms. In Figure 4-4(a) the single-coil configuration shows a peak eddy current density of 365 A/m². The eddy currents are primarily concentrated around the area directly beneath the coil, with the intensity diminishing as the distance from the coil increases. This indicates a limited penetration depth and a narrower area of influence, which may restrict the system's sensitivity to variations in sample thickness.

In contrast, Figure 4-4(b) demonstrates the performance of the dual-coil configuration. The peak eddy current density for this setup reaches 573 A/m², significantly higher than that of the single-coil configuration. The eddy current distribution is more extensive and uniform across a broader region of the sample. This enhanced distribution suggests that the dual-coil system can penetrate deeper into the material, providing a more comprehensive assessment of the sample's thickness and internal structure.

For the application of detecting sample thicknesses up to 20 mm at increments of 2 mm, the dual-coil configuration provides enhanced sensitivity due to its higher eddy current density and deeper distribution depth. This makes it particularly suitable for precise measurements in applications requiring consistent detection across the specified thicknesses in the thesis.

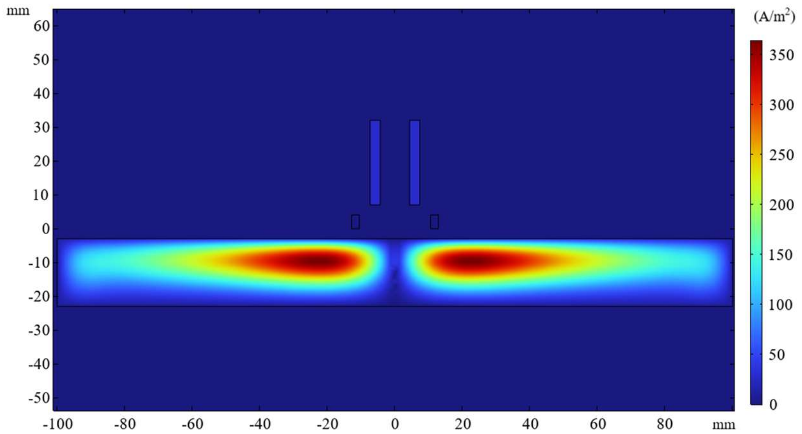

(a)

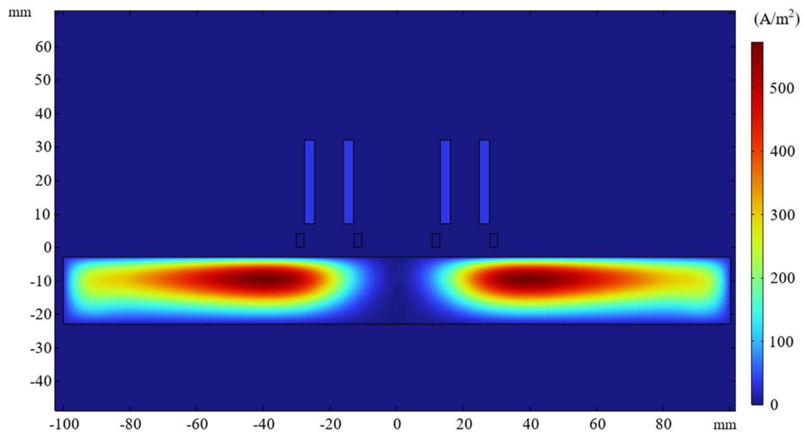

(b)

Figure 4-4: The distributions of eddy current induced in the circumferential direction for (a) single-coil configuration, (b) dual-coil configuration.

Additionally, the log of received signal of both configurations were shown in Figure 4-5. As stated in Section 4.2, the feature extraction method is based on the PEC signal (when expressed as a logarithm) behaving as a straight line at later stages just before entering the noise margin. As shown in Figure 3-4, when examining the later stages of this signal in a logarithmic form, the defined range where $In[V(t)]$ behaves as $t \gg 0$. This is captured by the logarithmic form of the equation:

$$\begin{cases} In[V(t)] \approx -b_1 t + In[k_1] \\ t \gg 0 \end{cases} \tag{4.33}$$

Here, b_1 is the dominant time constant, and $\mathrm{In}[\mathrm{k}_1]$ is its corresponding coefficient. The feature τ, which is central to the sensor's operation, is defined as the reciprocal of the dominant time constant b_1

$$\tau = \frac{1}{\mathrm{b}_1} \tag{4.34}$$

Obviously from Figure 4-5, there is no noise margin since the simulation model is based on the analytical method and no additional noise is added. So, the linear range is chosen from minus infinity to -5 in this case. Using the feature extraction method described in Section 4.2, the maximum and minimum τ values for the 20 mm and 2 mm thicknesses in the normal configuration are 1.553 and 0.593, respectively, resulting in a difference of 0.960. In contrast, the maximum and minimum τ values for the 20.0 mm and 2.0 mm thicknesses in the dual-coil configuration are 16.251 and 1.996, respectively, resulting in a difference of 14.255. This significant increase in the τ difference, by a factor of 13.843, provides much better separation. This improved range enhances the system's robustness against noise and reduces the potential for noise processing errors in the later stages.

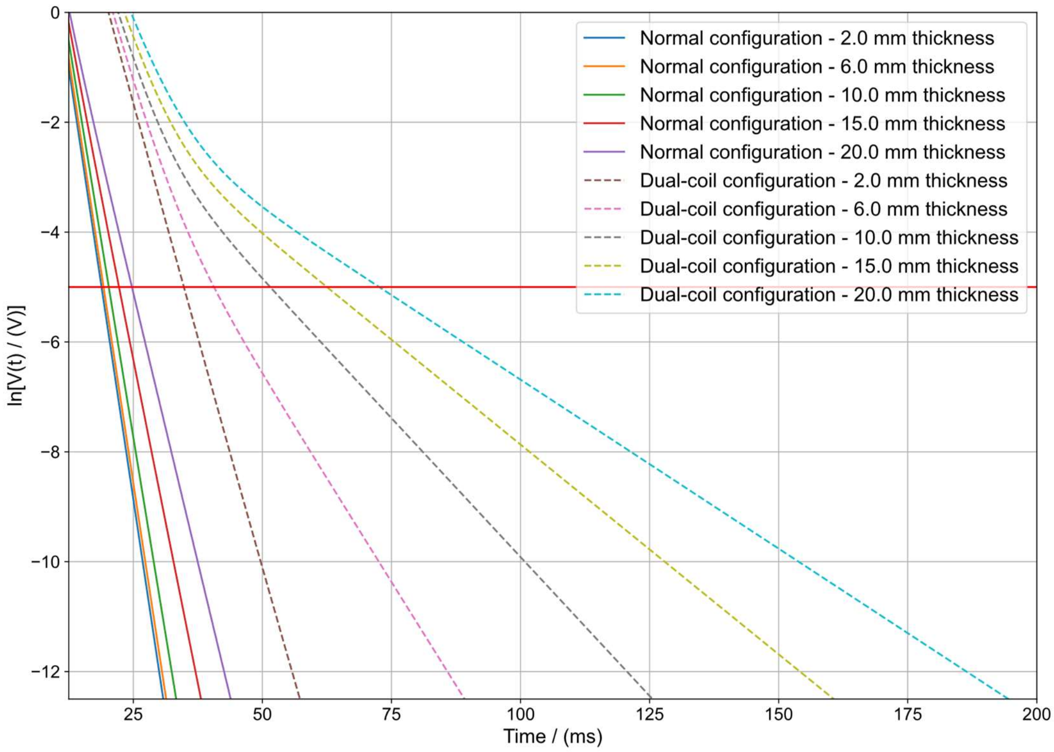

Figure 4-5: Simulation results between the two configurations.

4.3.3.2 Lift-off study

The thickness of tested sample is chosen to be 2.0 mm, 6.0 mm, 10.0 mm, 15.0 mm and 20.0 mm, while the lift-off distance was chosen to be from 1.0 mm to 9.0 mm, with an increment of 2.0 mm, representing different levels of lift-off. The effect of varying lift-off, which can be seen in Figure 4-6, suggests minimal lift-off influence on the time derivative of the signals. In contrast, the amplitude of the signals can be observed to reduce with greater lift-off, owing to the weakened interaction of the induced eddy current.

As previously mentioned, signal gating is carried out by gating the signal in the range of $-\infty \leq \ln\big(V(t)\big) \leq -5$. Following this, τ is extracted by computing the linear fitting of the excerpts of the logarithmic PEC signals and the linear relationship of the features with their corresponding thickness squared, d_{lo}, as shown in Figure 4-7.

It is apparent that the changes in lift-off as much as 9.0 mm has significantly small effect on τ, suggesting the high potential of using this probe design and feature extraction technique for the UAV application.

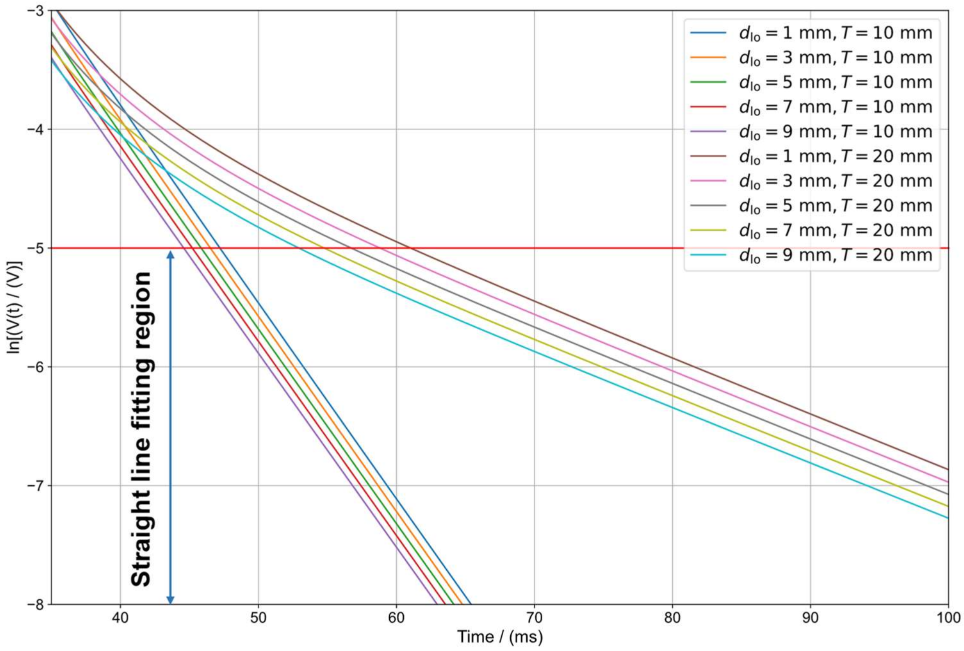

Figure 4-6: Simulated PEC signals with varying lift-off distances (d_{lo}) of sample thicknesses (T).

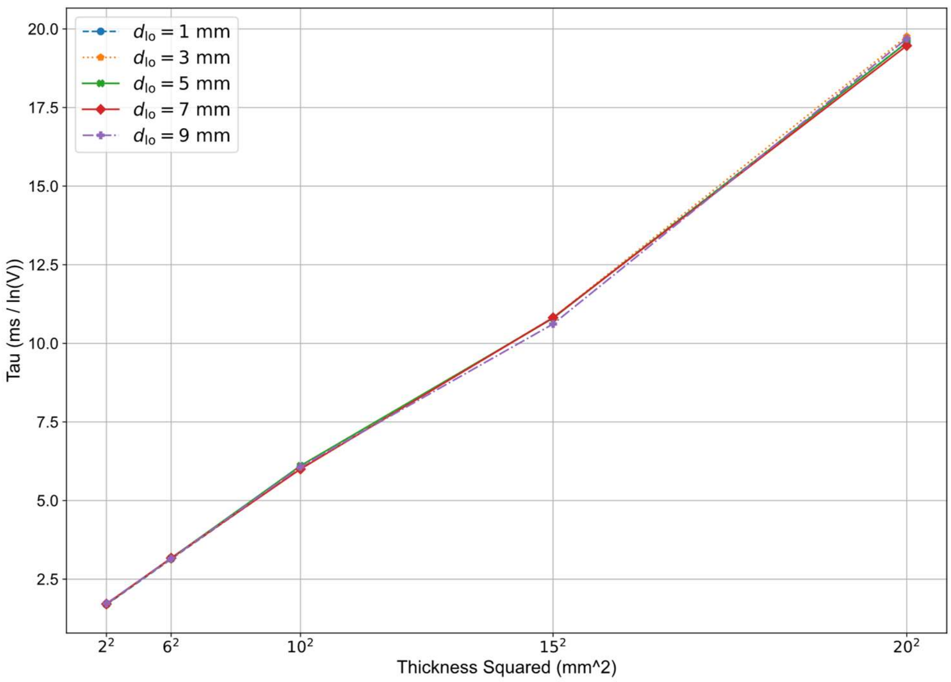

Figure 4-7: Extracted feature values corresponding to different lift-off distances (d_{lo}) and sample thicknesses (T).

4.3.3.3 Effects on horizontal distance of two detector coils

To determine the effects of the horizontal distance between the two detector coils (d_1), this parameter was varied from 1.0 mm to 9.0 mm in 2.0 mm increments, while keeping vertical excitation-detector distances (d_2) constant at 1.0 mm. Following the methodology outlined in Section 4.3.2, the same premise was applied when adjusting d_1. The results from the numerical modelling are shown in Figure 4-8.

As d_1 increased, the signal amplitude decreased, which is evident in the results. This is because a larger d_1 allows less coupling between the excitation and detector coils, leading to reduced PEC signal amplitudes. The responses of d_1 for a sample thickness of 10.0 mm also exhibited greater deviations across the sample thicknesses compared to those for a sample thickness of 20.0 mm.

A quantitative analysis of the τ values, depicted in Figure 4-9, reveals higher variances in PEC signals for larger horizontal distances between the two receiver coils. A smaller d_1 provides a more concentrated magnetic field, resulting in higher sensitivity to changes in sample thickness. This demonstrates that smaller distances are more sensitive to variations in sample thickness parameters. Consequently, it is preferable to design the distance to be as small as possible, while ensuring that the footprint size does not significantly exceed the expected size of the sample's length or width. The ideal parameter was selected to be 1.0 mm. However, due to the tolerances in the 3D printed model and the need to prevent the coils from touching each other when the manufactured probe is mounted onto the mobile platform, a final d_1 of 3.0 mm was chosen for this thesis.

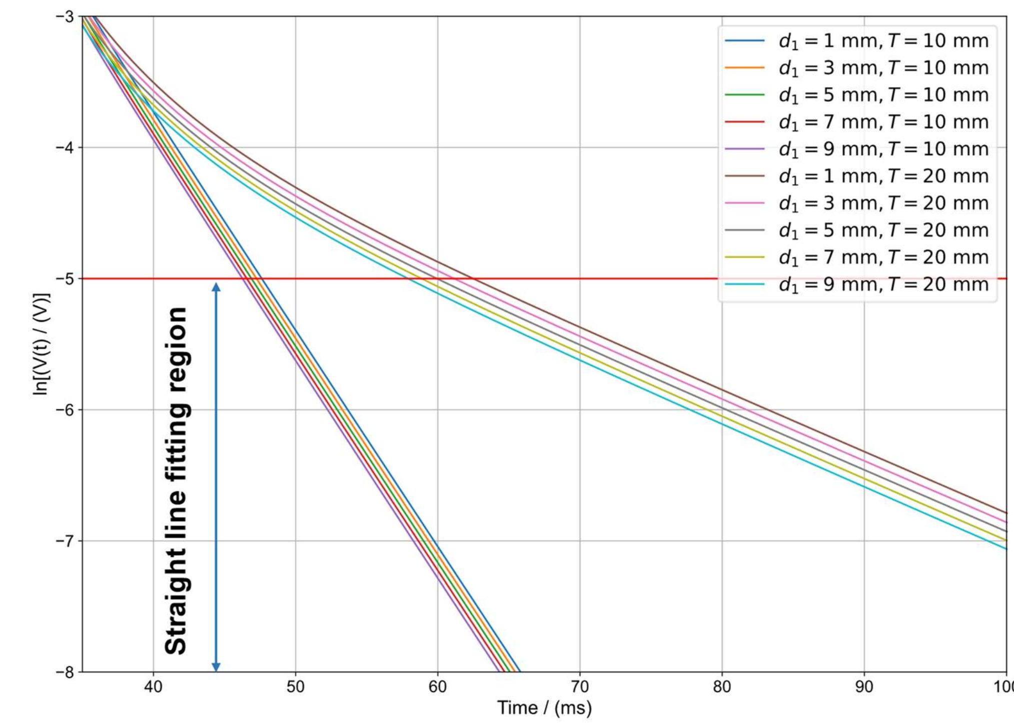

Figure 4-8: Simulated PEC signals with varying horizontal detector coil distances (d_1) and sample thicknesses (T).

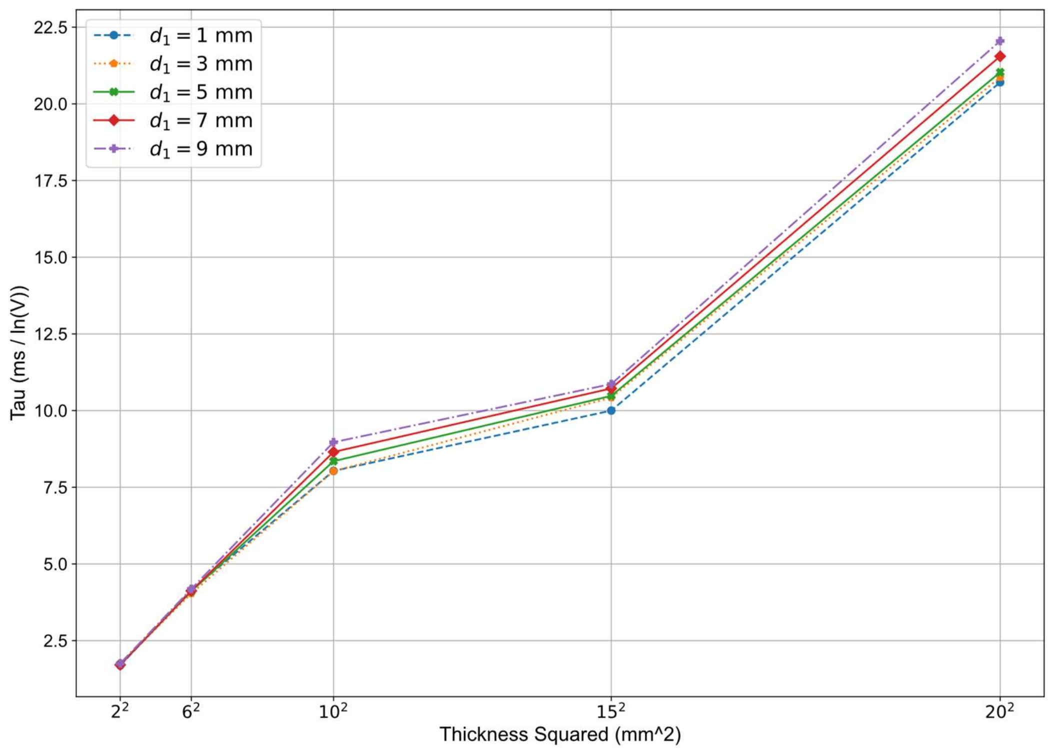

Figure 4-9: Extracted feature values corresponding to different horizontal detector coil distances (d_1) and sample thicknesses (T).

4.3.3.4 Effects on vertical excitation-detector coil distance

The vertical distance between the excitation and detector coils, d_2, was adjusted from 1.0 mm to 9.0 mm in 2.0 mm increments. Responses were recorded for sample thicknesses of 2.0 mm, 6.0 mm, 10.0 mm, 15.0 mm, and 20.0 mm for each d_2 value, while d_1 was kept constant throughout the experiment. The feature extraction method described in Section 4.3.3.1 was applied separately to the five data sets derived from the models. The PEC signals and feature τ for different pipe wall thicknesses are presented in Figure 4-10 and Figure 4-11.

Selective assessments of PEC signals for each d_2 with carbon steel sample thicknesses of 10.0 mm and 20.0 mm are shown in Figure 4-10. Increasing d_2 reduces the coupling between the excitation and sensing coils, resulting in smaller PEC signal amplitudes. However, this parameter does not significantly differentiate the PEC signals, as evidenced by the minimal differences in PEC signals for each d_2 in the 10.0 mm sample thickness compared to the 20.0 mm sample thickness.

The τ values for various d_2 settings across different sample thicknesses are depicted in Figure 4-11. These τ values suggest that d_2 provides a meaningful attribute in relation to sample thickness. While increasing sample thickness leads to higher τ values, varying d_2 does not significantly affect the probe's sensitivity across all thicknesses. The slope of the τ values for each d_2 remains consistent, indicating minimal contributions of d_2 to the sensitivity of the PEC system.

In summary, to minimize the probe dimensions, $d_2 = 1.0$ mm was selected for the probe design, as the vertical excitation-detector coil distance does not impact the probe's sensitivity.

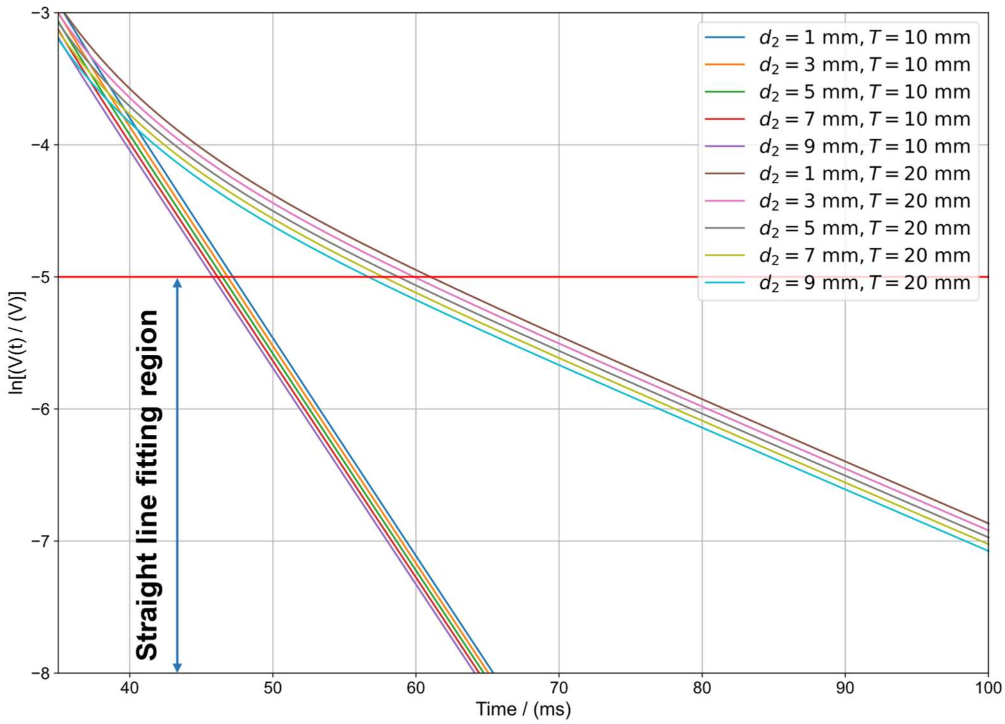

Figure 4-10: Simulated PEC signals with different vertical excitation-detector distances (d_2) and sample thicknesses (T).

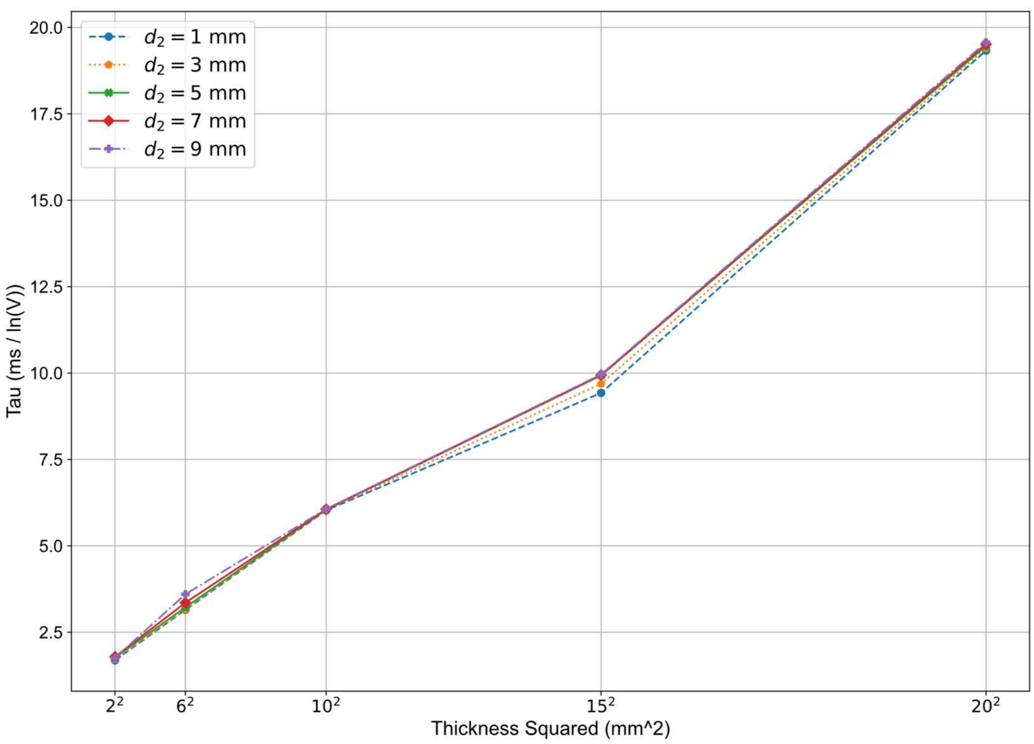

Figure 4-11: Extracted feature values corresponding to different vertical excitation-detector distances (d_2) and sample thicknesses (T).

4.5 Design of System's Framework for A UAV Deployable PEC System

This section outlines the entire PEC system's framework. Illustrated in Figure 4-12, the PEC system is designed for mobility and comprises three primary components: 1) the PEC probe, 2) the onboard PEC electronic system, and 3) the ground station. These elements work in conjunction to generate eddy currents in a test specimen for thickness measurement purposes.

- **Overview of the System**: The PEC system integrates various components to ensure efficient operation and data acquisition. The onboard PEC electronic system is powered by a 6S Lithium Polymer (LiPo) battery, which consists of six cells connected in series, providing a nominal voltage of 22.2V. This voltage is regulated down to 12V using a DC/DC regulator. The regulated power ensures consistent operation as the battery discharges. A Raspberry Pi Zero 2 W with an Analog-to-Digital Converter (ADC) is employed to issue control signals and manage data acquisition. The system includes an excitation board equipped with a Metal-Oxide-Semiconductor Field-Effect Transistor (MOSFET) module to handle high currents and protect the electronics. Additionally, a receiver amplifier board boosts the voltage signal from the receiver coils by 200 times, enhancing signal clarity for processing.
- **PEC Probe:** The PEC probe consists of excitation coils and receiver coils mounted on a 3-D printed probe frame. The excitation coils generate the electromagnetic field required for the PEC system, inducing eddy currents in the test material. The receiver coils detect these eddy currents, which are then processed to assess the material's thickness. The 3-D printed frame ensures

precise alignment and stability of the coils, which is crucial for accurate measurements.

- **Excitation Circuit**: The excitation circuit is responsible for generating the rectangular voltage pulse that drives the excitation coils. The pulse is controlled by the Raspberry Pi, which sends signals to the excitation board. The MOSFET module on the excitation board ensures that the high currents required for generating strong eddy currents do not damage the electronic components. This setup allows for precise control of the excitation signal, which is essential for accurate and repeatable measurements.
- **Receiver Circuit**: The receiver circuit amplifies the signal detected by the receiver coils. The amplified signal is then sent to the ADC on the Raspberry Pi for digitization. The receiver amplifier board ensures that the signal is large enough to be accurately digitized and processed. This amplification is critical for maintaining signal integrity and ensuring that the data collected features sufficient Signal to Noise Ratio. The digitized data is then wirelessly transmitted to the ground station, where it is logged and displayed for further analysis.
- **The Ground Station:** The ground station runs on Ubuntu 18.04 and includes code to receive signal response data via Wi-Fi. It can also remotely log into the Raspberry Pi W 2 to control the excitation circuit. The response signal can be displayed on a customized interface in real time and saved as a .csv file on the ground station for post-processing.

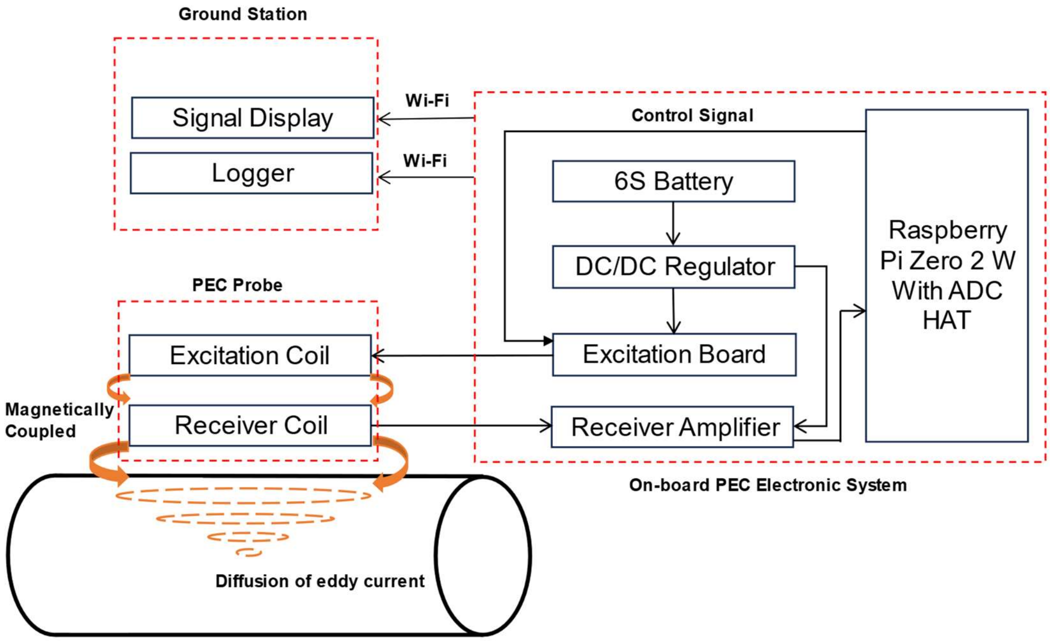

Figure 4-12: The whole PEC system structure.

4.5.1 PEC Probe

Using the parameters outlined in

and the other probe's parameter chosen from Section 4.3.3, the PEC coil and probe were fabricated to meet the stringent requirements of mobile NDT. The fabrication process began with designing the bobbin in Autodesk Inventor 2022, a Computer-Aided Design (CAD) software known for its accuracy and comprehensive modelling capabilities, shown in Figure 4-13. The design was based on parameters derived from the simulation model, focusing on ensuring the bobbin's structural integrity and functional efficiency. Following the design phase, the bobbin was created using Stereolithography (SL), a high-precision 3D printing technique. Stereolithography employs thermoset resins that are cured by ultraviolet light to form a solid structure [128], as illustrated in Figure 4-14.

The use of thermoset resins was a deliberate choice due to their excellent mechanical properties and thermal stability. These resins can withstand temperatures up to 268 °C [128], ensuring that the bobbin remains durable and stable even under extreme operating conditions. This high-temperature resistance is particularly important in PEC applications where the probe may be subjected to closed space environment and heat generated into the excitation coil due to the high current during testing.

The probe’s design also took into consideration the need for robust performance and ease of integration with the overall PEC system. The 3D printed holder provides a stable and secure housing for the coils, ensuring that they remain properly aligned during operation. This alignment is crucial for maintaining the accuracy and reliability of the measurements. Moreover, the compact and lightweight design of the probe makes it suitable for integration with mobile platforms, such as UAVs, enabling remote and precise inspections of complex structures.

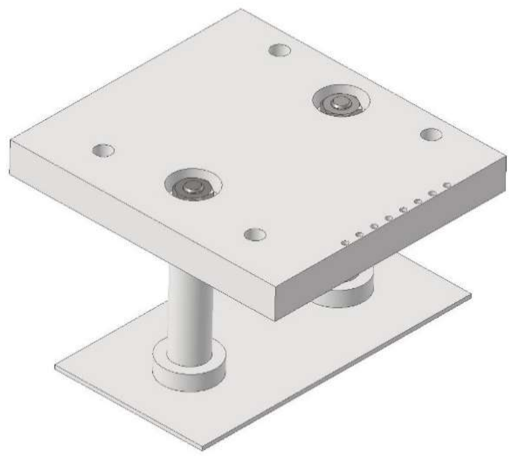

Figure 4-13: The CAD model for PEC probe frame.

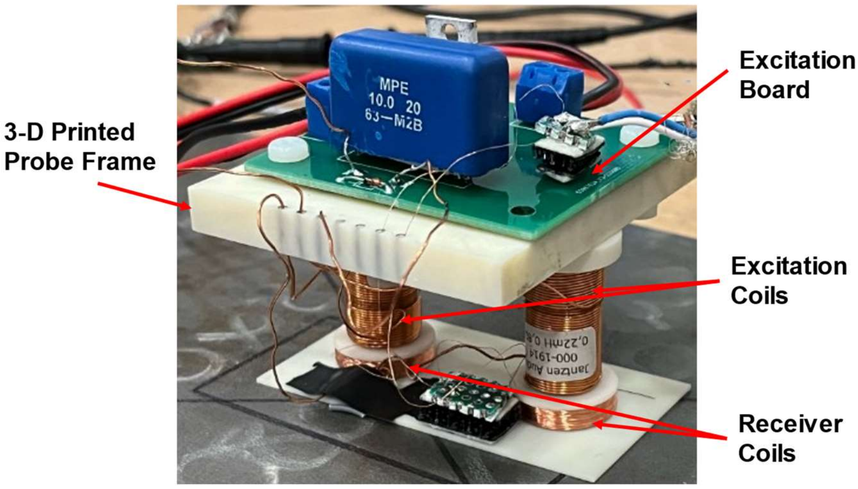

Figure 4-14: The assembled PEC sensor.

4.5.2 Signal Excitation Circuit

As stated in Section 4.3.2, for the signal excitation part of the PEC system, a pulse with a 1 s period and 5% duty ratio was chosen. The signal was sampled at a rate of 25 μs per data point, ensuring enough data to be acquired for the accurate data acquisition for the post-processing. The excitation circuit is composed of a MOSFET, a MOSFET driver, the control signal, and a 12V DC power supply. The DAQ device provides the control signal to the circuit. The 12V DC power is supplied by the 6-Cell battery, which goes through a 12V DC/DC regulator. The system diagram is depicted in the Figure 4-15.

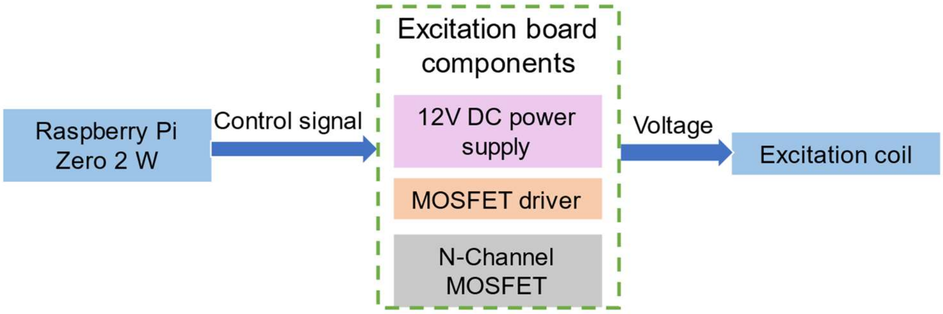

Figure 4-15: Block diagram of the excitation circuit for PEC signal generation.

A more detailed circuit diagram for building the system is shown in Figure 4-16. The IXDN614PI was chosen for the MOSFET driver due to its high current capability and fast switching speed, which are essential for driving the PEC excitation coil circuit. It can ensure rapid switching of the MOSFET and minimizing switching losses and heat generation. Its robust performance in driving large capacitive loads makes it suitable for high-speed PEC applications, ensuring efficient MOSFET operation and minimizing the effects on the rising and falling edges of the PEC signal.

The IRF3709Z is selected for the MOSFET due to its low on-resistance and high current handling capacity, crucial for the PEC excitation coil circuit. This MOSFET can handle continuous currents up to 62 A and has an on-resistance of just 0.0095 ohms, which reduces conduction losses and improves overall efficiency. Its ability to switch rapidly complements the IXDN614PI driver, ensuring that the excitation circuit operates effectively with further minimal power loss and heat dissipation. For the PEC system, the excitation current pulse was set to 5 A, requiring components that can handle significant current loads efficiently.

The combination of the MOSFET driver and the MOSFET ensures a reliable and fast switching signal excitation circuit, suitable for delivering the precise and powerful current pulses necessary for effective PEC measurements.

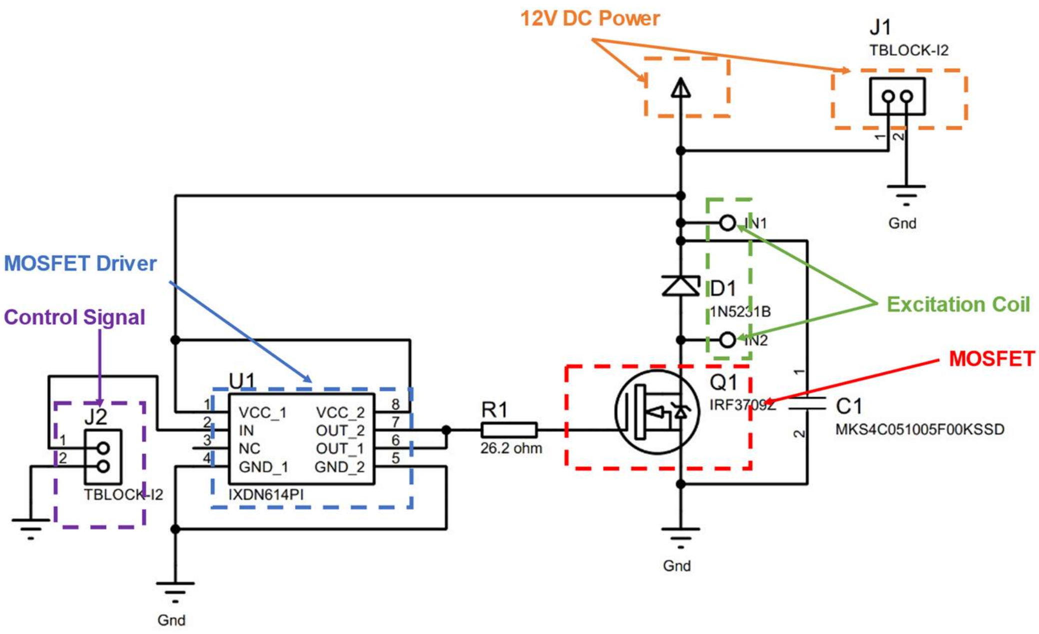

Figure 4-16: Circuit diagram of the excitation circuit for PEC signal generation.

4.5.3 Receiver Circuit

When considering the receiver circuit for capturing the PEC waveforms, the design begins with the signal from the detector coil, which typically falls within the millivolt range. This weak signal is first processed by the receiver circuit shown in Figure 4-17 and Figure 4-18. The signal undergoes initial amplification through the operational amplifiers (OP27GSZ), which are configured as differential amplifiers. These amplifiers are responsible for amplifying the small differential voltage picked up by the receiver coil while rejecting any common-mode noise that may be present. The gain provided by these differential amplifiers is set by adjustable resistors R6 and R7.

Next, the signal is fed into an instrumentation amplifier (U4, INA125U), which is chosen for its high precision and ability to provide a stable gain. The instrumentation amplifier further amplifies the differential signal from the operational amplifiers. This stage of amplification ensures that even the small variations in the signal are accurately captured, enhancing the overall sensitivity and accuracy of the PEC system. The combined overall amplification stages result in a total gain of 200, which boosts the millivolt-range signal to a level suitable for sampling.

The DAQ system, which includes a 12-bit ADC sampling at 40 kHz, interfaces with a Raspberry Pi Zero W 2. This setup ensures that the amplified PEC waveforms are accurately digitized for further analysis. The digitized data is then wirelessly transmitted to the ground station for recording and analysis, enabling real-time monitoring and evaluation of the PEC signals.

This detailed receiver circuit design ensures that the mobile PEC system can accurately capture and process the waveforms, providing reliable data for NDT applications. The use of high-precision components and careful design considerations in the amplification stages are critical for maintaining signal integrity and achieving high-quality measurements.

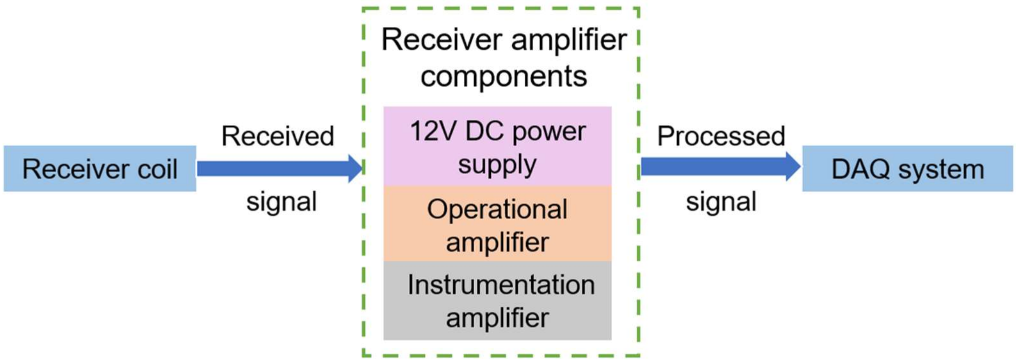

Figure 4-17: Block diagram of the receiver circuit for PEC signal acquisition.

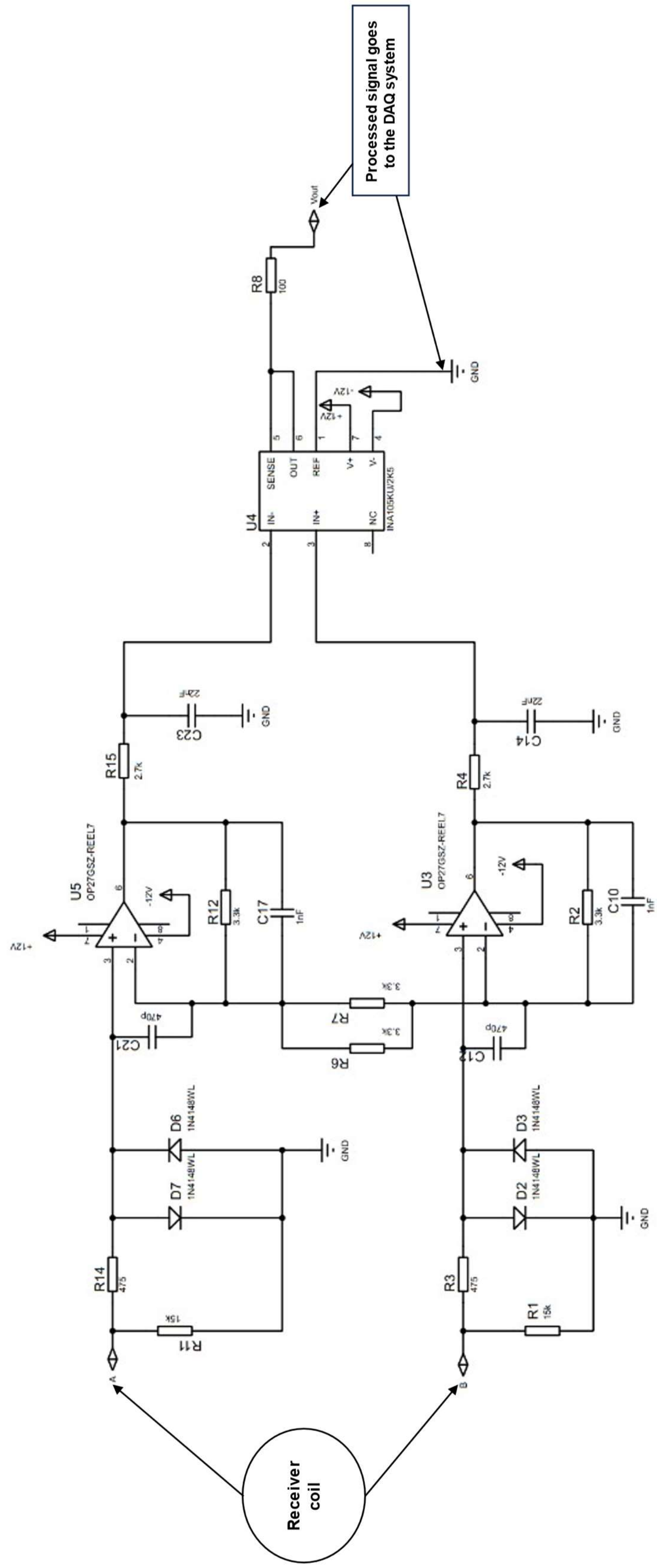

Figure 4-18: Circuit diagram of the receiver circuit for PEC signal acquisition.

4.6 Validation of PEC System through FEA and Experimental Data Comparison

Using the setup described in Section 4.4, the fully designed and manufactured PEC probe was tested across varying thickness steel plate samples to analyse the probe performance. Three steel plates, measuring 300.0 mm x 200.0 mm and nominal thicknesses of: 6.0 mm, 10.0 mm, and 20.0 mm, were utilised to capture and best represent common industrial plate and pipe wall thicknesses. During the testing, a lift-off distance of 1.0 mm was maintained between the probe and the sample, representing a practical balance between maximum signal energy at zero lift-off distance and what would be realistically achievable with a UAV.

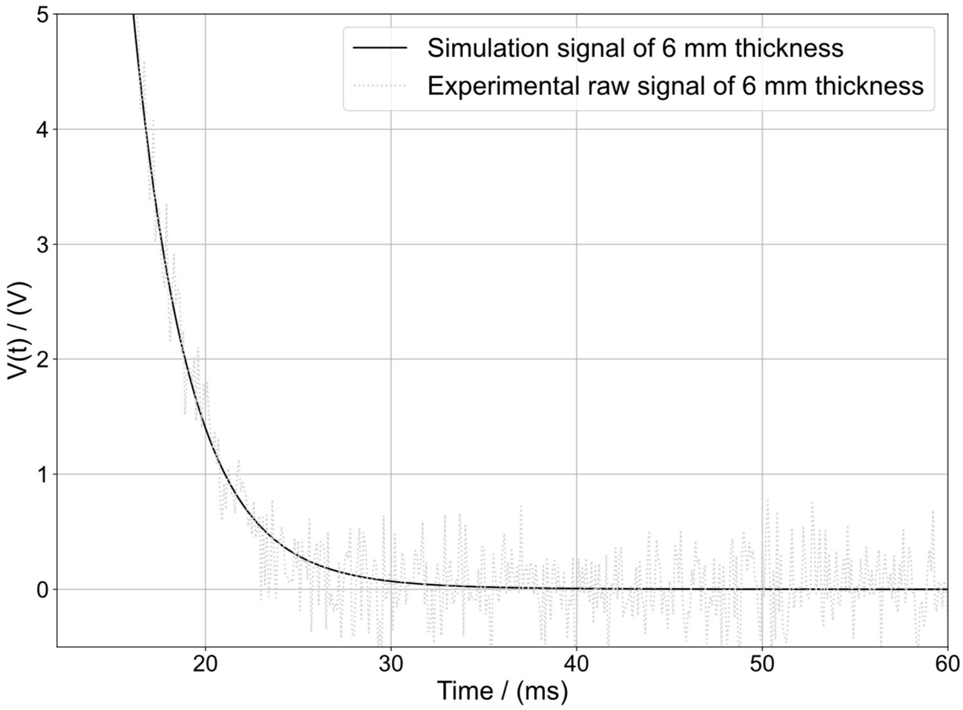

(a)

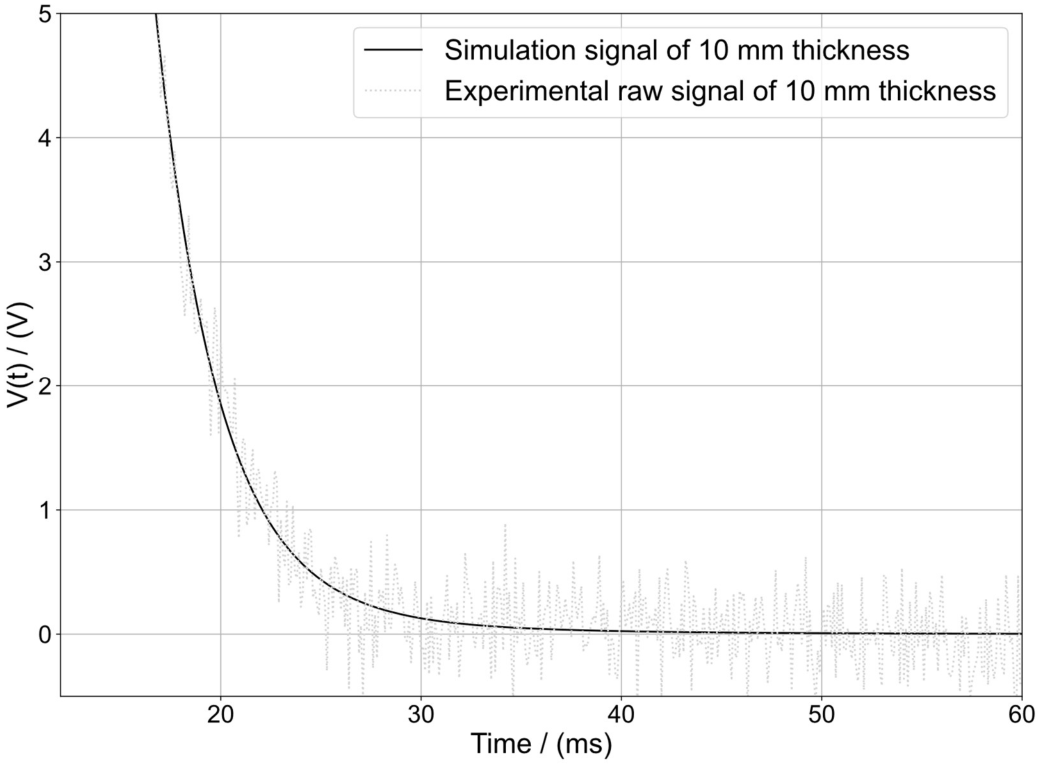

(b)

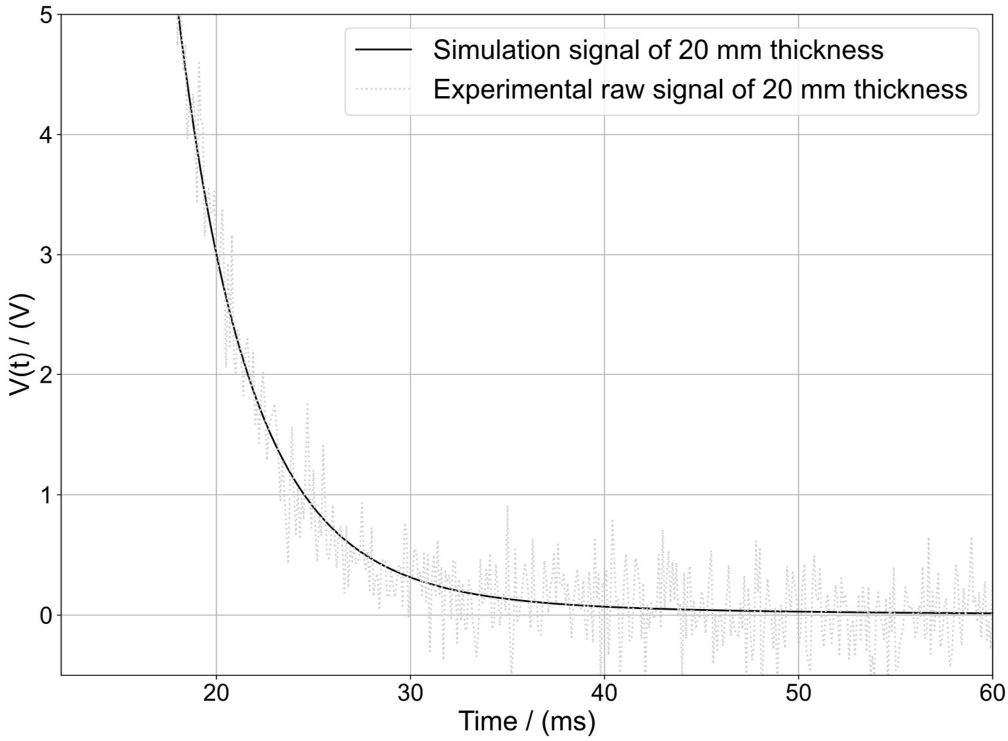

(c)

Figure 4-19: The simulation and experimental raw signals comparison of (a) 6.0 mm (b) 10.0 mm (c) 20.0 mm carbon steel sample.

The comparison between the FEA simulation signals and the experimental raw signal for varying thicknesses is depicted in Figure 4.22 above. Both the experimental and simulation signals exhibit the same decaying trend, but they do not show precise alignment. This discrepancy is proposed to be primarily due to the fact that the electrical and magnetic properties of the low carbon steel sample were not specifically measured for this study. In the FEA analysis conducted using COMSOL software, the default magnetization curve for low carbon steel (B-H loop) was employed. In reality, the material properties, such as magnetic permeability and electrical conductivity, can vary, which may lead to differences between the simulated and experimental results. Additionally, environmental factors such as temperature fluctuations and humidity were not controlled or accounted for in the experiments. These factors can impact the material properties and the performance of the PEC system. Temperature changes can cause thermal expansion or contraction, affecting the dimensions and magnetic properties of the sample. Humidity can influence the insulation and conductivity of the coils and other electronic components, potentially introducing variations in the signal.

Furthermore, the experimental setup includes factors such as a lossy medium, discretization limits in the analogue-to-digital converter, and high white noise margins. These factors are inevitable and constrain the accuracy of data acquisition. Moreover, differences in inductance values and wire resistance, which were not considered in the numerical modelling, can also contribute to the discrepancies observed between the experimental and simulation results.

Despite these limitations, the experimental results showed a consistent trend with the FEA analysis. Both the simulation and experimental data exhibited a similar decay pattern over time. The smaller the plate or pipe wall thickness is, the faster the PEC curve decays. This validates the general accuracy of the parameter studies conducted in Section 4.3.3. This consistency suggests that, although there are discrepancies due to the factors mentioned above, the overall approach and methodology are sound.

4.7 Conclusion

In this chapter, the analytical model of feature extraction method to calculate material thickness was reviewed. The design, fabrication, and analysis of a PEC sensor system aimed at mobile NDT and evaluation of ferro-magnetic material thickness was explored. The focus was on improving the sensitivity and accuracy of thickness measurements using a dual-coil configuration. The study involved both finite element analysis (FEA) simulations to compare the performance of single-coil and dual-coil setups. The dual-coil configuration demonstrated significant improvements in detecting variations in material thickness, exhibiting higher eddy current density and a more uniform distribution across the sample. The significant increase in the τ difference by a factor of 13.84 with the dual-coil configuration, compared to the single-coil configuration, demonstrates its superiority in providing comprehensive assessments of the internal structure of the steel sample. This is crucial for applications requiring precise and detailed pipe thickness measurements.

Additionally, the dimension parameters and lift off effect on the PEC received signal of the dual-coil configuration were investigated. The study on lift-off distances revealed that while signal amplitude decreases with increasing lift-off distance, the decay rate feature τ remains minimally affected, underscoring the robustness of the proposed probe design for autonomous aerial NDT applications. The investigation of horizontal distances between receiver coils demonstrated that smaller distances enhance sensitivity to thickness variations, with a 3 mm horizontal distance being optimal for practical implementation due to manufacturing tolerances. Lastly, the effects of varying vertical excitation-detector coil distances showed that while signal amplitude decreases with greater vertical distances, the sensitivity of the PEC system remains largely unaffected. These findings collectively inform the design parameters for maximizing the accuracy and reliability of the PEC sensor system in aerial NDT applications.

The development and implementation of the on-board PEC system has also been explained, including the PEC probe, signal excitation circuit, and signal reception and processing components. The integrated PEC system was designed for mobility, utilizing a 3D-printed probe frame, high heat-refection materials, and precise fabrication techniques to ensure structural integrity and functional efficiency. The excitation circuit was optimized to generate precise current pulses, crucial for inducing strong and measurable eddy currents in the test material. The receiver circuit effectively amplified the detected signals, ensuring high-quality data acquisition for accurate material thickness assessments. This comprehensive approach to PEC system design and implementation demonstrated the system's potential for autonomous NDT applications, particularly in mobile and remote inspection scenarios. The robustness and effectiveness of the developed system make it a valuable tool for material thickness evaluation.

Despite encountering some discrepancies between simulated and experimental results, attributed to factors such as material property variations, environmental conditions, and experimental setup limitations, the overall consistency in the trend of results validates the robustness of the proposed methodology and the FEA model. The experimental data consistently exhibited the expected decay patterns, reinforcing the reliability of the PEC system for autonomous NDT.

Chapter 5 Enhanced Pipe Thickness Measurement via UAV deployed Pulsed Eddy Current

5.1 Introduction

As outlined in Chapter 1, the integrity of pipeline infrastructure is a critical concern across various industries, including oil and gas, where maintaining uninterrupted service and ensuring safety are paramount. Traditional methods of NDE and NDT have relied heavily on manual inspection techniques, which are often labour-intensive, costly, and pose significant safety risks to personnel. The advent of robotic systems, particularly UAVs, offers a promising alternative by enabling remote inspection capabilities that can access hard-to-reach areas without human intervention.

This chapter focuses on the enhancement of pipe thickness measurement through the deployment of the PEC system developed in Chapter 4 via a UAV. The integration of UAV technology with PEC systems aims to address the limitations of conventional inspection methods by providing a more versatile, efficient, and safer solution for pipeline monitoring.

5.1.1 Robots for Exterior Pipe Inspection

Robotic inspection systems for exterior surfaces are widely used in in-service NDE processes and come in various forms. These systems include surface crawler robots and UAV platforms, with specific subvariants developed to meet particular process needs. The following provides an overview of existing approaches, supplemented with examples from recent literature discussed in more detail in Section 2.5, to facilitate the evaluation of their relative performance characteristics.

When comparing these systems, C-clamp style crawlers [129], [130] offer unparalleled platform stability. These crawlers utilize rigid mechanical clamping to nearly fully enclose the target, thereby fully supporting the vehicle and ensuring its Centre of Mass (CoM) is located within the pipe diameter. The strong reactive contact forces enable the use of simple motion control algorithms and allow for the precise deployment of NDE sensors in close proximity to the surface. Consequently, the sensors have a very short reach from the vehicle body, which eliminates the negative effects of lever-arm disturbance amplification on NDE data. However, these fully enclosed crawlers are unable to autonomously disengage and re-engage contact to navigate circumferential obstacles such as flanges, supports, or sharp bends. They can only pass small radial obstacles, like pipe junctions or valves, by aligning the obstacle with the small gap in their clamping mechanism used during initial deployment. This limitation renders certain areas of the target structure inaccessible without costly manual redeployment. Additionally, the clamp geometry restricts the maximum diameter of the enclosed asset, limiting the versatility of a single platform.

Flight offers a more versatile access solution, allowing the vehicle to briefly disengage from the surface to bypass obstacles and enabling deployment without direct manual intervention. The initial feasibility of this approach was demonstrated by depositing a discrete magnetic sensor package on top of a pipe using a standard unidirectional thrust quadrotor [131]. However, in this instance, the success rate of probe deployment was limited to below 65% due to near-surface aerodynamic disturbances [132], which commonly affect sensor placement accuracy and defect detection probability in underactuated UAVs [29].

In this way, recent UAV perching strategies have demonstrated significant improvements by minimising energy consumption and enhancing sensor stability compared to aerial manipulators. Some UAVs incorporate locomotion mechanisms, such as inchworm-like movement [133] or driven wheels [134], [135], to dynamically inspect suspected defects. However, other UAVs remain stationary after perching [136], [137], limiting their potential for NDE applications. Precise positioning of NDE transducers has also been achieved using onboard robotic arms while the UAV body passively supports itself atop the pipe surface [134], [135]. Nonetheless, the mass and reach of the robotic arms limit the scalability of these systems to large-diameter assets, as they lack adequate adhesion mechanisms to support their weight in positions other than atop the pipe.

5.1.2 PEC System Emendation Conception

As proposed in [100], a hybrid UAV-crawler vehicle is then identified as a novel and highly promising approach to combine the advantages and address the shortcomings of pipe exterior NDE systems. With an embedded PEC system, this hybrid UAV-crawler offers a new solution for examining pipe thickness from the exterior, as outlined in Table 5-1.

Table 5-1: A summary of the pipe exterior inspection robot

Reference	[129]	[130]	[131]	[135]	[100]	In the Chapter
Vehicle Type	Crawler	Crawler	UAV	UAV	UAV-Crawler	UAV-Crawler
Adhesion	Clamp	Clamp	Magnetic	Gravity	Thrust	Thrust
Pipe Coverage	Full	Full	Only Top	Full	Full	Full
Maximum Inspected Pipe Diameter (mm)	285	75	∞	250	∞	∞
NDT/NDE Method	None	Camera	EMAT	Ultrasonic	Camera	PEC
Probe Stability	Very high	Very high	Low	Mid	High	High

By utilising an airborne access method, this hybrid vehicle can eliminate costs associated with initial manual deployment, provided there is sufficient airspace clearance. During inspection, the vehicle engages in full-body pipe contact, significantly enhancing stability and disturbance rejection compared to free-flying systems [131]. With the customized electromagnetic interference (EMI) solution and data processing methods described in Section 4.5 and Section 5.2, this system, as shown in Figure 5-1, enables the collection of sufficient voltage signals with a relatively constant lift-off distance, functioning effectively as a remote non-contact NDT&E inspection platform.

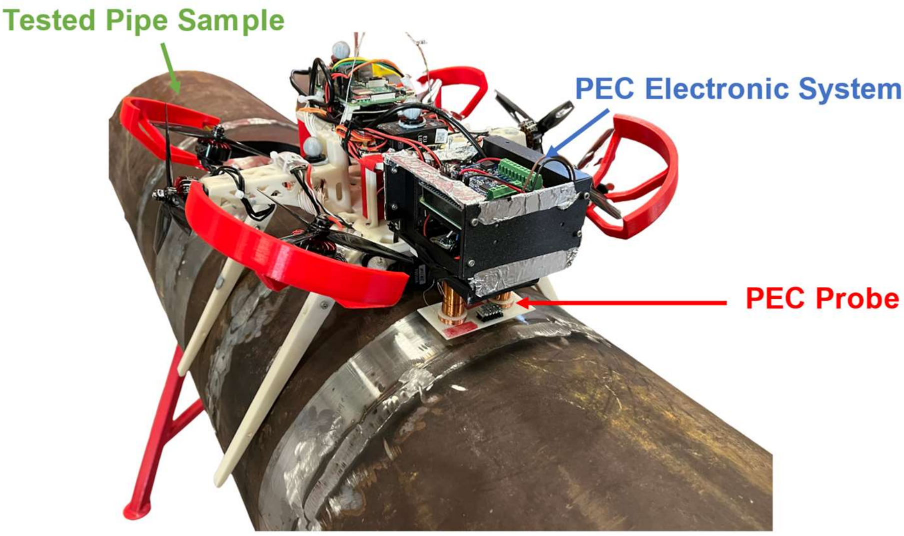

Figure 5-1: Aerial vehicle with the PEC sensor on the pipe sample.

5.2 Methodology

The research in this chapter employed an integrated approach combining UAVs with PEC technology to enhance the efficiency of NDT for pipeline infrastructure. The goal was to improve pipe thickness measurement and defect detection through a system capable of remote and automated operation. The methodology involves UAV-PEC system integration, signal processing for noise mitigation, and experimental validation to assess performance in real-world conditions.

The first step in the research involved changing the design of a hybrid UAV platform capable of performing PEC-based inspections. The UAV's design was optimized for stability and contact force control while carrying the PEC sensor payload, as shown in Figure 5-2. The sensor was mounted onto the UAV using a 3D-printed holder structure, ensuring that the sensor remained in close proximity to the surface without making physical contact, thereby maintaining a constant lift-off distance. This setup allowed for non-intrusive thickness measurements while the UAV traversed the pipe surface.

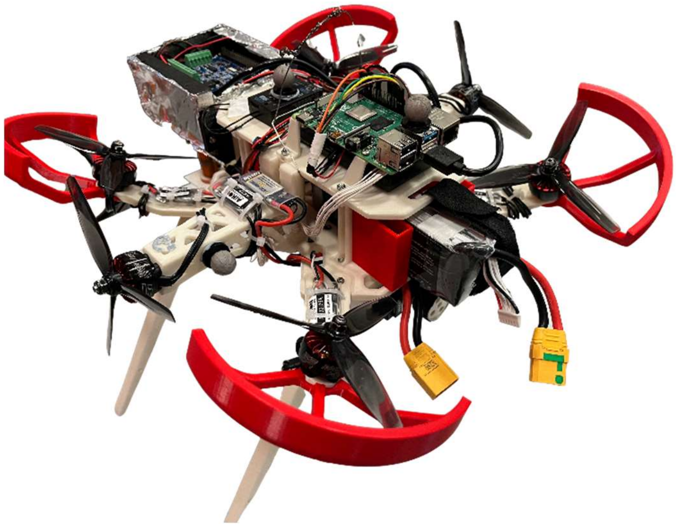

Figure 5-2: The aerial platform used in this thesis.

Signal processing was an essential part of the methodology due to the susceptibility of PEC signals to EMI generated by the UAV's motors and other environmental noise sources. To mitigate the impact of EMI on signal quality, a multi-step processing pipeline was applied. First, the Fourier Transform (FT) was used to convert time-domain signals into the frequency domain, enabling the identification and elimination of high-frequency noise. A Butterworth low-pass filter was then applied to further reduce noise, ensuring a smooth signal with minimal distortion. The filter parameters, such as cutoff frequency and filter order, were experimentally tuned to optimise the signal-to-noise ratio.

After noise filtering, the Savitzky-Golay filter was employed to smooth the signal without altering its key features. This step was crucial for preserving the decaying voltage curve characteristic of PEC signals, which is used for thickness calculation. The filtered signals were then processed to extract the feature τ, representing the time constant of the signal's logarithmic decay, which correlates directly with material thickness.

The experimental validation of the UAV-PEC system was conducted in two phases. The first phase involved the inspection of flat carbon steel plates with varying thicknesses to calibrate the PEC system. Trials were performed to establish a reliable relationship between the feature τ and the plate thickness. The second phase involved the inspection of a full-length carbon steel pipe with sections of different wall thicknesses. During this phase, the UAV maintained continuous contact with the pipe surface while performing circumferential scans. Measurements were taken at 25 points along the pipe's circumference.

Post-processing of the collected data involved averaging the measurements. The processed data were then compared against the reference thickness values of the pipe to evaluate the accuracy and precision of the UAV-PEC system. The experimental results demonstrated that the system could reliably distinguish between different thicknesses, with relative errors remaining below 5% in all measured cases.

5.2 Data Processing Methods and Results

In the context of UAV-based PEC inspections, signal processing is essential for extracting accurate and meaningful information from the raw data collected during inspections. The signals obtained from PEC sensors are often contaminated with noise and interference from various sources, including EMI, which can obscure the features of interest. Effective signal processing techniques are required to enhance the signal-to-noise ratio, isolate relevant signal components, and enable precise thickness measurements and defect detection. By applying these techniques, we can ensure the reliability and accuracy of the inspection results, which are crucial for maintaining the integrity of critical infrastructure.

To mitigate EMI noise during vehicle operation, digital post-processing of the signals received from the ADC is crucial. In this thesis, the Fourier Transform and Butterworth filters are initially employed to eliminate high-frequency noise. Subsequently, the Savitzky-Golay filter is applied to smooth the signal, facilitating accurate feature extraction. The following sections will elaborate on the principles of these methods.

5.2.1 Fourier Transform

The FT is a mathematical technique that transforms a time-domain signal into its constituent frequencies, providing a frequency-domain representation. This transformation is essential in various fields, including signal processing, communications, and audio engineering, where understanding the frequency components of a signal is crucial.

The Fourier Transform converts a signal from its original time domain to a representation in the frequency domain. This transformation is based on the principle that any time-domain signal can be represented as a sum of sinusoidal components of different frequencies. The continuous Fourier Transform of a time-domain signal x(t) is defined as:

$$X(f) = \int_{-\infty}^{\infty} x(t) e^{-j2\pi f t} dt \tag{5.1}$$

where: $X(f)$ is the Fourier Transform of $x(t)$, t is the time variable, f is the frequency variable, j is the imaginary unit.

The inverse Fourier Transform, which converts the frequency-domain signal back to the time domain, is given by:

$$x(t) = \int_{-\infty}^{\infty} X(f)e^{j2\pi ft}df \tag{5.2}$$

These equations form the basis for analysing signals in the frequency domain, allowing for the examination of amplitude and phase at various frequencies. However, in practical applications, signals are often discrete and finite in length. The Discrete Fourier Transform (DFT) is used to analyse such signals. The DFT of a discrete-time signal $x[n]$ with N samples is defined as:

$$X[k] = \sum_{n=0}^{N-1} x[n]e^{-j\frac{2\pi}{N}kn} \tag{5.3}$$

for $k = 0, 1, \dots, n$, where $X[k]$ is the DFT of $x[n]$, N is the number of samples, k is the index of the frequency component.

The inverse DFT (IDFT) is given by:

$$x[n] = \frac{1}{N}\sum_{k=0}^{N-1} X[k]e^{j\frac{2\pi}{N}kn} \tag{5.4}$$

The Fast Fourier Transform (FFT) is an efficient algorithm for computing the DFT. The FFT reduces the computational complexity from $O(N^2)$ to $O(N \log N)$, making it feasible to perform Fourier analysis on large datasets. The most commonly used FFT algorithm is the Cooley-Tukey algorithm [138], which recursively breaks down the DFT into smaller DFTs. The Cooley-Tukey algorithm exploits the symmetry and periodicity properties of the DFT to reduce the number of computations. The basic idea is to decompose the DFT of a sequence of length N into two DFTs of length $N/2$. This process is repeated recursively until the sequence length is reduced to 1. For an input sequence $x[n]$ of length N, the DFT can be expressed as:

$$X[k] = \sum_{n=0}^{N-1} x[n] e^{-j\frac{2\pi}{N}kn} \tag{5.5}$$

This can be rewritten as:

$$X[k] = \sum_{n=0}^{N/2-1} x[2n] e^{-j\frac{2\pi}{N}k(2n)} + \sum_{n=0}^{N/2-1} x[2n+1] e^{-j\frac{2\pi}{N}k(2n+1)} \tag{5.6}$$

where $x[2n]$ and $x[2n+1]$ are the even and odd indexed elements of $x[n]$, respectively. This decomposition reduces the number of multiplications required, significantly speeding up the computation.

5.2.2 Butterworth Filters

The Butterworth filter, first introduced by Stephen Butterworth in his 1930 paper "On the Theory of Filter Amplifiers," is renowned for its maximally flat frequency response in the passband. This characteristic makes it an ideal choice for various signal processing applications, including audio, communications, and biomedical engineering, where a smooth passband is crucial. This section delves into the theoretical underpinnings of Butterworth filters, covering their mathematical foundation, frequency response characteristics, and essential properties. The Butterworth filter is designed to have a flat frequency response in the passband, meaning there are no ripples, and it transitions smoothly to the stopband. The magnitude response $|H(j\omega)|$ of an n-order Butterworth low-pass filter is given by:

$$|H(j\omega)|^2 = \frac{1}{1+\left(\frac{\omega}{\omega_c}\right)^{2n}} \tag{5.7}$$

Where ω is the angular frequency, ω_c is the cutoff angular frequency, n is the filter order.

This equation shows that at $\omega = 0$, the magnitude response is 1, indicating no attenuation. As ω approaches ω_c, the response starts to decrease, and for frequencies much higher than ω_c, the response falls off sharply. The higher the order n, the steeper the roll-off at the cutoff frequency, resulting in better attenuation of frequencies beyond the cutoff. The simulation and correlation analysis of the Butterworth low-pass filter are completed. The performance indicators of the digital filter include a passband cutoff frequency of 200 Hz, a stopband cutoff frequency of 400 Hz, a maximum passband attenuation of 0.5 dB, a minimum stopband attenuation of 40 dB, and a sampling frequency of 2000 Hz, as shown in Figure 5-3. This illustrates that the higher the order, the faster the descent.

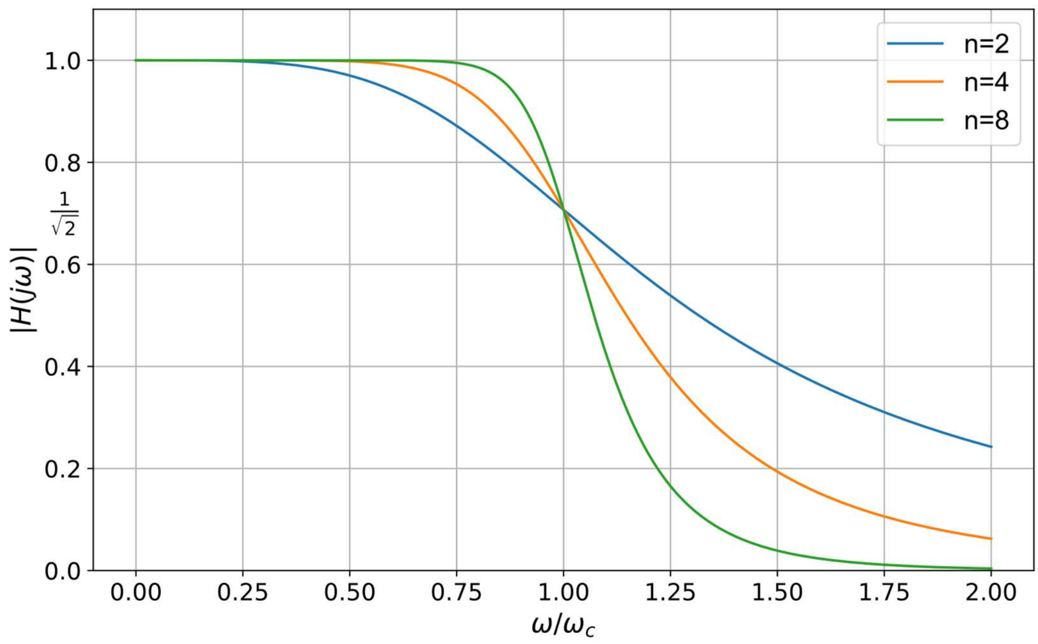

Figure 5-3: Butterworth filters of different orders.

Other types of low-pass filter such as Chebyshev filter and elliptic filter have their advantages and disadvantages. Chebyshev filter has flat stopband, but its transient characteristics are poor [139] while the elliptic filters has fast and disordered attenuation but it is so complex that it is hard to implement [140]. Table 5-2 concludes the advantages and disadvantages of Butterworth filter, Chebyshev filter and elliptic filter. Because PEC systems use transient inputs, and the Elliptic filter is computationally intensive, the Butterworth low-pass filter was chosen in this data-processing chapter.

Table 5-2: Comparison of different filters

Filter Type	Advantages	Disadvantages
Butterworth	● Good amplitude and transient characteristics ● Smooth response in both passband and stopband ● For a given order and ripple requirement, the transition band is narrow	● Slow roll-off ●Poor stopband attenuation
Chebyshev	● Equal ripple in the passband ● Flat stopband ● Steeper transition band than Butterworth	● Poor transient characteristics
Elliptic	● Fast and steep attenuation rate in the transition area ● Good frequency characteristics ● Narrow transition zone	● Complex transfer function ● Computationally intensive ● Difficult to adjust

5.2.3 Savitzky-Golay Filter

The Savitzky-Golay filter, also known as the digital smoothing polynomial filter or least-squares smoothing filter, is a crucial tool in the preprocessing stage of signal processing, especially in the context of enhancing signal quality without significantly distorting the signal's original characteristics [141]. This section provides a theoretical background on the Savitzky-Golay filter and its application in the context of digital signal processing as utilized in the referenced studies.

The primary objective of the Savitzky-Golay filter is to smooth a noisy signal by fitting successive sub-sets of adjacent data points with a low-degree polynomial by the method of linear least squares. The polynomial's value at the central point of each subset is then used to replace the original point in the smoothed signal. This method is particularly effective in preserving the essential shape and features of the signal's waveform, such as peak heights and widths, which is critical in applications requiring precise signal interpretation. Let $y(i)$ be the original signal and $x(i)$be the smoothed signal. The filter works by applying a convolution operation using a set of precomputed convolution coefficients. These coefficients are determined by the least-squares fitting of a polynomial of degree p to a window of $2m + 1$ points around each point i [141].

$$x(i) = \sum_{j=-m}^{m} c(j) y(i + j) \tag{5.8}$$

where $c(j)$ are the convolution coefficients that depend on the polynomial degree p and the window size $2m + 1$. These coefficients are derived by minimizing the sum of the squares of the differences between the data points and the polynomial fit.

In the context of the referenced studies in [63] and [142], the Savitzky-Golay filter is employed to preprocess the raw signals obtained from PEC sensors used for NDT of cast iron thickness. The primary advantage of using the Savitzky-Golay filter in this application is its ability to smooth the noisy decaying voltage signals without significantly altering the underlying characteristics of the signal, such as its logarithmic decay behaviour, which is critical for accurate thickness estimation. By applying the Savitzky-Golay filter, the noisy signal is transformed into a smoother version, which facilitates more accurate and robust interpretation algorithms, such as the Adaptive Least Square Fitting Line (ALSFL) strategy described in the referenced documents. The filter helps in maintaining the integrity of the signal's essential features, which are necessary for subsequent steps in the signal processing pipeline, including gradient computation and thickness derivation. However, there are limitations to consider. The filter can introduce distortions at the signal boundaries due to the asymmetric distribution of data points, which leads to insufficient data for accurate polynomial fitting. Moreover, the performance of the filter depends on the choice of polynomial degree and window size, requiring careful tuning for optimal results.

5.2.4 Data Processing Results Comparison

During the data processing, the collected signal from the ADC device first undergoes FFT. Next, a digital Butterworth filter is applied, followed by IFFT, as illustrated in Figure 5-4. For our specific application, the suitable cut-off frequency ω_c was set at 200 Hz after experimental trials, while the sampling rate fs was set at 40 kHz, fast enough data for processing. The choice of the filter order n, was set at 3 after analysis. Due to the noise caused by the electromagnetic interference from the motors of the UAV in operation, it is crucial to set a value for the cut-off frequency. It is worth noting that the selection of ω_c and n was guided by the specific requirements of our analysis and refined through fine parameter tuning. Figure 5-5 displays a comparison between the original signal and the one processed through a low-pass filter when the UAV was in operation.

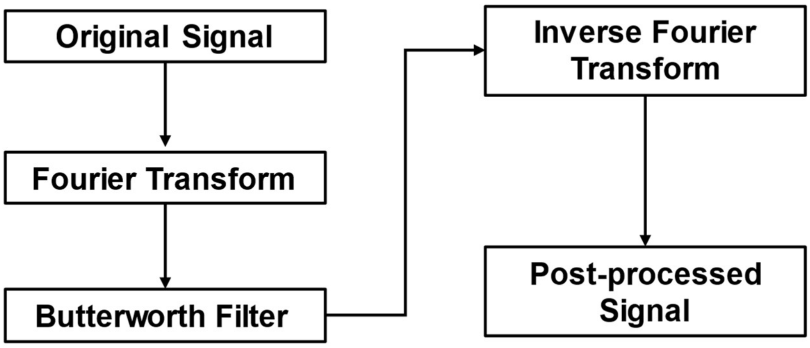

Figure 5-4: Flow chart of signal processing procedure

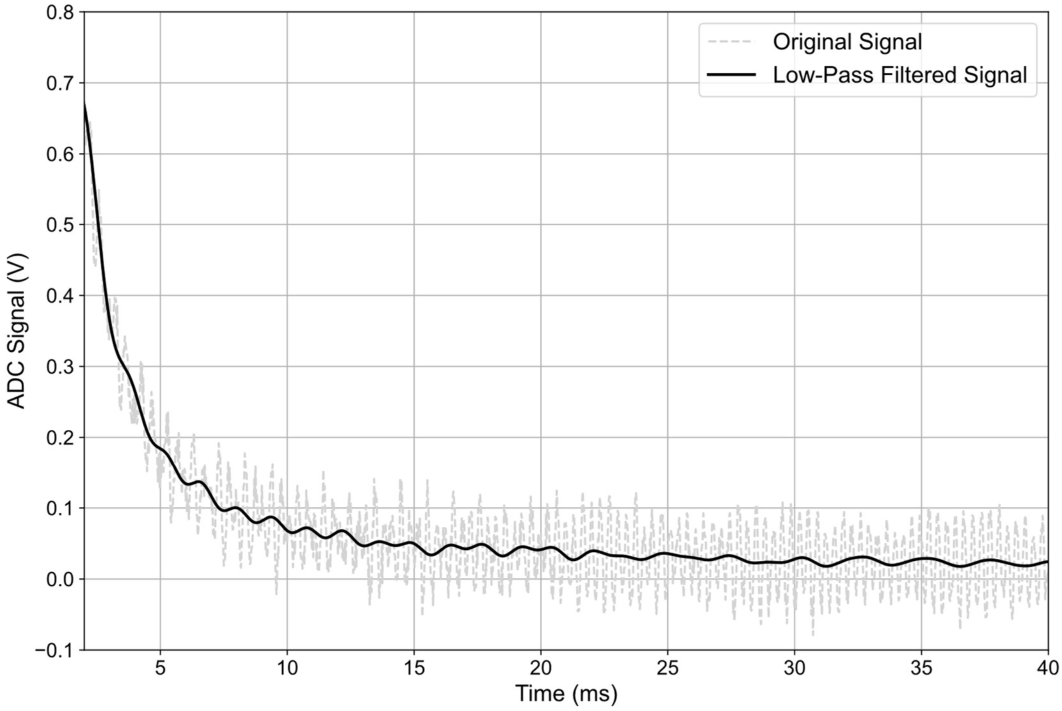

Figure 5-5: Comparison of unprocessed and post-processed signals using low-pass filter when the UAV was in operation (Raw signal post-amplification)

In this research, after passing the raw signal through a low-pass filter, the signal required further smoothing for effective post-processing. To address the noise levels and accurately identify the appropriate linear region for extracting the feature τ, the Savitzky-Golay filter was employed with a window size of 201 and a polynomial degree of 30, as stated in Section 5.2.3. This approach, which involves smoothing the captured raw signal prior to τ extraction, aligns with methodologies used in previous studies mentioned in [63], [143] and [141], was implemented to enhance the clarity and reliability of the signal analysis in our current research. Figure 5-6 displays a comparison between the original signal and the one processed through a low-pass filter and Savitzky-Golay filter when the UAV was in operation. This processing significantly reduces noise in the signal, thus preparing it for the extraction of the feature τ, indicating the signal's readiness for detailed analysis in Section 5.6.

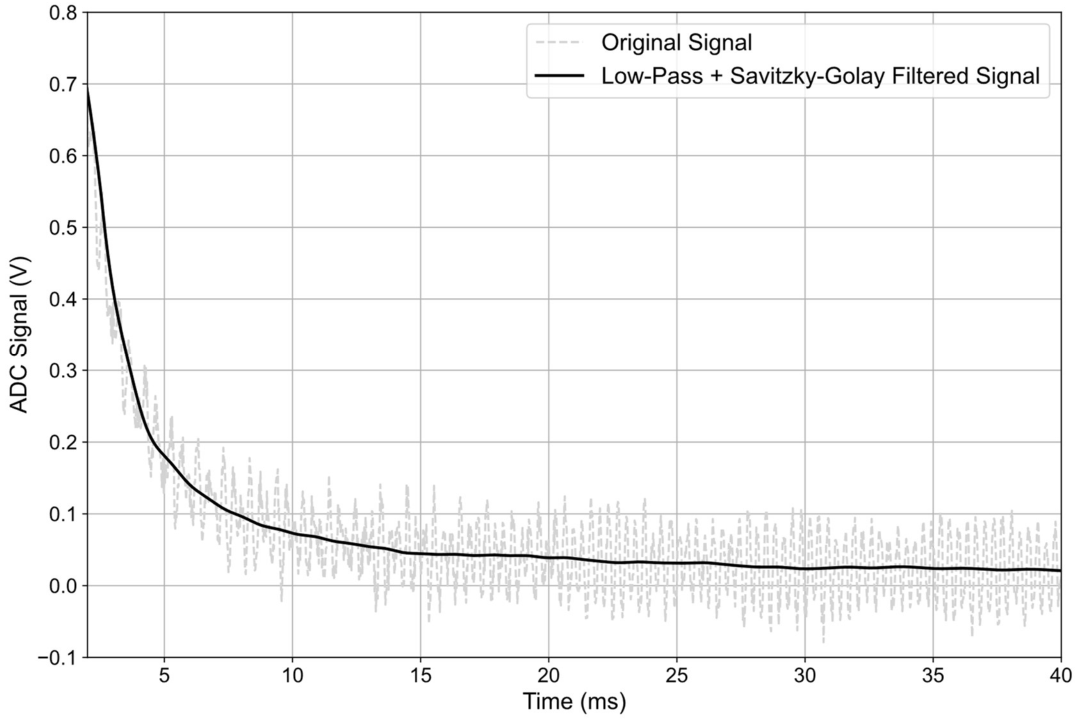

Figure 5-6: Comparison of unprocessed and post-processed signals using low-pass filter and Savitzky-Golay filter when the UAV was in operation (Raw signal post-amplification)

5.3 Unmanned Aerial Vehicles Platform for Inspection

In the development of the hybrid UAV-crawler vehicle outlined in [31], the original design incorporated a rigid-body model for thrust actuation and interaction with cylindrical pipelines. The PEC payload was integrated into this model. To fully define the rigid vehicle model, three coordinate frames were used: $\{W\}$, the global world frame, which describes the positions of the asset and vehicle relative to their surroundings; $\{B\}$, the body frame of the UAV-crawler, with its origin at the vehicle's CoM; and $\{P\}$, the pipe-relative frame, centred at the pipe's midpoint, with the x-axis aligned with the pipe's length and the z-axis pointing upwards.

5.3.1 Vehicle Overview

The UAV platform, depicted in Figure 5-7 represents an innovative, dedicated platform designed for deploying NDT sensors, in consistent proximity to the surfaces of cylindrical structures like pipes.

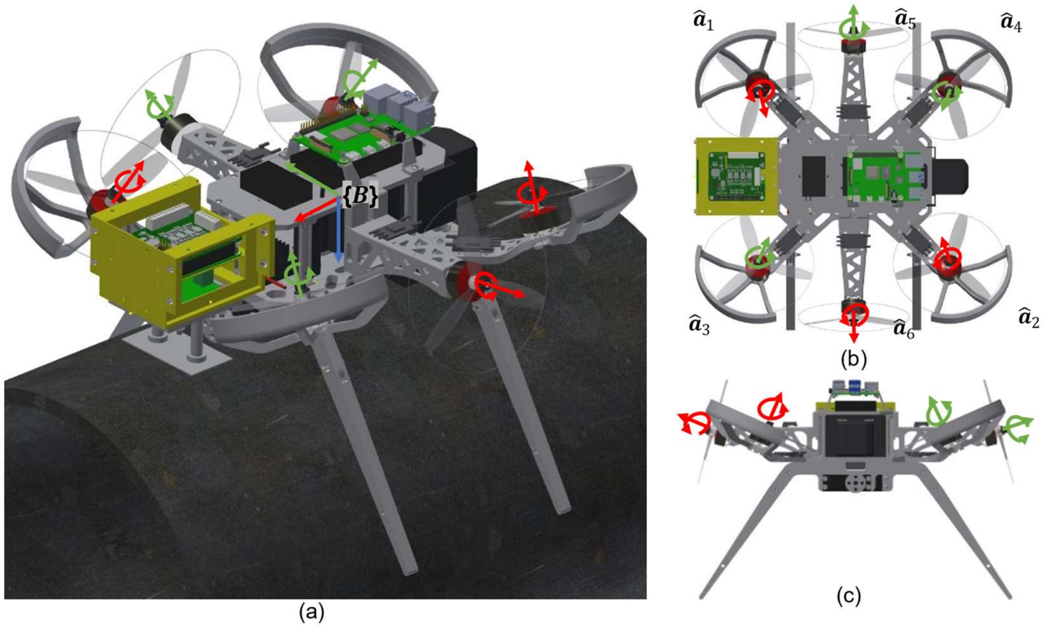

Figure 5-7: (a) A hybrid vehicle prototype diagram with PEC payload. (b) Top view and front view of the vehicle. The vectors defining the positive thrust direction of each propeller. Red vectors spin counter-clockwise; blue ones spin clockwise.

This UAV model is equipped with six arranged, 5-inch, fixed-pitch, reversible propellers, providing the omnidirectional net force in the $\{B\}$ y-z plane. These propellers are equipped with HQprop 3D-5x3.5x3 propeller [144], have equal thrust capabilities in both spin directions, enabling the UAV to fly like a normal drone and also to invert its thrust output completely. These have equal thrust efficacy in both spin directions, are driven by iFlight Xing 2207 motors [145], and powered by a 22.2 V (6S) 3300 mAh Li-Po battery [146]. And ikon AK32 Electronic Speed Controller (ESC) firmware [147] were used to enables run-time spin reversal and send telemetry data back to the flight controller.

Target contact occurs at six points, symmetrical in the $\{B\}$ y-z plane. At the front and rear, two FS5106R continuous rotation servo wheels [148] with high-grip polyurethane elastomer tires provide surface locomotion under adaptive thrust support. Two pairs of rigid legs are also added, providing a further four points of contact to constrain vehicle yaw and increase stability. These are designed for a known approximate target diameter and trivially adapted to fit American Society of Mechanical Engineers (ASME) standard pipes [149], or other targets above 160 mm diameter.

The arrangement includes four propellers inclined at 25° from the vertical and two tilted 15° above the horizontal plane, allowing for a combined thrust capability of up to ±30.8 N vertically and ±28.8 N horizontally relative to the drone's frame [100].

This thrust is suitable for the UAV, which weighs 1.91 kg with a 272 g PEC sensor system payload. This payload is broken down as the following Table 5-3. To maintain the stable flight without shaking the internal components of the PEC sensor system, a robust mounting structure is designed, the developed 3-D model of this is depicted as yellow colour in Figure 5-8.

Table 5-3: PEC system payload breakdown

	Mass (g)
3-D Printed Holder Structure	77
PEC Probe (Including coils)	122
Excitation Board	12
Raspberry Pi W 2	11
AD HAT	50

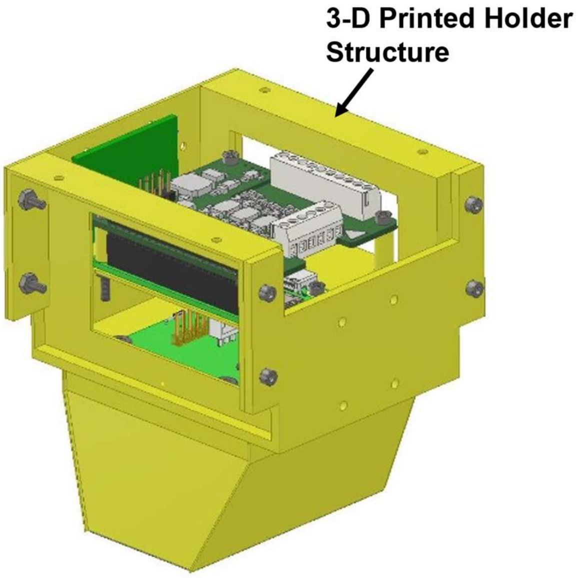

Figure 5-8: The CAD model of the PEC system mounted on the vehicle.

In this way, the vehicle is able to maintain contact forces exceeding 8 N in every direction around a cylindrical target, moving across its surface after landing without the need for magnetic or vacuum-based attachment methods. The UAV is equipped with two continuous rotation servos for movement, making it a hybrid between a drone and a robotic crawler. These servos, along with rigid legs that stabilize the UAV and can adjust to wrap around pipelines, ensure precise contact and navigation around the target. Running on a customized PX4 flight control software, this UAV platform uses a rigid body interaction model for stable flight around cylindrical objects. An Inertial Measurement Unit (IMU) provides all necessary data, allowing for efficient use in industrial environments without external positioning systems.

5.3.2 Mathematical Contact Model

As purposed in [150], the mathematical model describing the model is relevant to the work. For the vehicle with the PEC system, the model was developed to describe the interaction between the hybrid UAV-crawler and a cylindrical asset, i.e. the pipeline, depicted in Figure 5-9.

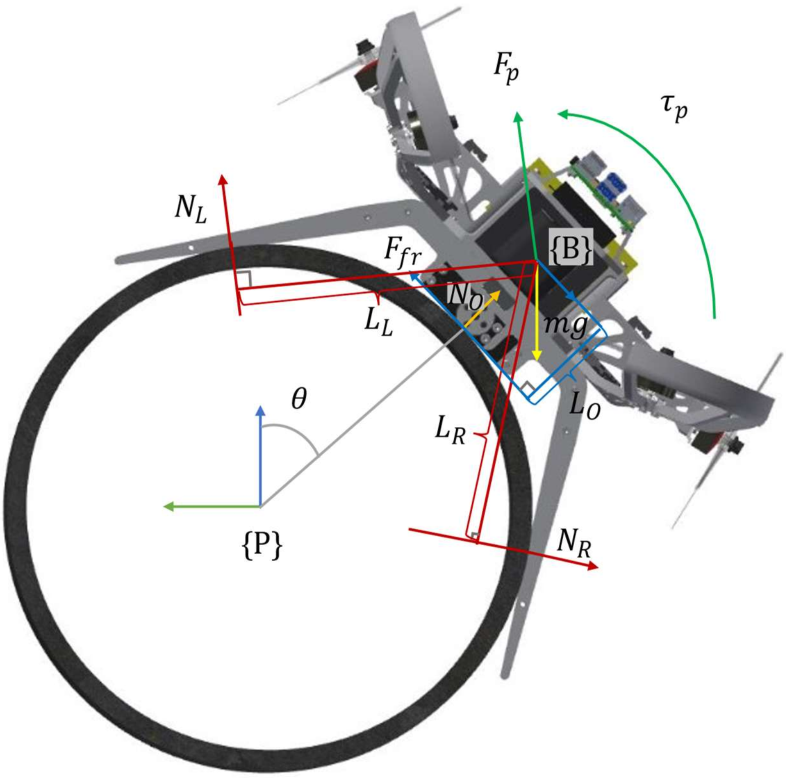

(a)

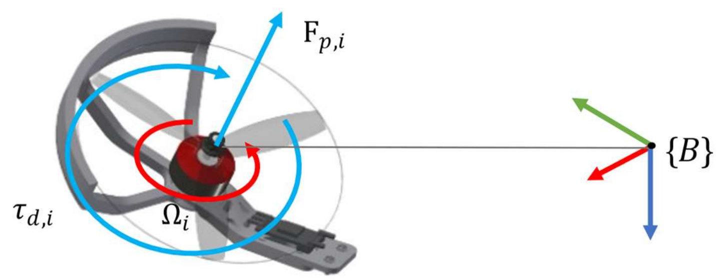

(b)

Figure 5-9: Free-body forces and torques diagram acting on the UAV-crawler vehicle with PEC payload. (a) Overview (b) Propellers. Grey vectors indicate forace application points relative to $\{B\}$.

The vehicle's angular position around the surface of the pipe is fully described by the clockface angle, $\theta \in [-180°, +180°]$, which is zero when the vehicle is atop the pipe and positive with clockwise rotation, conveniently matching the UAV roll angle.

The wrench components acting on the vehicle are examined in the body-relative frame $\{B\}$ to develop an interaction model foundational for onboard control. By exploiting system symmetry in the $\{B\}$ y-z plane, this interaction can be simplified to a 2D model for horizontal-axis cylindrical targets. The contact forces at the front and rear of the vehicle are approximately equal and are combined into single parameters.

The wheels split the normal contact and Coulomb friction force vectors, N_O and F_{fr}, respectively. Both F_{fr} and N_O act at L_O, directed in the $\{B\}$ y-axis and negative z-axis, respectively. The magnitude of the friction vector at the wheel is limited by the static friction coefficient, μ, as follows:

$$|\mathrm{F_{fr}}| \leq \mu \mathrm{N_O} \tag{5.9}$$

The remaining normal contact forces of the left and right leg pairs, N_L and N_R, act at points L_L and L_R with direction unit vectors $\widehat{n_L}$ and $\widehat{n_R}$, respectively. Friction effects at these contact points are neglected for simplicity due to the low-friction interaction between the plastic legs and target surface material compared to the rubberized tires.

Within the model for horizontal pipe interaction, the weight vector of the vehicle, mg, remains constant in magnitude, as it is the product of the vehicle's mass, m, and the gravitational acceleration, g. However, the orientation of this weight vector relative to the pipe surface changes as the vehicle moves around the pipe, defined by the angle θ. Specifically, the components of the weight along the vertical and horizontal axes vary as a function of θ, with the sine and cosine terms representing the projection of the weight along these axes at different clockface positions:

$$\mathrm{mg}(\theta) = \mathrm{mg}[0\ \sin\theta\ \ \cos\theta]^{\mathrm{T}} \tag{5.10}$$

Expanding the model framework, collective propeller behaviour is characterized by their net force, F_p, and torque, τ_p, vectors acting through the centre of mass. Each propeller exerts static thrust, $F_{p,i}$, and drag torque, $\tau_{d,i}$, varying as a function of its rotation speed, Ω_i, and lumped thrust, C_T, or drag, C_D, coefficients:

$$\mathrm{F_{p,i}} = \mathrm{C_T}\Omega_i^2 \cdot \widehat{e_i} \tag{5.11}$$

$$\tau_{d,i} = s_i C_D \Omega_i^2 \cdot \widehat{e_i} \tag{5.12}$$

These coefficients are determined by the propeller aerofoil and vary with air density and rotor radius. Thrust acts on the airframe at point p_i.

The collective propeller wrench is included in the consideration of the net wrench across all interaction forces and torques. Summation gives a single net force acting through the centre of mass and a single net torque acting about it, as follows:

$$\sum \mathrm{F_B} = \mathrm{N_O} + \mathrm{F_{fr}} + \mathrm{N_L} + \mathrm{N_R} + \mathrm{mg}(\theta) + \mathrm{F_p} \tag{5.13}$$

$$\sum \tau_B = (\mathrm{L_O} \times \mathrm{N_O}) + (\mathrm{L_O} \times \mathrm{F_{fr}}) + (\mathrm{L_L} \times \mathrm{N_L}) + (\mathrm{L_R} \times \mathrm{N_R}) + \tau_p \tag{5.14}$$

For vehicle support around the target circumference, the interaction is considered quasi-static, with net force-torque vectors equating to zero:

$$\sum \mathrm{F_B} = 0 \tag{5.15}$$

$$\sum \tau_B = 0 \tag{5.16}$$

This condition simplifies vehicle surface crawling behaviour during inspection, as slow motion requires minimal centripetal force relative to the weight support force.

To ensure the feasibility of a hybrid UAV designed for circumferential contact inspection, it is essential to establish the minimum supporting wrench required to maintain a stable pose on a cylindrical surface. This section outlines the derivation and application of this requirement.

Recognizing that the vehicle's legs can adapt to different asset diameters and provide beneficial contact forces, a conservative approach is taken by excluding these effects. This ensures that the vehicle can maintain stability across all possible diameters. From Eq. 5.15, the minimum supporting force vector at any clockface angle is determined by minimizing the residual force vector's magnitude that the vehicle must support:

$$\mathrm{argmin}_{N_O, F_{fr}} |N_O + F_{fr} + mg(\theta)| \tag{5.17}$$

Subject to:

$$N_O \geq N_{\min}$$

$$-\mu N_O \leq F_{fr} \leq +\mu N_O$$

These constraints include the limits of static friction and impose a minimum permissible wheel contact force, $N_{\min}$, at any point around the circumference. Setting $N_{\min} = 15\,\mathrm{N}$ ensures the vehicle exerts a strong radial contact force, enhancing position stability and robustness to disturbances. A safety factor is applied to the static friction coefficient, μ, typically set at 0.05, which accommodates model uncertainties and potential surface conditions like dust and moisture.

By solving for N_O and F_{fr} and substituting these into Eq. 5.17 and Eq. 5.18, the minimum supporting force vector $F_s(\theta)$ and the required torque vector $\tau_s(\theta)$ for static equilibrium are obtained. These vectors define the minimum support wrench:

$$W_S(\theta) = \begin{bmatrix} F_s(\theta) \\ \tau_s(\theta) \end{bmatrix} \tag{5.18}$$

Feasibility is achieved if, at all clockface angles, the required support wrench lies within the feasible net propeller wrench set Γ_p:

$$W_s(\theta) \in \Gamma_p \quad \forall\theta \tag{5.19}$$

This condition guides the design and optimization of the propeller array, ensuring that the UAV with PEC system payload can maintain stable contact-based inspection on cylindrical assets of various diameters.

5.4 Experimental Analysis

5.4.1 Flat Carbon Steel Plate Inspection

To understand the correlation between the feature τ and across varying steel sample thickness T, a carbon steel sample measuring 300.0 mm x 200.0 mm, with thicknesses of 2.0 mm, 6.0 mm, 10.0 mm, and 20.0 mm, maintaining a lift-off distance of 1.0 mm.

However, our intention was to use the logarithmic decay rate as a signal feature for thickness quantification of cylindrical structures, i.e., large diameter in-situ pipes. It could be hypothesized that the plate approximation is reasonable given large diameter pipes investigated are of radius R = 162.0 mm, shown in Fig. 10, while the sensor width w = 41.9 mm in the direction perpendicular to the pipe axis. As illustrated in [151], pipe with radius satisfying w/R < 0.25 produces variations in τ of less than 1% for the sensor. Given the radius of the pipes scanned in this work, the maximum w/R value encountered was 0.246, thus the approximation of large diameter pipe surfaces as flat plates holds for practical purposes in the scenario examined herein.

Moreover, during the final pipe dynamic test, the lift-off distance between the probe and the pipe surface was set to 4.5 mm, as shown in Figure 5-10, maintaining a contactless approach. As the probe design is verified to be minimally sensitive to lift off distance in Chapter 4, $\tau \propto T^2$ suits the final pipe dynamic test requirements. Fifteen measurements were taken and then averaged for each thickness to eliminate uncertainty factors.

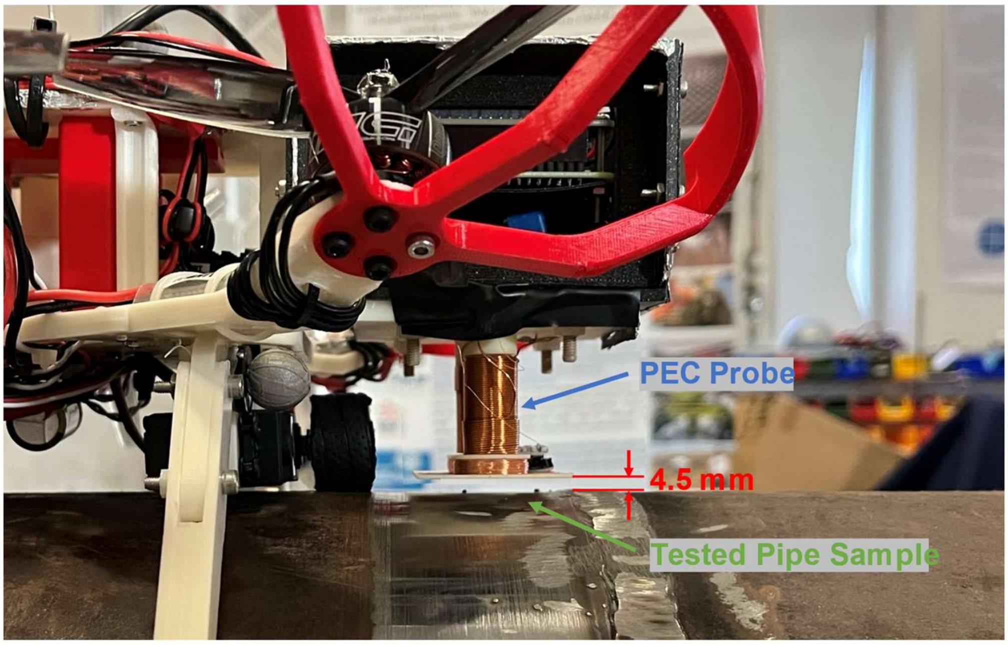

Figure 5-10: The lift-off distance between the PEC probe and the tested pipe sample in the experiment.

5.4.2 Pulsed Eddy Current Calibration

The calibration of the PEC system is a critical step in ensuring accurate thickness measurements of steel samples. The feature τ is used as the primary indicator of material thickness, derived from the decaying voltage signals captured by the PEC sensors.

Through the theory in Chapter 4 Section 4.2 indicates that the τ feature has to be captured as time t tends to reach infinity in equation 4.9, this is because the significant portion of the signal that contains the thickness information occurs in the later stages of the decay process. As can be seen from Fig. 12, the signals pass the noise limit (i.e., $ln[V(t)] < -6$) of the signal sampling circuitry as time increases. Therefore, we select the later stage of signals (i.e., $-6 < ln[V(t)] < -4.3$) to extract τ. Moreover, the feature τ is simply the reciprocal of the absolute of the gradient of $ln[V(t)]$ when $t \rightarrow \infty$.

By applying the line-fitting algorithm described in Chapter 4 Section 4.2, the τ value could be extracted from the four situations, with 2.0 mm of τ = 0.136, 6.0 mm with $\tau = 1.727$, 10.0 mm with τ = 4.679 and 20.0 mm with $\tau = 18.662$. The trend is used to model the relationship between thickness and τ to predict unknown thickness with known received PEC signal, which is shown in Figure 5-11. The fitted curve of the relationship between the thickness T and the extracted feature τ could be achieved as $\tau = 0.0467T^2$, as depicted in Figure 5-12.

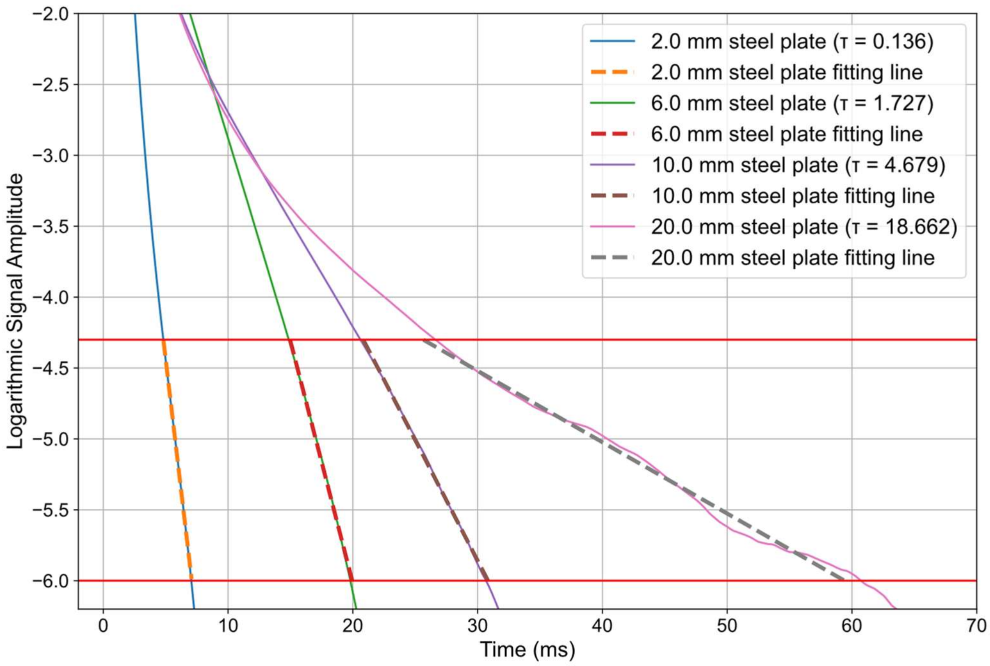

Figure 5-11: PEC responses of steel plate sample with line fitting.

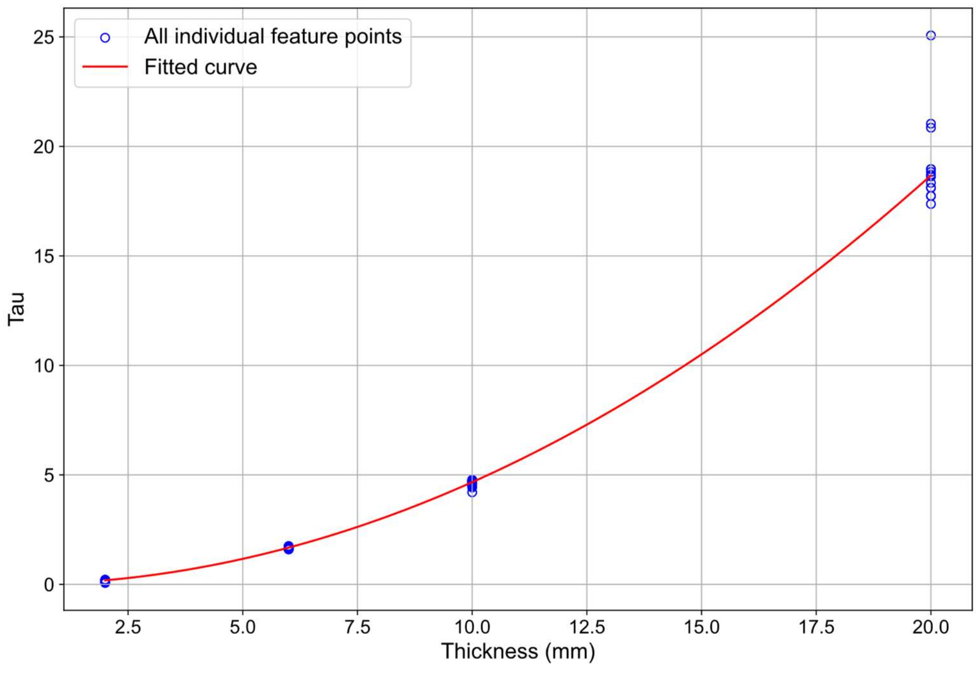

Figure 5-12: Fitted curve of thickness versus τ.

5.4.3 Carbon Steel Pipe Sample

The final phase of the experiment, aimed at mapping the thickness of a pipe, involved piloting a vehicle equipped with a PEC sensor system around the pipe's entire circumference while maintaining constant vehicle contact. The experiment utilised a nominal 1400.0 mm long, Schedule 80, pipe composed of five sections, each with a 12.75-inch (324.0 mm) outer diameter, made of low carbon steel. The ends of the assembly had a thickness of 37.0 mm over 400.0 mm lengths. In between these ends, three sections varied in thickness—20.0 mm, 10.0 mm, and 6.0 mm, respectively, over a total length of 200.0 mm, as depicted in Figure 5-13.

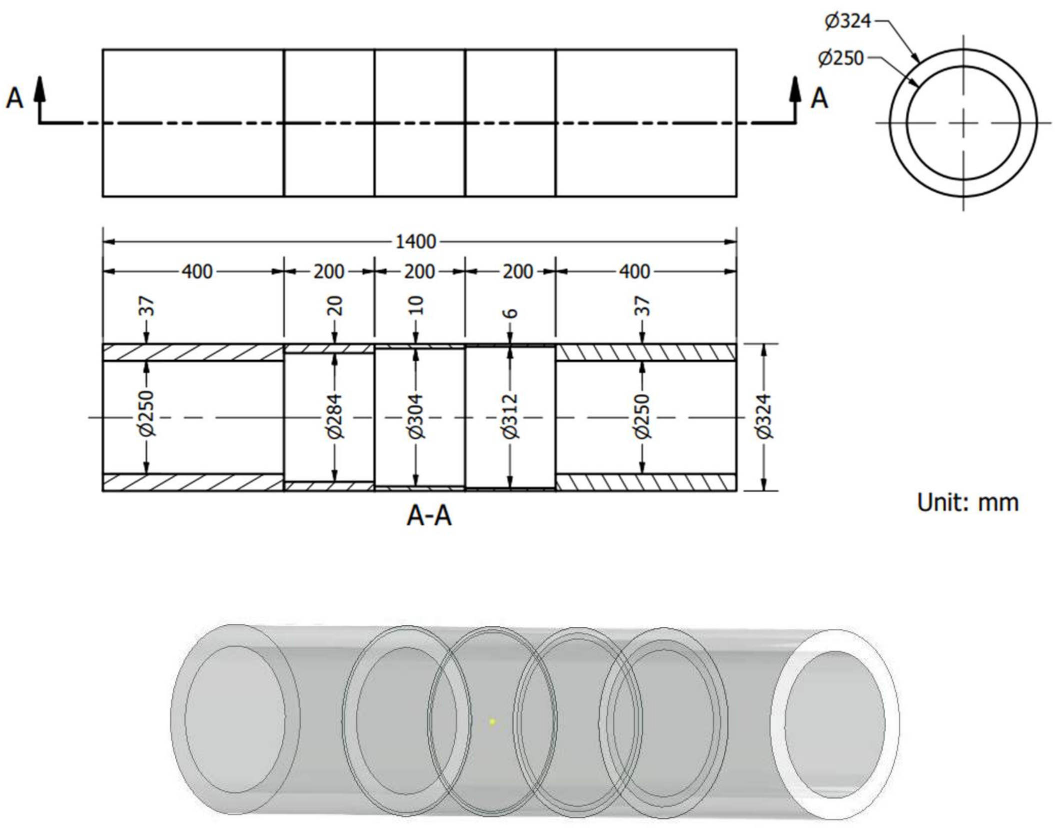

Figure 5-13: The pipe sample (a) 2-D viewing of the tested pipe sample, (b) 3-D viewing of the tested pipe sample.

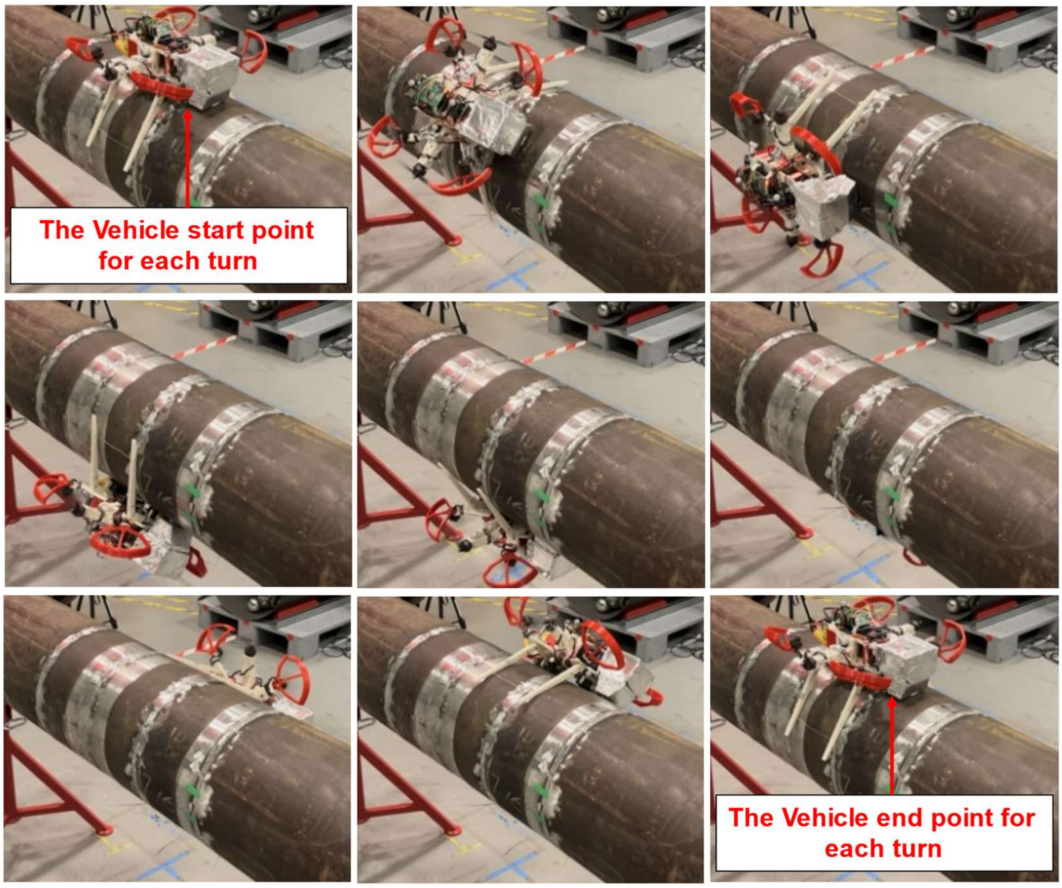

Figure 5-14: Sequential image series showing the vehicle around the pipe, covering each 45° station. Temporal progression runs from left to right, top to bottom.

As the vehicle completed a full 360-degree rotation, the PEC sensor actively measured the pipe's thickness at sections of nominal 6.0 mm, 10.0 mm, and 20.0 mm. Each section was measured three times, requiring the vehicle to make three complete circuits for each thickness measurement, which is shown in Figure 5-14. The median value of these measurements was then used to determine the final thickness for each section. The vehicle completed its path, from starting at the top and returning, in under 75 seconds, with each circuit taking approximately 25 seconds. This allowed for 25 measurement points around the pipe for each circle.

As stated in Section 5.2 data processing methods such as the FFT, Butterworth low-pass filter and Savitzky-Golay Filter were used in order to filter and smooth the signal.

5.4.4 Pulsed Eddy Current with Unmanned Aerial Vehicle for Pipe Inspection Results

The next phase of the experiment involved using the calibrated PEC system mounted on the UAV-crawler hybrid vehicle to inspect a cylindrical pipe. The pipe used in this experiment were stated in Section 5.5.2. Using the calibration block in Section 5.6.1, dynamic PEC thicknesses was mapped by extracting features from each recorded signal.

The radar plot, which depicts the pipe's thickness in relation to the reference pipe thickness, and the error analysis, are presented in Figure 5-15 and Table 5-4, respectively. Upon reviewing the results, a relatively significant signal error was observed at approximately 180° (bottom of pipe) for the nominal 20.0 mm pipe thickness section, with a maximum absolute mean error of 0.412 mm. This error is likely caused by the increased downward forces of gravity and could be attributed to the increased motor speed required to support the vehicle in this position, thereby generating additional Electromagnetic Interference (EMI).

Despite these issues, the prediction of thickness under three different conditions demonstrates good consistency, with the maximum standard deviation error from dynamic tests being 1.070 mm, adequately distinguishing thickness variations around the pipe. The relative errors remain below 5% across all measured conditions, indicating that the margin of error is sufficiently narrow to reliably discern variations in thickness.

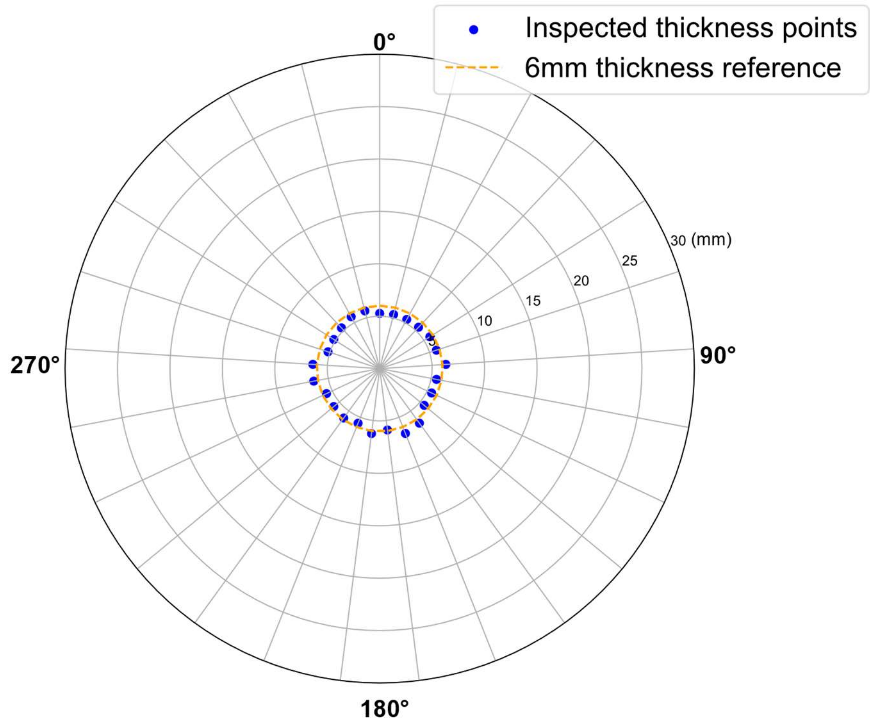

(a)

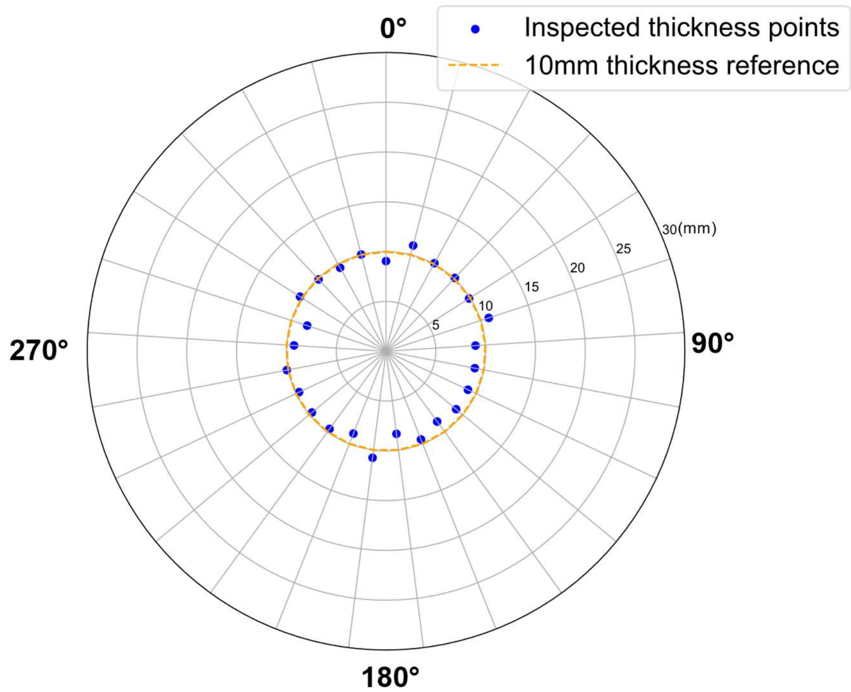

(b)

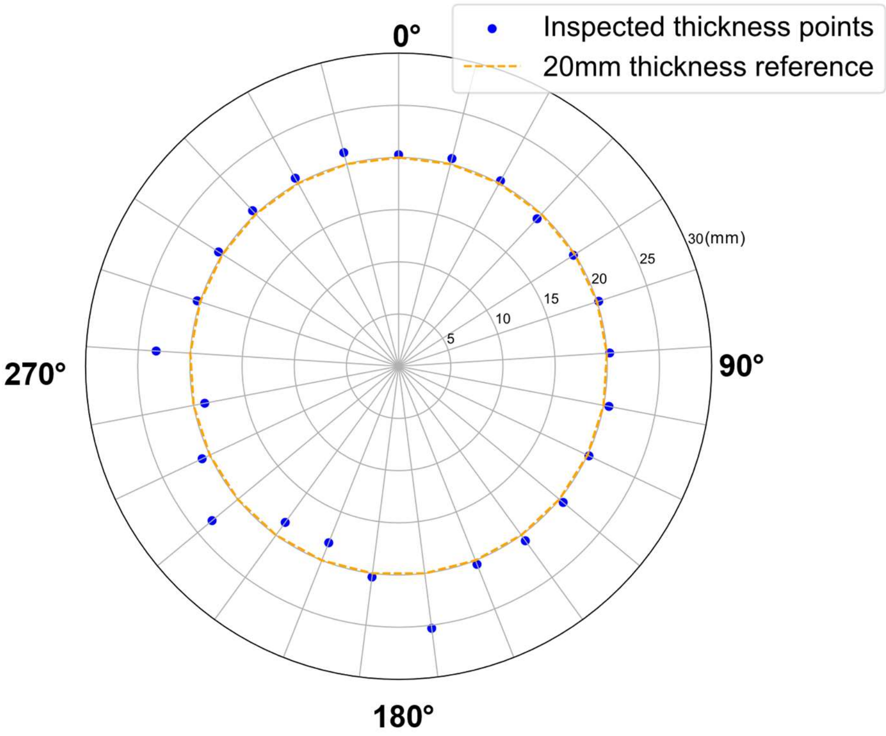

(c)

Figure 5-15: A radar chart comparing measured pipe thicknesses at (a) 6.0 mm, (b) 10.0 mm, and (c) 20.0 mm during the inspection.

Table 5-4: Pipe wall thickness measurement error statics

Pipe reference thickness (mm)	Mean error (mm)	Relative error	Standard deviation (mm)
6.0	-0.269	4.80%	0.433
10.0	-0.294	2.94%	0.707
20.0	0.412	2.08%	1.070

5.5 Conclusion

In conclusion, this chapter first illustrates reviews approaches of different robots for exterior pipe inspection. The novel hybrid UAV-crawler is identified as a novel and highly promising approach to combine the advantages and address the shortcomings of pipe exterior NDE systems. With an embedded PEC system, this UAV-crawler hybrid offers a new solution for examining pipe thickness from the exterior. In this way, costs associated with initial manual deployment could be eliminated, provided there is sufficient airspace clearance. During inspection, the vehicle engages in full-body pipe contact, significantly enhancing stability and disturbance rejection compared to free-flying systems.

This study of this chapter also bridges a crucial gap in NDT for essential infrastructure upkeep, notably in the oil and gas sector. Conventional PEC systems, despite their efficacy in identifying subsurface defects, are generally cumbersome for aerial platform integration, constraining their use for inspection at height, amid hazards, or in locations with otherwise challenging access and necessitating hazardous manual inspection processes.

Our approach introduces a drone-mounted, lightweight dual-coil PEC sensor system, tailored to overcome the challenges of traditional and commercial systems' weight constraints. First, the use of the Butterworth low-pass filter, along with Fourier Transform and Savitzky-Golay smoothing, is proved efficient and useful in mitigating EMI and enhancing signal clarity. This processing pipeline ensured accurate feature extraction and reliable thickness measurements. Then, the application of practical UAV integrations with the PEC system enables comprehensive, non-intrusive inspections of pipeline integrity from all angles, enhancing detection capabilities for wall thinning, with a maximum absolute mean error of 0.412 mm. Besides, this application of PEC and UAV integration to inspect pipeline ensured reliable thickness measurements, with relative errors remaining below 5% across all measured conditions.

Future work should look to optimise system sensitivity and applicability to additional geometries and alloys. Additionally, the system endurance time should be improved to extend inspection durations. Furthermore, efforts should be made to improve the current system's ability to function across large lift-off distances enabling inspection under insulation.

Nevertheless, despite the current limitations, the findings in this chapter underscore the potential of integrating minimised PEC systems with UAV technology. This integration not only enhances the safety and efficiency of pipeline inspections but also sets the stage for future advancements in autonomous NDT applications. The continued development and refinement of this technology promise significant improvements in infrastructure maintenance and safety, highlighting the importance of ongoing research and innovation in this field.

Chapter 6 Conclusions and Future Work

6.1 Conclusions

This thesis describes the challenges encountered by the energy and petrochemical sectors in conducting remote asset inspections and introduces novel innovations and techniques to enhance these processes. It highlights the advantages of remotely deployable inspections, particularly those utilizing UAVs, and examines the measurable PEC inspection capabilities from such platforms.

Chapter 1 has introduced the motivation, research aims and goals of this project. The research presented herein has highlighted the substantial economic contributions of the oil and gas sector to the UK economy, despite the nation's ongoing transition to a renewable low-carbon energy model. It has underscored the vulnerabilities of critical infrastructure to corrosion and other forms of degradation, which necessitate regular, thorough inspections to prevent costly unplanned outages and ensure safe operations. A key focus of this chapter is the advancement of PEC technology and its integration with UAVs for remote inspection purposes. By developing a compact PEC sensor system suitable for deployment on mobile platforms, including UAVs, the research addresses the limitations of traditional PEC systems and enhances the capability to inspect hard-to-reach and hazardous areas.

The research aims and goals outlined, including the development of a compact PEC sensor system and enhanced UAV-deployed inspections, pave the way for more efficient, comprehensive, and safe assessments of critical infrastructure. This innovative approach promises to significantly mitigate the challenges associated with traditional inspection methods, ensuring the continued integrity and reliability of vital energy infrastructure.

In **Chapter 2**, the NDT method, Pulsed Eddy Current technology, robotic NDT particularly aerial NDT have been reviewed an introduced in detail. NDT remains a critical technique for assessing material and structural integrity across various industries without causing damage. Among these methods, PEC technology stands out for its effectiveness in detecting subsurface defects and corrosion in conductive materials, particularly through coatings and insulation. The integration of robotics into NDT processes further enhances inspection efficiency, accuracy, and safety, especially in hazardous environments. Additionally, UAVs have revolutionized NDT by providing flexible, mobile platforms capable of accessing difficult or dangerous areas, thereby reducing the need for scaffolding or rope access. This chapter delves into the advancements in NDT, particularly PEC and UAV-based methods, showcasing their potential to improve inspection capabilities for critical infrastructure.

In **Chapter 3**, an extensive evaluation was performed to characterize the performance of the MAXWELL PEC probe when scanning various thicknesses of BRT 080A15 carbon steels. The study emphasized the impact of minor changes in orientation angles on thickness measurements, simulating conditions akin to those encountered when the probe is mounted on a hybrid-crawler UAV.

Experimental results indicate the PEC probe's performance is contingent on both the thickness and alignment of steel samples. Nominal 20.0 mm thick samples exhibited a marginally higher sensitivity to orientation effects, yet measurement errors remained below 0.5 mm. In contrast, alignment had a minimal impact on thinner samples (6.0 mm), with the maximum error reaching only 1.122 mm. The increased sensitivity of thicker samples is attributed to deeper probe penetration, leading to signal attenuation and spatial errors. Consistently, the probe demonstrated a tendency to overestimate thickness. These findings provide critical insights for optimizing probe deployment and enhancing accuracy in NDT.

These results are pivotal for addressing challenges related to sensor sensitivity and measurement precision, particularly in UAV applications. This research lays a foundation for future advancements in NDT techniques, offering a strategic framework for deploying PEC probes in UAV-based inspections. As industries increasingly adopt automation and robotics for inspection and monitoring, the insights from this study pave the way for improved efficiency, accuracy, and reliability in industrial operations.

In **Chapter 4**, the analytical model for the feature extraction method to calculate material thickness was reviewed. The design, fabrication, and analysis of a PEC sensor system for mobile NDT, specifically for evaluating ferro-magnetic material thickness, were explored. The study focused on enhancing the sensitivity and accuracy of thickness measurements using a dual-coil configuration. Both finite element analysis (FEA) simulations and experimental comparisons were conducted to evaluate the performance of single-coil and dual-coil setups. The dual-coil configuration showed significant improvements in detecting material thickness variations, with higher eddy current density and a more uniform distribution across the sample. The notable increase in the τ difference by a factor of 13.84 with the dual-coil setup demonstrates its superiority in providing comprehensive assessments of the internal structure of steel samples, which is crucial for applications requiring precise pipe thickness measurements.

The investigation included dimension parameters and the lift-off effect on the PEC signal of the dual-coil configuration. The study on lift-off distances revealed that while signal amplitude decreases with increasing lift-off distance, the decay rate feature τ remains minimally affected, highlighting the robustness of the proposed probe design for autonomous aerial NDT applications. Additionally, examining the horizontal distances between receiver coils indicated that smaller distances enhance sensitivity to thickness variations, with a nominal 3.0 mm horizontal distance being optimal for practical implementation due to manufacturing tolerances. The effects of varying vertical excitation-detector coil distances showed that although signal amplitude decreases with greater vertical distances, the sensitivity of the PEC system remains largely unaffected. These findings collectively inform the design parameters for maximizing the accuracy and reliability of the PEC sensor system in aerial NDT applications.

The chapter also detailed the development and implementation of the on-board PEC system, including the PEC probe, signal excitation circuit, and signal reception and processing components. The integrated PEC system was designed for mobility, utilizing a 3D-printed probe frame, high heat-deflection materials, and precise fabrication techniques to ensure structural integrity and functional efficiency. The excitation circuit was optimized to generate precise current pulses, crucial for inducing strong and measurable eddy currents in the test material. The receiver circuit effectively amplified the detected signals, ensuring high-quality data acquisition for accurate material thickness assessments. This comprehensive approach to PEC system design and implementation demonstrated the system's potential for autonomous NDT applications, particularly in mobile and remote inspection scenarios. The robustness and effectiveness of the developed system make it a valuable tool for material thickness evaluation.

Despite encountering some discrepancies between simulated and experimental results, attributed to factors such as material property variations, environmental conditions, and experimental setup limitations, the overall consistency in the trend of results validates the robustness of the proposed methodology and the FEA model. The experimental data consistently exhibited the expected decay patterns, reinforcing the reliability of the PEC system for autonomous NDT applications.

In **Chapter 5**, the review began by examining various robotic approaches for exterior pipe inspection. The novel hybrid UAV-crawler emerged as a highly promising solution, combining the benefits and addressing the limitations of existing pipe exterior NDE systems. Equipped with an embedded PEC system, this hybrid UAV-crawler offers a new method for assessing pipe thickness from the exterior, potentially eliminating costs associated with initial manual deployment, given adequate airspace clearance. During inspections, the vehicle maintains full-body contact with the pipe, significantly enhancing stability and disturbance rejection compared to free-flying systems.

This chapter also addresses a crucial gap in NDT for essential infrastructure maintenance, particularly in the oil and gas sector. While conventional PEC systems effectively identify subsurface defects, they are typically too bulky for integration with aerial platforms, limiting their use for inspections at height, in hazardous environments, or in areas with challenging access, often necessitating dangerous manual inspection processes.

Our approach introduces a drone-mounted, lightweight dual-coil PEC sensor system designed to overcome the weight constraints of traditional and commercial systems. The application of the Butterworth low-pass filter, Fourier Transform, and Savitzky-Golay smoothing effectively mitigates EMI and enhances signal clarity, ensuring accurate feature extraction and reliable thickness measurements. Practical UAV integrations with the PEC system enable comprehensive, non-intrusive inspections of pipeline integrity from all angles, significantly improving detection capabilities for wall thinning, with a maximum absolute mean error of 0.412 mm. The PEC-UAV integration ensures reliable thickness measurements, with relative errors remaining below 5% across all measured conditions.

Summary Conclusion: In summary, this thesis has successfully developed and demonstrated a novel PEC sensor system integrated with UAV technology for the inspection of critical infrastructure in the energy and petrochemical sectors. The innovative approach of deploying compact PEC systems via UAVs has proven effective in overcoming the limitations of traditional inspection methods, particularly in accessing hard-to-reach and hazardous areas. The research findings provide a foundation for future advancements in NDT techniques, paving the way for more efficient, accurate, and safe inspections. This work represents a step forward in the automation of inspection processes, especially in automated PEC field, promising to enhance the integrity and reliability of vital energy infrastructure while reducing operational risks and costs. The insights gained from this study hold the potential contribute to safer and more sustainable practices.

6.2 Future Work

The advancements and findings presented in this thesis pave the way for several future research directions aimed at further enhancing the capabilities and applications of UAV-deployed PEC technologies, particularly in the context of the oil and gas sector. The following areas are identified as key opportunities for future work, to further improve inspection accuracy and the efficiency of airborne PEC NDT inspections:

6.2.1 Industrial PEC Sensor

The controlled laboratory setting with an industrial robotic manipulator does not fully replicate real-world UAV environments. The test samples were uniform, flat carbon steel plates and pipes, not reflecting real-world variability in material properties, surface roughness, and geometry. In addition, environmental factors such as temperature fluctuations and humidity were not explored, which could impact sensor performance. Future research will include field tests with UAVs equipped with PEC sensors in real-world environments. Nonuniform components, such as drawn pipes, can vary in material composition and thickness, affecting probe performance and requiring a broader understanding of probe behaviour. Nonplanar structures, common in industrial settings, also pose challenges for accurate thickness measurement. Investigating these factors will help develop more sophisticated and robust NDT methods for modern industrial applications.

6.2.2 FEA Analysis and Simulation Model

There are some discrepancies between simulated and experimental results of the customised and optimised PEC sensor in Chapter 4, this could be attributed to factors such as material property variations, environmental conditions, and experimental setup limitations. In future, the measured magnetization curve for low carbon steel (B-H loop) should be applied into the FEA analysis using COMSOL software. Besides, temperature fluctuations and humidity should also be controlled or accounted for in the experiments. Moreover, differences in inductance values and wire resistance should be considered and measured in the numerical modelling.

6.2.3 Integration of PEC into UAV-Crawler Vehicle

The probe's operation is currently limited to under two and a half minutes due to the risk of overheating the current PEC probe design. This limitation is a constraint, particularly in environments where extended inspection times are necessary for thorough assessments. To address this issue, a controller panel could be embedded into the excitation circuit to manage pulse generation. This modification would enable more precise control over the heat generated by the coil, thereby mitigating the risk of overheating and extending the operational duration of the PEC system within the aluminium-shielded enclosure. The enclosure serves a dual purpose: protecting the electronics from dust and mechanical impacts, while also attenuating EMI, which improves the reliability of the system.

Furthermore, the operational constraints of the drone are influenced by the battery capacity of the entire vehicle system. The current battery life limits the drone’s ability to complete multiple circuits around the pipe, which has been essential for accurate thickness measurements in the experiments presented in this work. A minimum of three complete passes around the pipe was conducted to ensure comprehensive data collection, allowing signal averaging over multiple runs to enhance measurement reliability.

However, it is acknowledged that reducing the number of passes by slowing the drone's movement during a single pass may offer a more efficient approach. By collecting more data points at a lower speed, the requirement for multiple passes could be mitigated, potentially improving both data resolution and battery efficiency. This alternative strategy, which was not explored in the current research, will be considered as part of future work to optimise the system’s performance and further reduce power consumption during inspection.

Therefore, extending the vehicle's operation time is crucial. This could be achieved by several means: switching from a 3D-printed mechanical flight frame to a carbon fibre one, which would reduce weight and increase durability; increasing the drone's battery capacity to allow for longer flight times; and upgrading the motor to boost propeller thrust, thus enabling the drone to carry a higher payload. These enhancements would not only improve the drone's endurance but also its overall performance and reliability in industrial inspection scenarios.

Future work should also focus on improving the system’s ability to function across large lift-off distances, which is essential for conducting inspections under insulation. The presence of an insulation layer on industrial pipes poses a challenge for traditional inspection methods, as it can interfere with the accuracy of the measurements. By developing a PEC system that can effectively inspect through insulation, the utility of the technology can be expanded. This would involve integrating tuned signal processing technique parameters and enhancing the sensitivity of the sensors to detect variations in material thickness despite the presence of insulating materials.

In addition to these technical improvements, there is also a need for further field testing and validation in real-world industrial environments. Pilot projects in collaboration with industry partners could provide valuable insights into the practical challenges and performance of the enhanced PEC-UAV system. Such initiatives would help in fine-tuning the technology, ensuring it meets industry standards and regulatory requirements.

In conclusion, while significant progress has been made in the development and application of PEC systems for UAV-based inspections, there remain several avenues for future work. By addressing the current limitations and exploring new technological integrations, the effectiveness and applicability of PEC systems in the oil and gas sector can be greatly enhanced, leading to safer and more efficient inspection processes.

In Short, this PhD research has developed and integrated PEC sensor system with a hybrid UAV-crawler to enhance remote inspection of critical infrastructure. The work addresses key challenges in the NDT field of energy and petrochemical sectors, particularly in accessing and inspecting hard-to-reach areas. Through a combination of theoretical analysis and experimental validation, this research contributes to the existing knowledge in PEC and UAV technologies and offers practical solutions for improving inspection methods. The findings provide a solid foundation for future advancements in automated inspection processes, aimed at enhancing the safety and reliability of industrial operations.

References

[1] ‘OGUK-Economic-Report-2021.pdf’. Accessed: Jul. 19, 2024. [Online]. Available: https://oeuk.org.uk/wp-content/uploads/2021/08/OGUK-Economic-Report-2021.pdf

[2] G. M. Team, ‘The Cost of Unplanned Downtime for Refineries’. Accessed: Jul. 19, 2024. [Online]. Available: https://blog.geckorobotics.com/the-cost-of-unplanned-downtime-for-refineries

[3] ‘5 Key Questions About Corrosion in Carbon Capture Processing Plants’. Accessed: Jul. 19, 2024. [Online]. Available: https://m.crimeawalks.com/corrosion-in-carbon-capture-plants/2/6623

[4] ‘API RP 571 | API Standards Store’. Accessed: Jul. 19, 2024. [Online]. Available: https://store.accuristech.com/api/standards/api-rp-571?product_id=2108271

[5] K. CSC (SK), ‘Corrosion under Insulation - CUI matters Safety, Reliability, Reputation’, KAEFER SE & Co. KG. Accessed: Jul. 19, 2024. [Online]. Available: https://kaefer.com/blog/corrosion-under-insulation-cui-matters-safety-reliability-reputation/

[6] Q. Cao *et al.*, ‘A Review of Corrosion under Insulation: A Critical Issue in the Oil and Gas Industry’, *Metals*, vol. 12, no. 4, Art. no. 4, Apr. 2022, doi: 10.3390/met12040561.

[7] nztc, ‘Solving the corrosion under insulation challenge’, Net Zero Technology Centre. Accessed: Jul. 19, 2024. [Online]. Available: https://www.netzerotc.com/news-insights/solving-the-corrosion-under-insulation-challenge/

[8] 'API 570 | API Standards Store'. Accessed: Jul. 19, 2024. [Online]. Available: https://store.accuristech.com/api/standards/api-570?product_id=1910713

[9] M. Z. Ab Rashid, M. F. Mohd Yakub, S. A. Zaki bin Shaikh Salim, N. Mamat, S. M. Syed Mohd Putra, and S. A. Roslan, 'Modeling of the in-pipe inspection robot: A comprehensive review', *Ocean Engineering*, vol. 203, p. 107206, May 2020, doi: 10.1016/j.oceaneng.2020.107206.

[10] A. Shukla and H. Karki, 'Application of robotics in onshore oil and gas industry—A review Part I', *Robotics and Autonomous Systems*, vol. 75, pp. 490–507, Jan. 2016, doi: 10.1016/j.robot.2015.09.012.

[11] LuminUltra, 'Understanding microbiologically influenced corrosion (MIC): what you need to know', LuminUltra. Accessed: Jul. 19, 2024. [Online]. Available: https://www.luminultra.com/blog/understanding-microbiologically-influenced-corrosion/

[12] International Atomic Energy Agency, 'Non-destructive testing: A guidebook for industrial management and quality control personnel', International Atomic Energy Agency (IAEA), 1999.

[13] A. Sophian, G. Tian, and M. Fan, 'Pulsed Eddy Current Non-destructive Testing and Evaluation: A Review', *Chin. J. Mech. Eng.*, vol. 30, no. 3, Art. no. 3, May 2017, doi: 10.1007/s10033-017-0122-4.

[14] F. Nafiah, M. O. Tokhi, G. Shirkoohi, F. Duan, Z. Zhao, and O. Rees-Lloyd, 'Decoupling the Influence of Wall Thinning and Cladding Thickness Variations in Pulsed Eddy Current Using Principal Component Analysis', *IEEE Sensors J.*, vol. 21, no. 19, pp. 22011–22018, Oct. 2021, doi: 10.1109/JSEN.2021.3100648.

[15] F. Nafiah *et al.*, 'Parameter Analysis of Pulsed Eddy Current Sensor Using Principal Component Analysis', *IEEE Sensors Journal*, vol. 21, no. 5, pp. 6897–6903, Mar. 2021, doi: 10.1109/JSEN.2020.3036967.

[16] C. Huang, X. Wu, Z. Xu, and Y. Kang, 'Ferromagnetic material pulsed eddy current testing signal modeling by equivalent multiple-coil-coupling approach', *NDT & E International*, vol. 44, no. 2, pp. 163–168, Mar. 2011, doi: 10.1016/j.ndteint.2010.11.001.

[17] D. Vasic, V. Bilas, and D. Ambrus, 'Pulsed eddy-current nondestructive testing of ferromagnetic tubes', *IEEE Transactions on Instrumentation and Measurement*, vol. 53, no. 4, Art. no. 4, Aug. 2004, doi: 10.1109/TIM.2004.830594.

[18] Applus+, 'Riser Inspection and Caisson Inspection', https://www.applus.com. Accessed: Jul. 19, 2024. [Online]. Available: https://www.applus.com/uk/en/what-we-do/service-sheet/riser-inspection-and-caisson-inspection

[19] 'NDE 4.0—NDE for the 21st Century—The Internet of Things and Cyber Physical Systems will Revolutionize NDE'. Accessed: Jul. 19, 2024. [Online]. Available: https://dr.lib.iastate.edu/entities/publication/79f0af53-7287-40db-b1d6-d6f95e6d2fc9

[20] 'Human factors and ergonomics - HSE'. Accessed: Jul. 19, 2024. [Online]. Available: https://www.hse.gov.uk/humanfactors/index.htm

[21] P. Nooralishahi *et al.*, 'Drone-Based Non-Destructive Inspection of Industrial Sites: A Review and Case Studies', *Drones*, vol. 5, no. 4, Art. no. 4, Dec. 2021, doi: 10.3390/drones5040106.

[22] L. Wang, Z. Zhang, and X. Luo, ‘A Two-Stage Data-Driven Approach for Image-Based Wind Turbine Blade Crack Inspections’, *IEEE/ASME Transactions on Mechatronics*, vol. 24, no. 3, pp. 1271–1281, Jun. 2019, doi: 10.1109/TMECH.2019.2908233.

[23] P. Buchan, 'How Drones Are Being Used for Inspection in Industrial Environments,' *Multicopters for Inspection*, July 2018. [Online]. Available: https://www.bindt.org/admin/Downloads/Multicopters%20for%20Inspection%20-%2005%20Buchan%20-%20July%2018%20V1.1.pdf. Accessed: Aug. 9, 2024.

[24] X. Li, Q. Yang, Z. Chen, X. Luo, and W. Yan, ‘Visible defects detection based on UAV-based inspection in large-scale photovoltaic systems’, *IET Renewable Power Generation*, vol. 11, no. 10, pp. 1234–1244, 2017, doi: 10.1049/iet-rpg.2017.0001.

[25] O. Menéndez, M. Pérez, and F. Auat Cheein, ‘Visual-Based Positioning of Aerial Maintenance Platforms on Overhead Transmission Lines’, *Applied Sciences*, vol. 9, no. 1, Art. no. 1, Jan. 2019, doi: 10.3390/app9010165.

[26] J. Seo, L. Duque, and J. Wacker, ‘Drone-enabled bridge inspection methodology and application’, *Automation in Construction*, vol. 94, pp. 112–126, Oct. 2018, doi: 10.1016/j.autcon.2018.06.006.

[27] ‘Pioneering Unmanned Inspection of North Sea FPSO Cargo Tank - TEXO’. Accessed: Jul. 19, 2024. [Online]. Available: https://texo.co.uk/case-studies/pioneering-unmanned-inspection-of-north-sea-fpso-cargo-tank/

[28] C. J. Hellier, *Handbook of Nondestructive Evaluation*, 3rd ed. New York: McGraw-Hill, 2020.

[29] D. Zhang, R. Watson, C. MacLeod, G. Dobie, W. Galbraith, and G. Pierce, 'Implementation and evaluation of an autonomous airborne ultrasound inspection system', *Nondestructive Testing and Evaluation*, vol. 37, no. 1, pp. 1–21, Jan. 2022, doi: 10.1080/10589759.2021.1889546.

[30] P. B. Quater, F. Grimaccia, S. Leva, M. Mussetta, and M. Aghaei, 'Light Unmanned Aerial Vehicles (UAVs) for Cooperative Inspection of PV Plants', *IEEE Journal of Photovoltaics*, vol. 4, no. 4, pp. 1107–1113, Jul. 2014, doi: 10.1109/JPHOTOV.2014.2323714.

[31] 'Nace-International-Report.pdf'. Accessed: Jul. 19, 2024. [Online]. Available: http://impact.nace.org/documents/Nace-International-Report.pdf

[32] T. Chen, G. Y. Tian, A. Sophian, and P. W. Que, 'Feature extraction and selection for defect classification of pulsed eddy current NDT', *NDT & E International*, vol. 41, no. 6, Art. no. 6, Sep. 2008, doi: 10.1016/j.ndteint.2008.02.002.

[33] I. Z. Abidin, C. Mandache, G. Y. Tian, and M. Morozov, 'Pulsed eddy current testing with variable duty cycle on rivet joints', *NDT & E International*, vol. 42, no. 7, pp. 599–605, Oct. 2009, doi: 10.1016/j.ndteint.2009.04.001.

[34] M. Alamin, G. Y. Tian, A. Andrews, and P. Jackson, 'Principal Component Analysis of Pulsed Eddy Current Response From Corrosion in Mild Steel', *IEEE Sensors Journal*, vol. 12, no. 8, Art. no. 8, Aug. 2012, doi: 10.1109/JSEN.2012.2195308.

[35] C. Mineo, S. G. Pierce, P. I. Nicholson, and I. Cooper, 'Robotic path planning for non-destructive testing – A custom MATLAB toolbox approach', *Robotics*

and Computer-Integrated Manufacturing, vol. 37, pp. 1–12, Feb. 2016, doi: 10.1016/j.rcim.2015.05.003.

[36] Y. Javadi *et al.*, 'Ultrasonic phased array inspection of a Wire + Arc Additive Manufactured (WAAM) sample with intentionally embedded defects', *Additive Manufacturing*, vol. 29, p. 100806, Oct. 2019, doi: 10.1016/j.addma.2019.100806.

[37] G. Dobie, R. Summan, C. MacLeod, G. Pierce, and W. Galbraith, 'An automated miniature robotic vehicle inspection system', *AIP Conference Proceedings*, vol. 1581, no. 1, pp. 1881–1888, Feb. 2014, doi: 10.1063/1.4865053.

[38] C. Deneke, C. Schlösser, S. Mehler, and T. Schüppstuhl, 'Positioning NDT Sensors with a Mobile Robot for Efficient Aircraft Inspections', *e-Journal of Nondestructive Testing*, vol. 21, no. 04, Apr. 2016, Accessed: Jul. 19, 2024. [Online]. Available: https://www.ndt.net/search/docs.php3?id=18922&msgID=0&rootID=0

[39] R. Q. Ismael and Q. Z. Henari, 'Accuracy Assessment of UAV photogrammetry for Large Scale Topographic Mapping', in *2019 International Engineering Conference (IEC)*, Jun. 2019, pp. 1–5. doi: 10.1109/IEC47844.2019.8950607.

[40] B. Abad, D.-A. Borca-Tasciuc, and M. S. Martin-Gonzalez, 'Non-contact methods for thermal properties measurement', *Renewable and Sustainable Energy Reviews*, vol. 76, pp. 1348–1370, Sep. 2017, doi: 10.1016/j.rser.2017.03.027.

[41] D. Zhang, R. Watson, G. Dobie, C. MacLeod, and G. Pierce, ‘Autonomous Ultrasonic Inspection Using Unmanned Aerial Vehicle’, in *2018 IEEE International Ultrasonics Symposium (IUS)*, Oct. 2018, pp. 1–4. doi: 10.1109/ULTSYM.2018.8579727.

[42] R. Watson *et al.*, ‘Dry Coupled Ultrasonic Non-Destructive Evaluation Using an Over-Actuated Unmanned Aerial Vehicle’, *IEEE Transactions on Automation Science and Engineering*, vol. 19, no. 4, pp. 2874–2889, Oct. 2022, doi: 10.1109/TASE.2021.3094966.

[43] Y. Yu, Y. Yan, F. Wang, G. Tian, and D. Zhang, ‘An approach to reduce lift-off noise in pulsed eddy current nondestructive technology’, *NDT & E International*, vol. 63, pp. 1–6, Apr. 2014, doi: 10.1016/j.ndteint.2013.12.012.

[44] P. Crouzen and I. Munns, ‘Pulsed Eddy Current Corrosion Monitoring in Refineries and Oil Production Facilities–Experience at Shell’, *signal*, vol. 2, no. 3, Art. no. 3, 2006.

[45] J. García-Martín, J. Gómez-Gil, and E. Vázquez-Sánchez, ‘Non-Destructive Techniques Based on Eddy Current Testing’, *Sensors*, vol. 11, no. 3, Art. no. 3, Feb. 2011, doi: 10.3390/s110302525.

[46] 14:00-17:00, ‘ISO 20669:2017’, ISO. Accessed: Jul. 19, 2024. [Online]. Available: https://www.iso.org/standard/68784.html

[47] M. Michniakova and L. Janousek, ‘The impact of various waveform shapes on the response signal in pulsed eddy current NDE’, in *2012 ELEKTRO*, May 2012, pp. 439–442. doi: 10.1109/ELEKTRO.2012.6225661.

[48] Y. Li, B. Yan, D. Li, H. Jing, Y. Li, and Z. Chen, ‘Pulse-modulation eddy current inspection of subsurface corrosion in conductive structures’, *NDT & E*

International, vol. 79, pp. 142–149, Apr. 2016, doi: 10.1016/j.ndteint.2016.02.001.

[49] J. Li, X. Wu, Q. Zhang, and P. Sun, ‘Measurement of lift-off using the relative variation of magnetic flux in pulsed eddy current testing’, *NDT & E International*, vol. 75, pp. 57–64, Oct. 2015, doi: 10.1016/j.ndteint.2015.06.008.

[50] D. Desjardins, T. W. Krause, and L. Clapham, ‘Transient eddy current method for the characterization of magnetic permeability and conductivity’, *NDT & E International*, vol. 80, pp. 65–70, Jun. 2016, doi: 10.1016/j.ndteint.2016.02.010.

[51] Y. He *et al.*, ‘Pulsed eddy current technique for defect detection in aircraft riveted structures’, *NDT & E International*, vol. 43, no. 2, Art. no. 2, Mar. 2010, doi: 10.1016/j.ndteint.2009.10.010.

[52] C. Huang, ‘Pulsed eddy current signal processing method for signal denoising in ferromagnetic plate testing’, p. 6, 2010.

[53] C. Huang and X. Wu, ‘An improved ferromagnetic material pulsed eddy current testing signal processing method based on numerical cumulative integration’, *NDT & E International*, vol. 69, pp. 35–39, Jan. 2015, doi: 10.1016/j.ndteint.2014.09.006.

[54] N. Ulapane, A. Alempijevic, T. Vidal-Calleja, J. V. Miro, J. Rudd, and M. Roubal, ‘Gaussian process for interpreting pulsed eddy current signals for ferromagnetic pipe profiling’, in *2014 9th IEEE Conference on Industrial Electronics and Applications*, Hangzhou, China: IEEE, Jun. 2014, pp. 1762–1767. doi: 10.1109/ICIEA.2014.6931453.

[55] Z. Xu, X. Wu, J. Li, and Y. Kang, ‘Assessment of wall thinning in insulated ferromagnetic pipes using the time-to-peak of differential pulsed eddy-current

testing signals’, *NDT & E International*, vol. 51, pp. 24–29, Oct. 2012, doi: 10.1016/j.ndteint.2012.07.004.

[56] F. Nafiah, M. O. Tokhi, S. Majidnia, J. Rudlin, Z. Zhao, and F. Duan, ‘Pulsed Eddy Current: Feature Extraction Enabling In-Situ Calibration and Improved Estimation for Ferromagnetic Application’, *J Nondestruct Eval*, vol. 39, no. 3, p. 52, Sep. 2020, doi: 10.1007/s10921-020-00699-w.

[57] C. Huang, W. Xinjun, X. Zhiyuan, and Y. Kang, ‘Pulsed eddy current signal processing method for signal denoising in ferromagnetic plate testing’, *NDT & E International*, vol. 43, no. 7, Art. no. 7, Oct. 2010, doi: 10.1016/j.ndteint.2010.06.010.

[58] X. Chen and Y. Lei, ‘Excitation current waveform for eddy current testing on the thickness of ferromagnetic plates’, *NDT & E International*, vol. 66, pp. 28–33, Sep. 2014, doi: 10.1016/j.ndteint.2014.04.006.

[59] S. Yan and X. Chen, ‘Time-domain analytical solutions to pulsed eddy current model of moving cylindrical conductor’, *NDT & E International*, vol. 137, p. 102863, Jul. 2023, doi: 10.1016/j.ndteint.2023.102863.

[60] V. O. de Haan and P. de Jong, 'Simultaneous Measurement of Material Properties and Thickness of Carbon Steel Plates Using Pulsed Eddy Currents,' in *16th World Conference on NDT*, Montreal, Canada, 2004. [Online]. Available: https://www.ndt.net/article/wcndt2004/pdf/eddy_current/42_haan.pdf. Accessed: Aug. 9, 2024.

[61] S. Tumanski, ‘Induction coil sensors—a review’, *Meas. Sci. Technol.*, vol. 18, no. 3, p. R31, Jan. 2007, doi: 10.1088/0957-0233/18/3/R01.

[62] X. Chen and Y. Lei, ‘Time-domain analytical solutions to pulsed eddy current field excited by a probe coil outside a conducting ferromagnetic pipe’, *NDT & E International*, vol. 68, pp. 22–27, Dec. 2014, doi: 10.1016/j.ndteint.2014.07.005.

[63] N. Ulapane and L. Nguyen, ‘Review of Pulsed-Eddy-Current Signal Feature-Extraction Methods for Conductive Ferromagnetic Material-Thickness Quantification’, *Electronics*, vol. 8, no. 5, p. 470, Apr. 2019, doi: 10.3390/electronics8050470.

[64] N. Ulapane, A. Alempijevic, T. Vidal Calleja, and J. Valls Miro, ‘Pulsed Eddy Current Sensing for Critical Pipe Condition Assessment’, *Sensors*, vol. 17, no. 10, Art. no. 10, Oct. 2017, doi: 10.3390/s17102208.

[65] N. Ulapane, K. Thiyagarajan, J. V. Miro, and S. Kodagoda, ‘Surface Representation of Pulsed Eddy Current Sensor Signals for Improved Ferromagnetic Material Thickness Quantification’, *IEEE Sensors J.*, vol. 21, no. 4, pp. 5413–5422, Feb. 2021, doi: 10.1109/JSEN.2020.3034571.

[66] ‘Quantum Design North America - Products - Physical Property Measurement System – Quantum Design PPMS®’. Accessed: Jul. 19, 2024. [Online]. Available: https://www.qdusa.com/products/ppms.html

[67] W. Cheng, ‘Pulsed Eddy Current Testing of Carbon Steel Pipes’ Wall-thinning Through Insulation and Cladding’, *J Nondestruct Eval*, vol. 31, no. 3, pp. 215–224, Sep. 2012, doi: 10.1007/s10921-012-0137-9.

[68] D. G. Park, C. S. Angani, G. D. Kim, C. G. Kim, and Y. M. Cheong, ‘Evaluation of Pulsed Eddy Current Response and Detection of the Thickness Variation in the Stainless Steel’, *IEEE Transactions on Magnetics*, vol. 45, no. 10, Art. no. 10, Oct. 2009, doi: 10.1109/TMAG.2009.2024219.

[69] 'Flaw Detection And Quantification For Ferromagnetic Steels Using Pulsed Eddy Current Techniques And Magnetization', Accessed: Jul. 19, 2024. [Online]. Available: https://www.witpress.com/elibrary/wit-transactions-on-engineering-sciences/44/13946

[70] G. Singh, H. M. Bapat, B. P. Singh, M. Bandyopadhyay, R. K. Puri, and D. N. Badodkar, 'Thickness Evaluation of Aluminium Plate Using Pulsed Eddy Current Technique', *J. Inst. Eng. India Ser. D*, vol. 94, no. 2, Art. no. 2, Oct. 2013, doi: 10.1007/s40033-013-0028-y.

[71] 'Operational Amplifiers: Theory and Design | SpringerLink'. Accessed: Jul. 19, 2024. [Online]. Available: https://link.springer.com/book/10.1007/978-3-319-28127-8

[72] *Filter Handbook A Practical Design*. Accessed: Jul. 19, 2024. [Online]. Available: http://archive.org/details/FilterHandbookAPracticalDesign

[73] A. Sophian, 'Characterisation of surface and sub-surface discontinuities in metals using pulsed eddy current sensors', doctoral, University of Huddersfield, 2003. Accessed: Jul. 19, 2024. [Online]. Available: https://www.hud.ac.uk/news/

[74] C. Kitchin and L. Counts, 'A Designer's Guide to Instrumentation Amplifiers', 3rd ed. Norwood, MA: Analog Devices, Inc., 2006. [Online]. Available: https://www.analog.com/media/en/training-seminars/design-handbooks/designers-guide-instrument-amps-complete.pdf. Accessed: Aug. 9, 2024.

[75] M. D. Lutovac, D. V. Tošić, and B. L. Evans, *Filter Design for Signal Processing Using MATLAB and Mathematica*. Miroslav Lutovac, 2001.

[76] 'continuous-time-active-filter-design.pdf'. Accessed: Jul. 19, 2024. [Online]. Available: https://gctjaipur.wordpress.com/wp-content/uploads/2015/08/continuous-time-active-filter-design.pdf

[77] G. Y. Tian, Y. Li, and C. Mandache, 'Study of Lift-Off Invariance for Pulsed Eddy-Current Signals', *IEEE Transactions on Magnetics*, vol. 45, no. 1, Art. no. 1, Jan. 2009, doi: 10.1109/TMAG.2008.2006246.

[78] C. S. Angani, D. G. Park, G. D. Kim, C. G. Kim, and Y. M. Cheong, 'Differential pulsed eddy current sensor for the detection of wall thinning in an insulated stainless steel pipe', *Journal of Applied Physics*, vol. 107, no. 9, p. 09E720, May 2010, doi: 10.1063/1.3337725.

[79] Y. He, M. Pan, F. Luo, and G. Tian, 'Pulsed eddy current imaging and frequency spectrum analysis for hidden defect nondestructive testing and evaluation', *NDT & E International*, vol. 44, no. 4, Art. no. 4, Jul. 2011, doi: 10.1016/j.ndteint.2011.01.009.

[80] A. Sophian, G. Y. Tian, D. Taylor, and J. Rudlin, 'A feature extraction technique based on principal component analysis for pulsed Eddy current NDT', *NDT & E International*, vol. 36, no. 1, pp. 37–41, Jan. 2003, doi: 10.1016/S0963-8695(02)00069-5.

[81] G. Y. Tian, A. Sophian, D. Taylor, and J. Rudlin, 'Multiple sensors on pulsed eddy-current detection for 3-D subsurface crack assessment', *IEEE Sensors Journal*, vol. 5, no. 1, Art. no. 1, Feb. 2005, doi: 10.1109/JSEN.2004.839129.

[82] D. Chen, Q. Ji, H. Zhang, and L. Zhao, 'Application of pulsed eddy current in plate thickness evaluation', in *2009 4th IEEE Conference on Industrial*

Electronics and Applications, May 2009, pp. 3286–3288. doi: 10.1109/ICIEA.2009.5138810.

[83] Y. Li, G. Y. Tian, and A. Simm, ‘Fast analytical modelling for pulsed eddy current evaluation’, *NDT & E International*, vol. 41, no. 6, pp. 477–483, Sep. 2008, doi: 10.1016/j.ndteint.2008.02.001.

[84] N. Ulapane, A. Alempijevic, J. Valls Miro, and T. Vidal-Calleja, ‘Non-destructive evaluation of ferromagnetic material thickness using Pulsed Eddy Current sensor detector coil voltage decay rate’, *NDT & E International*, vol. 100, pp. 108–114, Dec. 2018, doi: 10.1016/j.ndteint.2018.08.003.

[85] Applus+, ‘INCOTEST: Corrosion Under Insulation Inspection Tool’, https://www.applus.com. Accessed: Jul. 19, 2024. [Online]. Available: https://www.applus.com/uk/en/what-we-do/sub-service-sheet/incotest-corrosion-under-insulation-inspection-tool

[86] B. Brown, M. Dixon, M. Morozov, G. Dobie, and A. Gachagan, ‘Assessment of Corrosion under Insulation and Engineered Temporary Wraps using Pulsed Eddy-Current Techniques’, *e-Journal of Nondestructive Testing*, vol. 23, no. 08, Aug. 2018, Accessed: Jul. 19, 2024. [Online]. Available: https://www.ndt.net/search/docs.php3?id=22797&msgID=0&rootID=0

[87] ‘Lyft – Corrosion Under Insulation Inspection Equipment | Eddyfi’. Accessed: Jul. 19, 2024. [Online]. Available: https://www.eddyfi.com/en/product/lyft

[88] R. Bogue, ‘The role of robotics in non-destructive testing’, *Industrial Robot: An International Journal*, vol. 37, no. 5, pp. 421–426, Jan. 2010, doi: 10.1108/01439911011063236.

[89] N. S. Roslin, A. Anuar, M. F. A. Jalal, and K. S. M. Sahari, ‘A Review: Hybrid Locomotion of In-pipe Inspection Robot’, *Procedia Engineering*, vol. 41, pp. 1456–1462, Jan. 2012, doi: 10.1016/j.proeng.2012.07.335.

[90] C. Mineo *et al.*, ‘Interfacing Toolbox for Robotic Arms with Real-Time Adaptive Behavior Capabilities’. Accessed: Jul. 20, 2024. [Online]. Available: https://doi.org/10.17868/70008

[91] C. Mineo *et al.*, ‘Flexible integration of robotics, ultrasonics and metrology for the inspection of aerospace components’, *AIP Conference Proceedings*, vol. 1806, no. 1, p. 020026, Feb. 2017, doi: 10.1063/1.4974567.

[92] Anonymous, ‘Dynamic pulsed eddy current inline inspection technology assesses unpiggable pipelines APRIL 2015’, *Materials Performance; Houston*, vol. 54, no. 4, pp. 14–16, Apr. 2015.

[93] ‘Non-Destructive Testing – IFF GmbH’. Accessed: Jul. 20, 2024. [Online]. Available: https://www.iff-gmbh.de/en/complete-solutions/non-destructive-testing/

[94] T. P. Sattar, H. Leon Rodriguez, and B. Bridge, ‘Climbing ring robot for inspection of offshore wind turbines’, *Industrial Robot*, vol. 36, no. 4, pp. 326–330, Jun. 2009, doi: 10.1108/01439910910957075.

[95] C. N. MacLeod, "Considerations for Automated NDE Applications," Ph.D. dissertation, Dept. of Electronic and Electrical Engineering, Univ. of Strathclyde, Glasgow, U.K., p. 448, 2014.

[96] D. Zhang, K. C. Burnham, L. McDonald, C. N. MacLeod, G. Dobie, R. Summan, and S. Pierce, "Remote inspection of wind turbine blades using UAV with photogrammetry payload," in *Proc. 56th Annual British Conf. Non-*

Destructive Testing (NDT 2017), Telford, U.K., 2017. [Online]. Available: https://strathprints.strath.ac.uk/63321/1/Zhang_etal_NDT_2017_Remote_inspection_of_wind_turbine_blades_using_UAV_with_photogrammetry_payload.pdf. Accessed: Aug. 9, 2024.

[97] M. Han, H. Wang, G. Wang, and Y. Liu, 'TARGETS MASK U-NET FOR WIND TURBINES DETECTION IN REMOTE SENSING IMAGES', *The International Archives of the Photogrammetry, Remote Sensing and Spatial Information Sciences*, vol. XLII–3, pp. 475–480, Apr. 2018, doi: 10.5194/isprs-archives-XLII-3-475-2018.

[98] M. Nieuwenhuisen, J. Quenzel, M. Beul, D. Droeschel, S. Houben, and S. Behnke, 'ChimneySpector: Autonomous MAV-based indoor chimney inspection employing 3D laser localization and textured surface reconstruction', in *2017 International Conference on Unmanned Aircraft Systems (ICUAS)*, Jun. 2017, pp. 278–285. doi: 10.1109/ICUAS.2017.7991427.

[99] R. Watson *et al.*, 'TECHNIQUES FOR CONTACT-BASED STRUCTURAL HEALTH MONITORING WITH MULTIROTOR UNMANNED AERIAL VEHICLES', in *Proceedings of the 13th International Workshop on Structural Health Monitoring*, Destech Publications, Inc., Mar. 2022. doi: 10.12783/shm2021/36236.

[100] R. Watson, "Unmanned Aerial Vehicles for Contact-Based Inspection," Ph.D. dissertation, Dept. of Engineering, Univ. of Strathclyde, Glasgow, UK, 2023. [Online]. Available: https://stax.strath.ac.uk/concern/theses/g732d945t

[101] M. Itani, A. Haroun, and W. Fahs, 'Obstacle Avoidance for Ultrasonic Unmanned Aerial Vehicle Monitoring Using Android Application', in *2018*

International Arab Conference on Information Technology (ACIT), Nov. 2018, pp. 1–4. doi: 10.1109/ACIT.2018.8672681.

[102] K. Niwa, K. Watanabe, and I. Nagai, ‘A detection method using ultrasonic sensors for avoiding a wall collision of Quadrotors’, in *2017 IEEE International Conference on Mechatronics and Automation (ICMA)*, Aug. 2017, pp. 1438–1443. doi: 10.1109/ICMA.2017.8016028.

[103] M. P. Jarzebski *et al.*, ‘Ageing and population shrinking: implications for sustainability in the urban century’, *npj Urban Sustain*, vol. 1, no. 1, pp. 1–11, May 2021, doi: 10.1038/s42949-021-00023-z.

[104] G. Dobie, R. Summan, S. G. Pierce, W. Galbraith, and G. Hayward, ‘A noncontact ultrasonic platform for structural inspection’, *IEEE Sensors Journal*, vol. 11, no. 10, Art. no. 10, 2011.

[105] R. Summan, S. Pierce, G. Dobie, J. Hensman, and C. MacLeod, ‘Practical constraints on real time Bayesian filtering for NDE applications’, *Mechanical Systems and Signal Processing*, vol. 42, no. 1, pp. 181–193, Jan. 2014, doi: 10.1016/j.ymssp.2013.08.008.

[106] C. N. Macleod, S. G. Pierce, J. C. Sullivan, A. G. Pipe, G. Dobie, and R. Summan, ‘Active Whisking-Based Remotely Deployable NDE Sensor’, *IEEE Sensors J.*, vol. 13, no. 11, pp. 4320–4328, Nov. 2013, doi: 10.1109/JSEN.2013.2267813.

[107] ‘9th European Conference on NDT - September 2006 - Berlin (Germany) Proceedings’. Accessed: Jul. 22, 2024. [Online]. Available: https://www.ndt.net/search/docs.php3?id=0&msgID=0&rootID=0

[108] X.-L. Chen and Y.-Z. Lei, ‘Inverse problem of pulsed eddy current field of ferromagnetic plates*’, *Chinese Phys. B*, vol. 24, no. 3, p. 030301, Mar. 2015, doi: 10.1088/1674-1056/24/3/030301.

[109] ‘MAXWELL NDT | New PECT instrument’. Accessed: Jun. 05, 2024. [Online]. Available: https://www.maxwellndt.com/

[110] ‘KR AGILUS’, KUKA AG. Accessed: Jul. 22, 2024. [Online]. Available: https://www.kuka.com/en-gb/products/robotics-systems/industrial-robots/kr-agilus

[111] ‘Convex Optimization – Boyd and Vandenberghe’. Accessed: Jul. 23, 2024. [Online]. Available: https://stanford.edu/~boyd/cvxbook/

[112] ‘ARTECH HOUSE U.K.: Computational Electrodynamics, Third Edition’. Accessed: Jul. 23, 2024. [Online]. Available: https://uk.artechhouse.com/Computational-Electrodynamics-Third-Edition-P1916.aspx

[113] D. J. Griffiths, *Introduction to electrodynamics*, Fourth edition. Boston: Pearson, 2013.

[114] C. A. Sawicki, ‘A dynamic demonstration of Lenz’s law’, *The Physics Teacher*, vol. 35, no. 1, pp. 47–49, Jan. 1997, doi: 10.1119/1.2344590.

[115] R. Pillsbury, ‘A three dimensional eddy current formulation using two potentials: The magnetic vector potential and total magnetic scalar potential’, *IEEE Transactions on Magnetics*, vol. 19, no. 6, pp. 2284–2287, Nov. 1983, doi: 10.1109/TMAG.1983.1062819.

[116] O. Biro, K. Preis, G. Buchgraber, and I. Ticar, ‘Voltage-driven coils in finite-element formulations using a current vector and a magnetic scalar potential’,

IEEE Transactions on Magnetics, vol. 40, no. 2, pp. 1286–1289, Mar. 2004, doi: 10.1109/TMAG.2004.825428.

[117] J.-M. Jin, *The Finite Element Method in Electromagnetics*. John Wiley & Sons, 2015.

[118] O. Biro and K. Preis, ‘On the use of the magnetic vector potential in the finite-element analysis of three-dimensional eddy currents’, *IEEE Transactions on Magnetics*, vol. 25, no. 4, pp. 3145–3159, Jul. 1989, doi: 10.1109/20.34388.

[119] H. Tsuboi, N. Seshima, I. Sebestyen, J. Pavo, S. Gyimothy, and A. Gasparics, ‘Transient eddy current analysis of pulsed eddy current testing by finite element method’, *IEEE Transactions on Magnetics*, vol. 40, no. 2, Art. no. 2, Mar. 2004, doi: 10.1109/TMAG.2004.825009.

[120] ‘Finite Element Analysis (Wiley Series in Computational Mechanics): Amazon.co.uk: Szabó, Barna, Babu□ka, Ivo: 9780471502739: Books’. Accessed: Jul. 23, 2024. [Online]. Available: https://www.amazon.co.uk/Finite-Element-Analysis-Computational-Mechanics/dp/0471502731

[121] M. V. K. Chari, ‘Finite-Element Solution of the Eddy-Current Problem in Magnetic Structures’, *IEEE Transactions on Power Apparatus and Systems*, vol. PAS-93, no. 1, pp. 62–72, Jan. 1974, doi: 10.1109/TPAS.1974.293916.

[122] V. K. Babbar, P. P. Whalen, and T. W. Krause, ‘Pulsed Eddy Current Probe Development to Detect Inner Layer Cracks near Ferrous Fasteners Using COMSOL Modeling Software’, p. 6, 2012.

[123] R. W. Pryor, *Multiphysics Modeling Using COMSOL®: A First Principles Approach*. Jones & Bartlett Publishers, 2009.

[124] 'COMSOL: Multiphysics Software for Optimizing Designs', COMSOL. Accessed: Jul. 23, 2024. [Online]. Available: https://www.comsol.com/

[125] S. Moaveni, *Finite Element Analysis: Theory and Application with ANSYS*, 4th edition. Boston: Pearson, 2014.

[126] F. Vacher, F. Alves, and C. Gilles-Pascaud, 'Eddy current nondestructive testing with giant magneto-impedance sensor', *NDT & E International*, vol. 40, no. 6, pp. 439–442, Sep. 2007, doi: 10.1016/j.ndteint.2007.02.002.

[127] I. D. Adewale and G. Y. Tian, 'Decoupling the Influence of Permeability and Conductivity in Pulsed Eddy-Current Measurements', *IEEE Transactions on Magnetics*, vol. 49, no. 3, Art. no. 3, Mar. 2013, doi: 10.1109/TMAG.2012.2225634.

[128] 'PC-like Ceramic-like (Advanced HighTemp PerFORM)'. Accessed: Jul. 23, 2024. [Online]. Available: https://www.protolabs.com/services/3d-printing/plastic/polycarbonate/perform/

[129] P. Chatzakos, Y. P. Markopoulos, K. Hrissagis, and A. Khalid, 'On the Development of a Modular External-pipe Crawling Omni-directional Mobile Robot', in *Climbing and Walking Robots*, M. O. Tokhi, G. S. Virk, and M. A. Hossain, Eds., Berlin, Heidelberg: Springer, 2006, pp. 693–700. doi: 10.1007/3-540-26415-9_83.

[130] C. Choi, B. Park, and S. Jung, 'The Design and Analysis of a Feeder Pipe Inspection Robot With an Automatic Pipe Tracking System', *IEEE/ASME Transactions on Mechatronics*, vol. 15, no. 5, pp. 736–745, Oct. 2010, doi: 10.1109/TMECH.2009.2032541.

[131] R. Jarvis, A. Farinha, M. Kovac, and F. Cegla, ‘NDE sensor delivery using unmanned aerial vehicles’, *insight*, vol. 60, no. 8, pp. 463–467, Aug. 2018, doi: 10.1784/insi.2018.60.8.463.

[132] C. Paz, E. Suárez, C. Gil, and C. Baker, ‘CFD analysis of the aerodynamic effects on the stability of the flight of a quadcopter UAV in the proximity of walls and ground’, *Journal of Wind Engineering and Industrial Aerodynamics*, vol. 206, p. 104378, Nov. 2020, doi: 10.1016/j.jweia.2020.104378.

[133] F. J. Garcia Rubiales, P. Ramon Soria, B. C. Arrue, and A. Ollero, ‘Soft-Tentacle Gripper for Pipe Crawling to Inspect Industrial Facilities Using UAVs’, *Sensors*, vol. 21, no. 12, Art. no. 12, Jan. 2021, doi: 10.3390/s21124142.

[134] A. Lopez-Lora, P. J. Sanchez-Cuevas, A. Suarez, A. Garofano-Soldado, A. Ollero, and G. Heredia, ‘MHYRO: Modular HYbrid RObot for contact inspection and maintenance in oil & gas plants’, in *2020 IEEE/RSJ International Conference on Intelligent Robots and Systems (IROS)*, Oct. 2020, pp. 1268–1275. doi: 10.1109/IROS45743.2020.9341639.

[135] J. Cacace, G. A. Fontanelli, and V. Lippiello, ‘A Novel Hybrid Aerial-Ground Manipulator for Pipeline Inspection tasks’, in *2021 Aerial Robotic Systems Physically Interacting with the Environment (AIRPHARO)*, Oct. 2021, pp. 1–6. doi: 10.1109/AIRPHARO52252.2021.9571034.

[136] P. Yu, G. Chamitoff, and K. C. Wong, ‘Perching Upside Down with Bi-directional Thrust Quadrotor’, in *2020 International Conference on Unmanned Aircraft Systems (ICUAS)*, Sep. 2020, pp. 1697–1703. doi: 10.1109/ICUAS48674.2020.9213946.

[137] H. Zhang, E. Lerner, B. Cheng, and J. Zhao, ‘Compliant Bistable Grippers Enable Passive Perching for Micro Aerial Vehicles’, *IEEE/ASME Transactions on Mechatronics*, vol. 26, no. 5, pp. 2316–2326, Oct. 2021, doi: 10.1109/TMECH.2020.3037303.

[138] Norton and Silberger, ‘Parallelization and Performance Analysis of the Cooley–Tukey FFT Algorithm for Shared-Memory Architectures’, *IEEE Transactions on Computers*, vol. C–36, no. 5, pp. 581–591, May 1987, doi: 10.1109/TC.1987.1676943.

[139] S. Basu and S. Mamud, ‘Comparative Study on the Effect of Order and Cut off Frequency of Butterworth Low Pass Filter for Removal of Noise in ECG Signal’, in *2020 IEEE 1st International Conference for Convergence in Engineering (ICCE)*, Sep. 2020, pp. 156–160. doi: 10.1109/ICCE50343.2020.9290646.

[140] Y. Chen, ‘Design Methods of High-order Low Pass Filters’, in *2023 IEEE International Conference on Sensors, Electronics and Computer Engineering (ICSECE)*, Aug. 2023, pp. 572–576. doi: 10.1109/ICSECE58870.2023.10263550.

[141] W. H. Press and S. A. Teukolsky, ‘Savitzky-Golay Smoothing Filters’, *Computer in Physics*, vol. 4, no. 6, pp. 669–672, Nov. 1990, doi: 10.1063/1.4822961.

[142] L. Nguyen, N. Ulapane, J. V. Miro, G. Dissanayake, and F. Munoz, ‘Improved signal interpretation for cast iron thickness assessment based on pulsed eddy current sensing’, in *2017 12th IEEE Conference on Industrial Electronics and*

Applications (ICIEA), Siem Reap: IEEE, Jun. 2017, pp. 2005–2010. doi: 10.1109/ICIEA.2017.8283167.

[143] N. Ulapane, L. Nguyen, J. V. Miro, A. Alempijevic, and G. Dissanayake, 'Designing a pulsed eddy current sensing set-up for cast iron thickness assessment', in *2017 12th IEEE Conference on Industrial Electronics and Applications (ICIEA)*, Siem Reap: IEEE, Jun. 2017, pp. 901–906. doi: 10.1109/ICIEA.2017.8282967.

[144] 'HQ Prop 3D 5X3.5X3 Propeller (2CW, 2CCW) - Unmanned Tech Shop'. Accessed: Jul. 29, 2024. [Online]. Available: https://www.unmannedtechshop.co.uk/product/hq-prop-3d-5x35-prop/

[145] 'iFlight XING-E Pro 2207 1800KV Motor', HobbyRC. Accessed: Jul. 29, 2024. [Online]. Available: https://www.hobbyrc.co.uk/iflight-xing-e-pro-2207-1800kv-motor

[146] '3300mAh 22.2V 6S 80C Extreme Pro LiPo Battery'. Accessed: Jul. 29, 2024. [Online]. Available: https://www.overlander.co.uk/lipo-batteries/22-2v-6s/3300mah-22-2v-6s-80c-extreme-pro-lipo-battery.html

[147] 'Aikon AK32 35A BLHeli32 6S ESC - Unmanned Tech Shop'. Accessed: Jul. 29, 2024. [Online]. Available: https://www.unmannedtechshop.co.uk/product/aikon-ak32-35a-blheli32-6s-esc/

[148] 'Pololu - FEETECH Continuous Rotation Servo FS5106R'. Accessed: Jul. 31, 2024. [Online]. Available: https://www.pololu.com/product/3430

[149] F. D. Ledezma *et al.*, 'A Market Survey of Offshore Underwater Robotic Inspection Technologies for the Oil and Gas Industry', presented at the SPE

Saudi Arabia Section Annual Technical Symposium and Exhibition, Society of Petroleum Engineers, Jun. 2015. doi: 10.2118/177989-MS.

[150] S. Hamaza *et al.*, ‘Sensor Installation and Retrieval Operations Using an Unmanned Aerial Manipulator’, *IEEE Robotics and Automation Letters*, vol. 4, no. 3, pp. 2793–2800, Jul. 2019, doi: 10.1109/LRA.2019.2918448.

[151] N. Ulapane, "Nondestructive Evaluation of Ferromagnetic Critical Water Pipes Using Pulsed Eddy Current Testing," Ph.D. dissertation, Dept. of Electrical Engineering, Univ. of Technology, Sydney, Australia, pp. 62- 65, 2016.

APPENDIX A

A.1 Thickness Error View from AB Angle

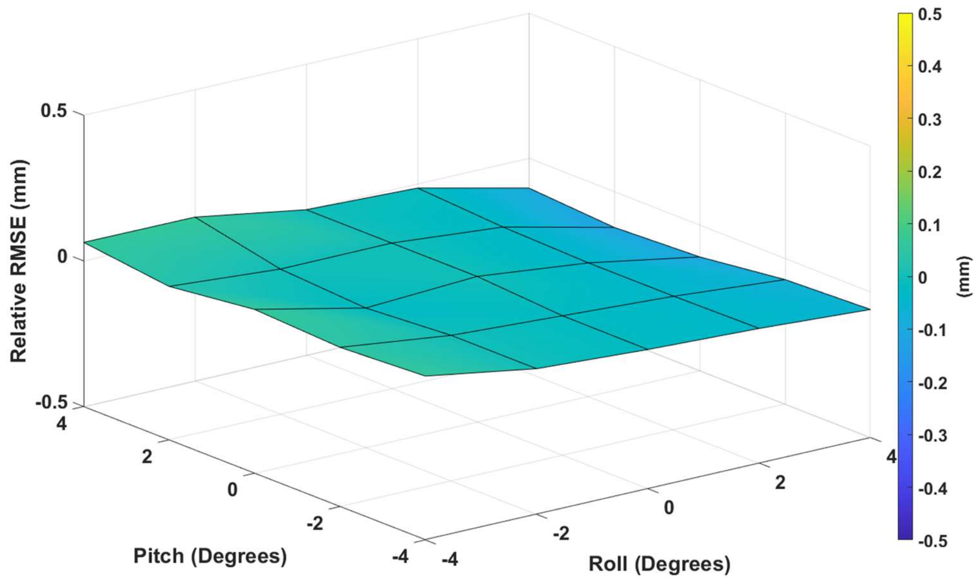

(a)

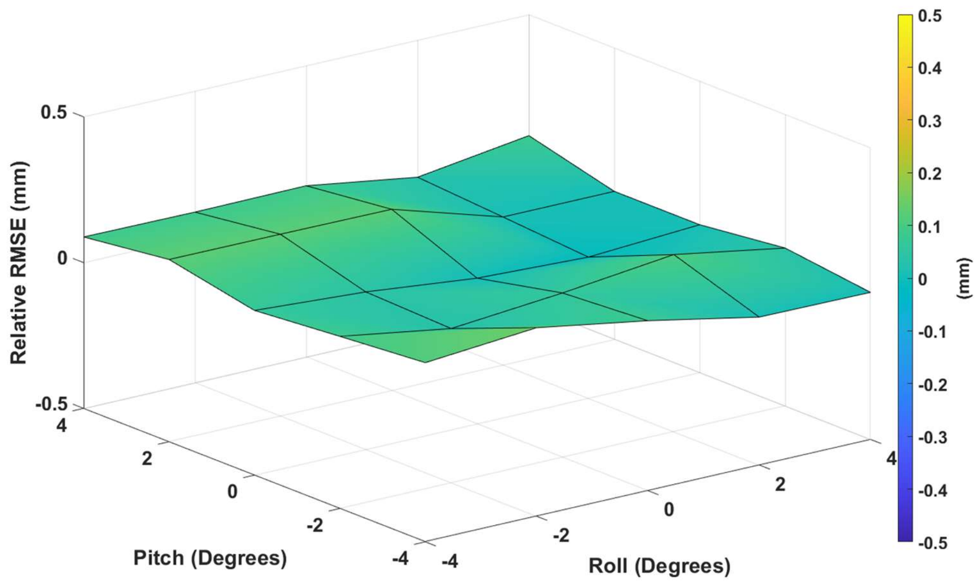

(b)

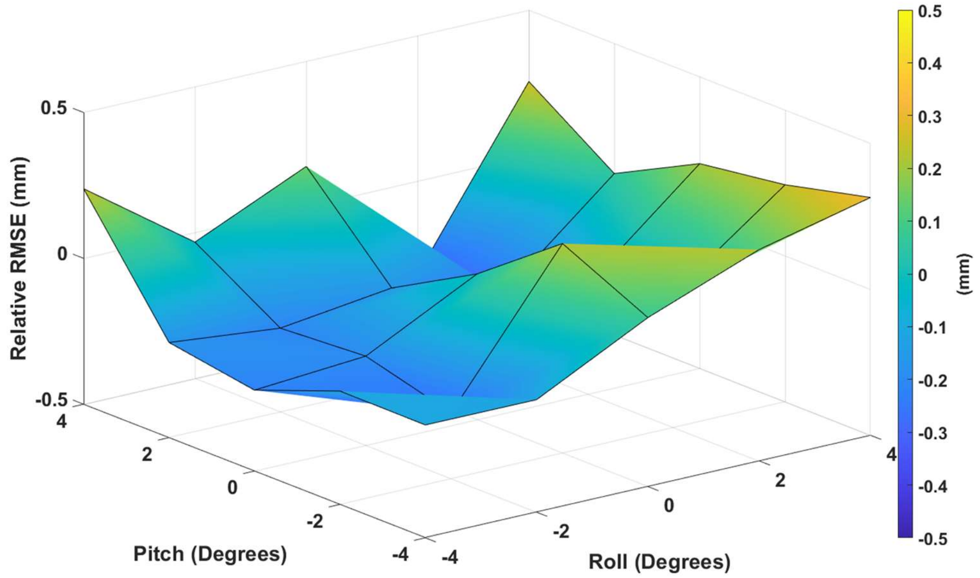

(c)

Figure A-1: AB angle thickness RMSE error, (a)-Nominal Thickness of 6 mm, (b)-Nominal thickness of 10mm, (c)-Nominal Thickness of 20 mm.

Table A-1: AB angle thickness measurement error statistical performance

Nominal Thickness (mm)	Mean RMSE (mm)	RMSE (AB) Standard Deviation (mm)
20.0	1.407	0.052
10.0	0.454	0.059
6.0	0.437	0.194

A.2 Thickness Error View from AC Angle

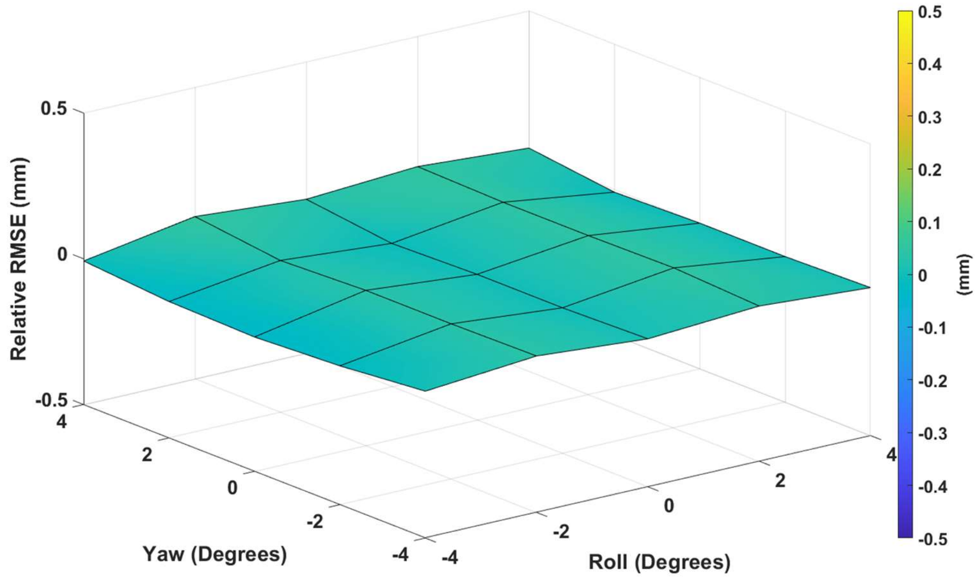

(a)

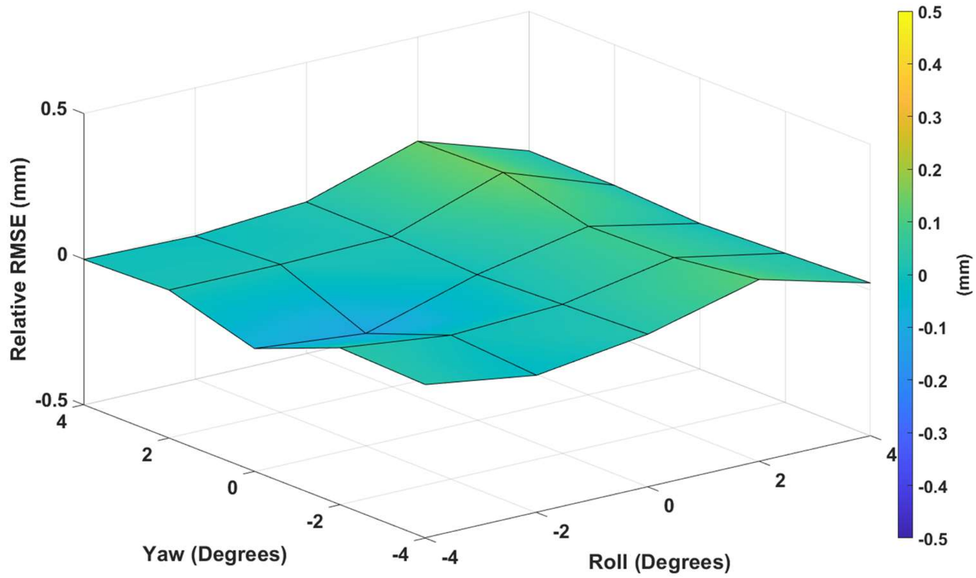

(b)

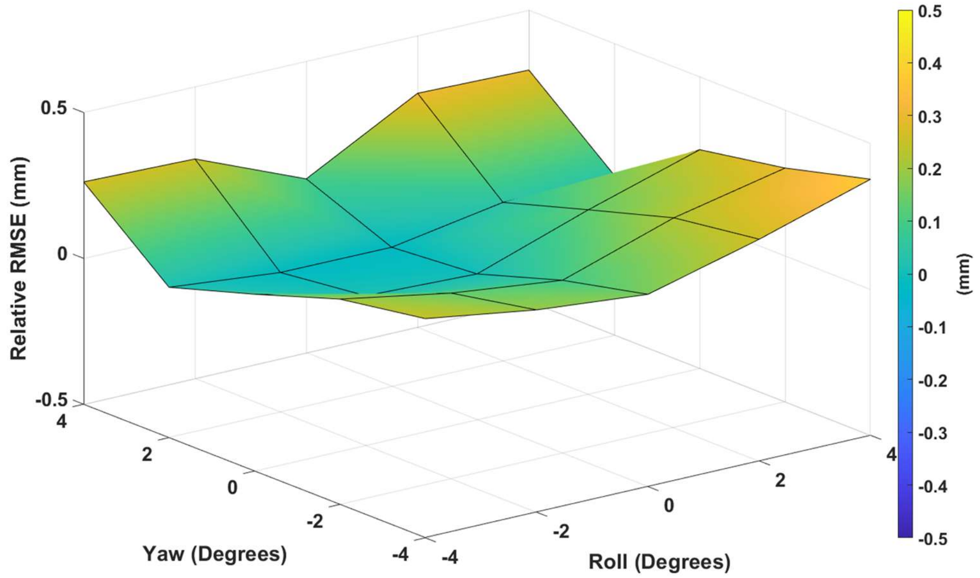

(c)

Figure A-2: AC angle thickness RMSE error, (a)-Nominal Thickness of 6 mm, (b)-Nominal thickness of 10mm, (c)-Nominal Thickness of 20 mm.

Table A-2: BC angle Thickness measurement error statistical performance

Nominal Thickness (mm)	RMSE Mean (mm)	RMSE (AC) Standard Deviation (mm)
20.0	1.408	0.026
10.0	0.453	0.058
6.0	0.451	0.115

A.3 Thickness Error View from BC Angle

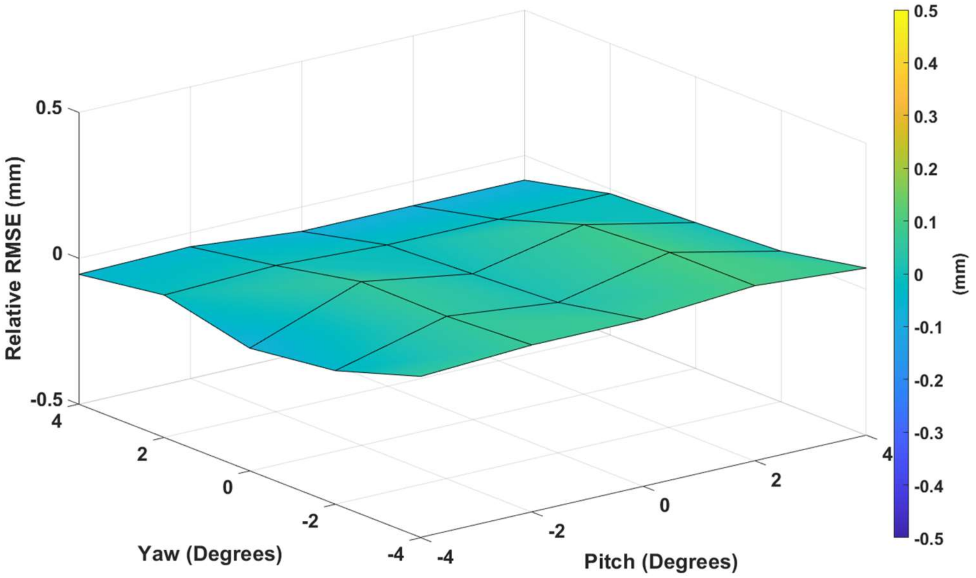

(a)

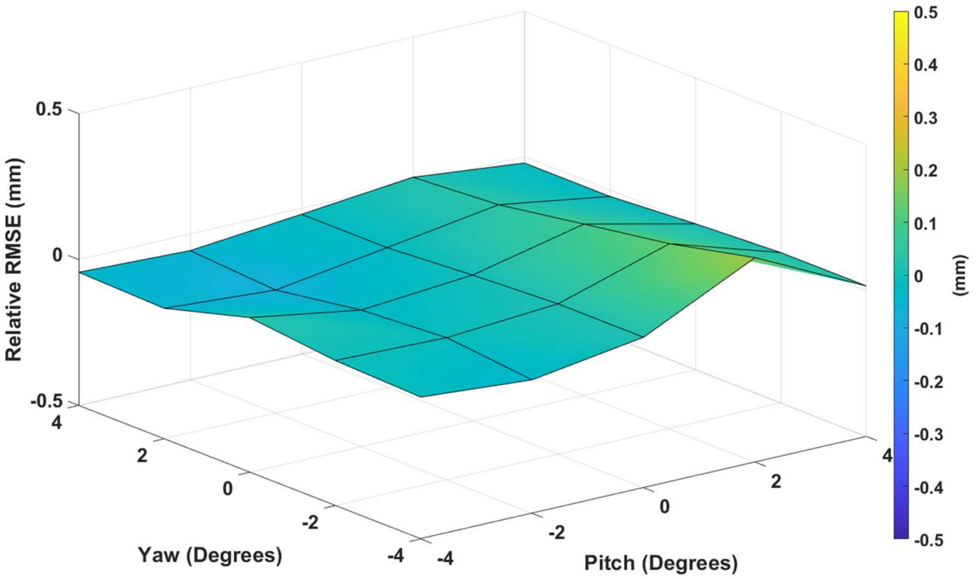

(b)

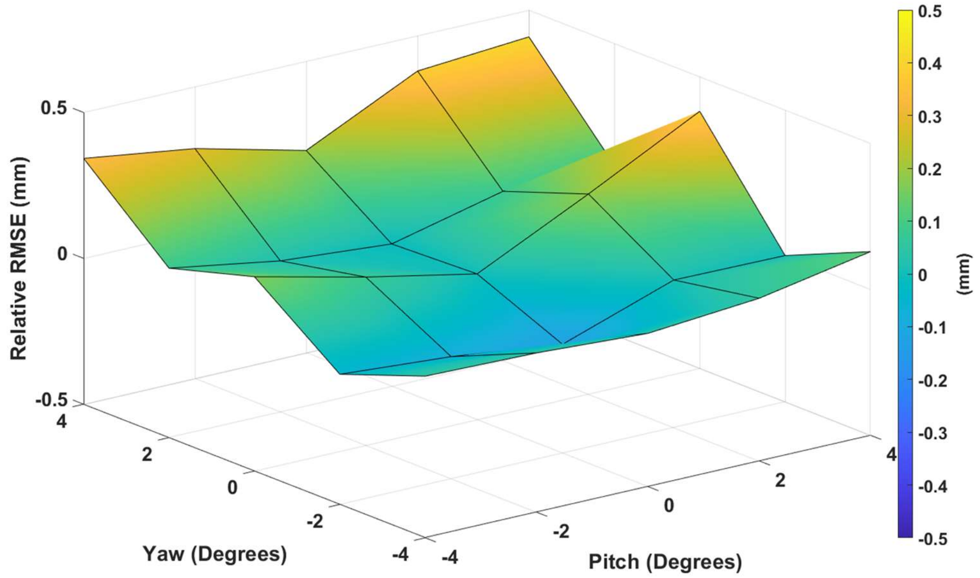

(c)

Figure A-3: AC angle thickness RMSE mean error, (a)-Nominal Thickness of 6 mm, (b)-Nominal thickness of 10mm, (c)-Nominal Thickness of 20 mm.

Table A-3: AC angle Thickness measurement error statistical performance

Nominal Thickness (mm)	RMSE Mean (mm)	RMSE (BC) Standard Deviation (mm)
20.0	1.407	0.026
10.0	0.453	0.061
6.0	0.451	0.146

A.4 Representative Raw Signals

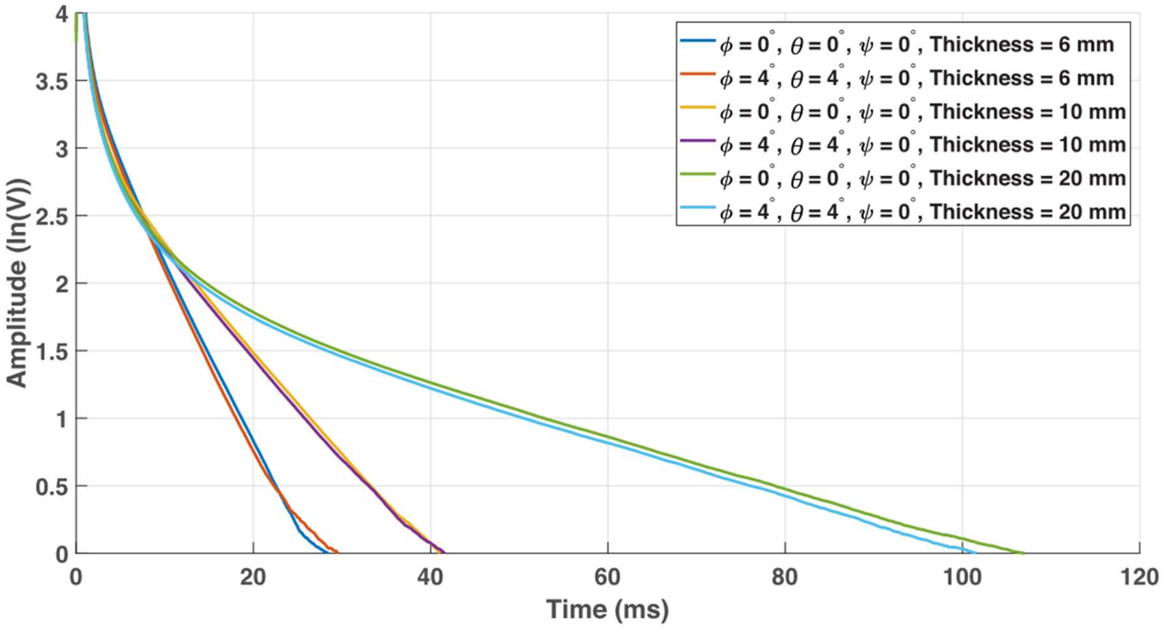

Figure A-4: Representative raw signals, captured with different setups, were exported from the MAXWELL software.